

Modeling and Classification of Voluntary and Imagery Movements through fNIR & EEG Signals for Brain-Computer Interface

By

Md. Asadur Rahman
(Roll No: 1515701)

A thesis submitted in partial fulfillment of the requirements for the degree of
Doctor of Philosophy (PhD) in the Department of Biomedical Engineering



Khulna University of Engineering & Technology (KUET)

Khulna-9203, Bangladesh

January 2020

Dedications

I would like to dedicate this Ph.D. thesis to the most honorable persons in my life-

My Boro Fuḡa

Muḡammad Khizir Khan (1948-2015),

[Ex-chairman of Baḡladesh Power Development Board (2007-2008)]

who brought liḡht to our family.

&

My Grand Sister

Mrs. Mehrunnesa (1945-2017)

who spent all of her father's properties
for the expense of my postgraduate education.

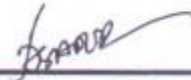
[- and I got no opportunity to share it with them]

Declaration

This is to certify that the thesis work entitled “**Modeling and Classification of Voluntary and Imagery Movements through fNIR & EEG Signals for Brain-Computer Interface**” has been carried out by **Md. Asadur Rahman** in the Department of Biomedical Engineering, Khulna University of Engineering & Technology, Khulna, Bangladesh. The above thesis work or any part of this work has not been submitted anywhere for the award of any degree or diploma.



Signature of Supervisor

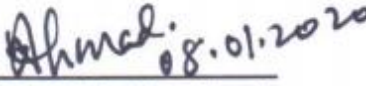
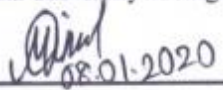
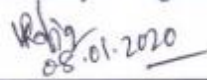
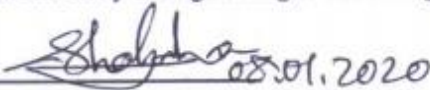
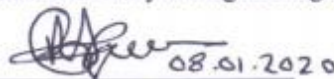

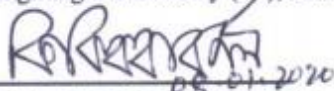


Signature of Candidate

Approval

This is to certify that the thesis work submitted by **Md. Asadur Rahman** entitled by “**Modeling and Classification of Voluntary and Imagery Movements through fNIR & EEG Signals for Brain-Computer Interface**” has been approved by the board of examiners for the partial fulfillment of the requirements for the degree of Doctor of Philosophy (Ph.D.) in the Department of Biomedical Engineering, Khulna University of Engineering & Technology (KUET), Khulna, Bangladesh in January 2020.

BOARD OF EXAMINERS

1.  08.01.2020
Prof. Dr. Mohiuddin Ahmad
Dept. of Electrical and Electronic Engineering (EEE)
Khulna University of Engineering & Technology (KUET), Khulna-9203, Bangladesh. Chairman
(Supervisor)
2.  08.01.2020
Dr. Muhammad Muinul Islam
Head of the Department
Dept. of Biomedical Engineering (BME)
Khulna University of Engineering & Technology (KUET), Khulna-9203, Bangladesh. Member
3.  08.01.2020
Prof. Dr. Md. Abdur Rafiq
Dept. of Electrical and Electronic Engineering (EEE)
Khulna University of Engineering & Technology (KUET), Khulna-9203, Bangladesh. Member
4.  08.01.2020
Prof. Dr. Md. Shahjahan
Dept. of Electrical and Electronic Engineering (EEE)
Khulna University of Engineering & Technology (KUET), Khulna-9203, Bangladesh. Member
5.  08.01.2020
Prof. Dr. A. B. M. Aowlad Hossain
Dept. of Electronics and Communication Engineering (ECE)
Khulna University of Engineering & Technology (KUET), Khulna-9203, Bangladesh. Member
6. 
Prof. Dr. Mohammad Shorif Uddin
Dept. of Computer Science and Engineering (CSE)
Jahangirnagar University (JU), Savar, Dhaka, Bangladesh. (Member)
External
7.  08.01.2020
Prof. Dr. Quazi Delwar Hossain
Dept. of Biomedical Engineering,
Chittagong University of Engineering & Technology (CUET)
Pahartoli, Raozan, Chittagong-4349, Bangladesh. (Member)
External
8. _____
Hasan Ayaz, PhD
Associate Professor (Member)
External
School of Biomedical Engineering, Science and Health Systems
Drexel University, 3141 Chestnut Street, Philadelphia, PA 19104, USA.

Acknowledgement

At the outset, I would like to prostrate to the Almighty Allah for being merciful to me and giving me the strength and resilience to complete my thesis work.

*Although the author's name is the only one to appear on the cover, it is the combined effort of these people that helped me to complete this very long academic journey from toddler to Ph.D. Therefore, I would like to take this opportunity to thank several individuals for their contributions, realizing that such a list can never be completed. At first, I would like to thank my younger aunt (**choto fufu**) and **grandma** for starting my first education. No word of thanks is sufficient to my academically uneducated parents, **Md. Anisur Rahman** and **Selina Khatun**, those who taught me all the academic and social knowledge until secondary and even guided in my Ph.D. works as well as embraced unprejudged life for me.*

*In course of starting to complete my theoretical and practical research works of PhD, I am the most grateful to my honorable supervisor, **Prof. Dr. Mohiuddin Ahmad** who was not only my mentor but also a true guardian from my personal life to academic life. A few words of thank is too insufficient to him.*

*In addition, I wish to express my sincere thanks to **Dr. Muhammad Muinul Islam**, the honorable Head of the Department of Biomedical Engineering for inspiring me. I am very grateful to **Prof. Dr. Md. Abdur Rafiq (EEE)** and **Prof. Dr. Md. Shahjahan (EEE)** to encourage me to devote myself to completing my thesis work. Especially, I want to thank **Prof. Dr. ABM Aowlad Hossain (ECE)** for giving me various valuable directions to improve my research work. I would like to thank **Prof. Dr. Mohammad Shorif Uddin**, Dept. of CSE, Jahangirnagar University, for his remarkable advice. Exclusively, I express my deepest gratitude to **Prof. Dr. Hasan Ayaz**, School of Biomedical Engineering, Science and Health Systems, Drexel University, USA for his wonderful guidelines to solve many critical problems regarding this thesis work. I am also thankful to my one of the most loving personality and teacher **Prof. Dr. Md. Shalah Uddin Yusuf** and **Prof. Dr. Mostafa Zaman Chowdhury**, Department of EEE, KUET, Khulna.*

*It is my pleasure to acknowledge the roles of several special individuals in my life. Distinctive thanks to **Md. Mahub Hossain Biplob**, who taught me fundamentals of computer-based applications and to **Eng. Md. Motiul Islam**, who taught the ground rules of programming language. It is my honor to thank you, **Md. Shirajul Islam Hero** because you always looked after me not to be misguided. I am also indebted to my three uncles **Md. Ataur Rahman**, **Md. Azizur Rahman**, and **Md. Amanur Rahman**, for supporting me in this journey. I am grateful to my honorable Father-in-law and Mother-in-law to believe in me. I would like to take the opportunity to thank my beloved aunts (**Mamota**, **Shahanaaj**, **Shilpi**, **Jolpy**, and **Makhan**) and boro mama, boro mami, choto mama and choto mami for their reasonless love.*

*I am grateful to all BME faculty members, participants participated in data recordings, the very loving staff of BME Department, and who helped and supported me directly, indirectly, and mentally. Thank you, my dear fellows: **Anika**, **Milu**, **Galib**, **Gourav**, **Noman**, **Faisal**, **Babu**, and **Tarun Da** (My mighty brother) for all of your kind supports and continuous help.*

*I want to acknowledge some beautiful people for their indescribable role in my journey of education: **Md. Alamgir Hossain (Jahid vai), Rasel Ahmmed, Md. Jobayer Hossain, Md. Towsif Rabbany (Avi vai), Md. Istiaque Reza, Anupam Das, Munmun Talukder Sumon, Md. Zaharul Islam, Md. Robiul Islam, Md. Asaduzzaman, Anirban Sen Swaksher, Md. Mamunur Rahman (Rana vai), Md. Jobayer Hossain,** and many more loving persons.*

*I am very honored and pleased having you **Eng. Farzana Khanam**, as a partner in my study and life; your all forms of supports, dedication, and patience during my thesis work were really blessing for me. At last, I would like to mention the name **Amyra Mehjabin Aqsa** (my loving daughter) who brings the only happiness during this multifaceted journey.*

This research work was supported by Higher Education Quality Enhancement Project (HEQEP), UGC, Bangladesh under Subproject “Postgraduate Research in BME,” CP#3472, KUET.

Author
January 2020

Declaration of Publications

I hereby declare that this dissertation incorporates the outcome of research undertaken by me under the supervision of **Professor Dr. Mohiuddin Ahmad**. The contribution is covered in Chapters 3, 4, and 5 of this thesis. In all cases, the key ideas, primary contributions, experimental designs, data analysis, and interpretation, were performed by the author, and the contribution of co-author was primarily through the provision of valuable suggestions and helping in comprehensive analysis of the simulation results for the publications. This thesis includes following papers that have been previously published/accepted for publication/submitted for publication in peer-reviewed journals and conferences, as follows:

Thesis Chapter	Publication Title/Full Citation	Publication Status
Chapter 3	Md. Asadur Rahman , Mohiuddin Ahmad, and Mohd Abdur Rashid, “Selecting the optimal conditions of Savitzky-Golay filter for fNIRS signal,” <i>Biocybernetics and Biomedical Engineering</i> , vol. 39, no. 3, pp. 624-637, 2019. doi.org/10.1016/j.bbe.2019.06.004	Published
	Md. Asadur Rahman , Farzana Khanam, Md. Kazem Hossain, Mohammad Khurshed Alam and Mohiuddin Ahmad, “Four-Class motor imagery EEG signal classification using PCA, wavelet and two-Stage neural network” <i>International Journal of Advanced Computer Science and Applications (IJACSA)</i> , vol. 10, no. 5, 2019. doi.org/10.14569/IJACSA.2019.0100562	Published
	Md. Asadur Rahman and Mohiuddin Ahmad, “A straight forward signal processing scheme to improve effect size of fNIR signals,” 5 th <i>International Conference on Informatics, Electronics & Vision (ICIEV)</i> , Dhaka University, Dhaka, Bangladesh, May 2016. doi.org/10.1109/ICIEV.2016.7760042	Published
	Md. Asadur Rahman and Mohiuddin Ahmad, “Identifying appropriate feature to distinguish between resting and active condition from FNIRS,” 3 rd <i>International Conference on Signal Processing and Integrated Networks, SPIN 2016</i> , Amity University, Noida, New Delhi, India, February 2016. doi.org/10.1109/SPIN.2016.7566781	Published
	Md. Asadur Rahman and Mohiuddin Ahmad, “Lie detection from fNIR signal and neuroimage,” <i>Int. Conf. on Medical Engineering, Health Informatics and Technology (MediTec)</i> , 17-18 December 2016, Dhaka, Bangladesh. doi.org/10.1109/MEDITEC.2016.7835382	Published

	Md. Asadur Rahman , and Mohiuddin Ahmad, “Lie detection from single feature of functional near infrared spectroscopic (fNIRS) signals,” <i>2nd International Conference on Electrical & Electronic Engineering (ICEEE 2017)</i> , 27-29 December, Rajshahi University of Engineering & Technology (RUET), Bangladesh. doi.org/10.1109/CEEE.2017.8412900	Published
Chapter 4	Md. Asadur Rahman and Mohiuddin Ahmad, “Modeling and classification of voluntary and imagery movements from the prefrontal fNIRS signals” (in <i>URASHIP Journal of Advanced Signal Processing</i>).	Under Review
	Md. Asadur Rahman and Mohiuddin Ahmad, “Evaluating the connectivity of motor area with prefrontal cortex by fNIR spectroscopy,” <i>International Conference on Electrical, Computer, and Communication Engineering</i> , 2017, Cox’s Bazar, Bangladesh, February 16-18. doi.org/10.1109/ECACE.2017.7912921	Published
	Md. Asadur Rahman and Mohiuddin Ahmad, “Movement related events classification from functional near infrared spectroscopic signal,” <i>Int. Conf. on Computer and Information Technology (ICCIT)</i> , Dhaka, Bangladesh, 18-20 December 2016, Dhaka, Bangladesh. doi.org/10.1109/ICCITECHN.2016.7860196	Published
	Md. Asadur Rahman , Md. Mahmudul Haque Milu, Anika Anjum, Farzana Khanam, Md. Nurunnabi Mollah, and Mohiuddin Ahmad, “Classification of Motor Imagery Events from Prefrontal Hemodynamics for BCI Application,” <i>International Joint Conference on Computational Intelligence (IJCCI)</i> , 14-15 December 2018, Daffodil International University, Dhaka, Bangladesh. pp. 1-06. doi.org/10.1007/978-981-13-7564-4_2	Published
	Md. Asadur Rahman , Mohiuddin Ahmad, and Farzana Khanam, “Detection of effective temporal window for classification of motor imagery events from prefrontal hemodynamics,” <i>International Conference on Electrical, Computer and Communication Engineering (ECCE 2019)</i> , CUET, Bangladesh. doi.org/10.1109/ECACE.2019.8679317	Published
Chapter 5	Md. Asadur Rahman , Mohammad Shorif Uddin, and Mohiuddin Ahmad, “Modeling and Classification of Voluntary and Imagery Movement through fNIR & EEG Signals for Brain-Computer Interface,” <i>Health Information Science and Systems</i> , vol. 7, no. 22, December 2019. doi.org/10.1007/s13755-019-0081-5	Published

Abstract

Neural activation measurement regarding voluntary and imagery movement is a crucial argument for brain-computer interface. Generally, movement-related hemodynamics is measured from the central lobe of the brain which may be erroneous for the paralyzed people due to their inactiveness of this brain area. To overcome this limitation, this thesis work proposes an approach to measure the movement-related hemodynamics from the prefrontal cortex. In the proposed research work, the changes of the oxidized hemoglobin (HbO_2) and deoxidized hemoglobin (dHb) concentration regarding different voluntary and imagery movement stimuli are captured by functional near-infrared spectroscopy (fNIR) from several subjects. With necessary preprocessing, the fNIR signals are statistically analyzed by ANOVA and effect size method to localize the most significantly activated regions of the prefrontal cortex regarding the voluntary and imagery stimuli. The experimental results show that voluntary and imagery movements have a strong correlation with the prefrontal cortex. The temporal pattern of HbO_2 and dHb signals regarding the most activated regions are modeled by polynomial regression. Consequently, the model activation patterns are used to classify the voluntary and imagery tasks based on the maximum similarity approach. In addition, conventional classification methods are used to classify the signals. In this work, we consider two, four, and six class fNIR data of movement-related tasks for classification. The classification accuracies of the proposed method are convincing and found almost similar to the conventional procedure. The outcomes of this proposed work suggest that the prefrontal hemodynamics can be used for the modeling and classification of the voluntary and imagery movement-related tasks which will be helpful for the brain-computer interface applications. The combination of fNIR and electroencephalography (EEG) signals has become the best choice of accurate brain-computer interface (BCI) because of their finer spatiotemporal resolution. The purpose of this work is to develop an effective BCI model to classify the brain signals (fNIR and EEG) regarding the voluntary and imagery movements. For achieving the high classification accuracy from the developed BCI system, convolutional neural network (CNN) has been used to extract the features automatically from the multiple channel fNIR and EEG signals instead of the

manual feature selection. In this work, eight different movement-related stimuli (four voluntary and four imagery movements of hands and feet) have been considered. The multiple channel fNIR and EEG signals are used to prepare functional neuroimages to train and test the performance of the proposed BCI system. In addition, the proposed procedure is applied to prepare neuroimages from the individual modality (fNIR and EEG) to train and test the performance of the CNN based BCI system. The results reveal that the combined-modality approach of fNIR and EEG provides improved classification accuracy than the individual one. From the results, we found that the proposed CNN-based BCI system of bimodal (fNIR+EEG) approach outperforms the unimodal (only fNIR) methods in terms of the classification accuracy. Therefore, the outcomes of the proposed research work will be very helpful to implement the finer BCI system, in future.

Table of Contents

<i>Title Page</i>	<i>i</i>
<i>Dedications</i>	<i>ii</i>
<i>Declaration</i>	<i>iii</i>
<i>Approval</i>	<i>iv</i>
<i>Acknowledgement</i>	<i>v-vi</i>
<i>Declaration of Publication</i>	<i>vii-viii</i>
<i>Abstract</i>	<i>ix-x</i>
<i>Contents</i>	<i>xi-xiii</i>
<i>List of Figures</i>	<i>xiv-xvii</i>
<i>List of Tables</i>	<i>xviii</i>
<i>List of Abbreviations</i>	<i>xix-xx</i>

CHAPTER#	TITLE OF THE CHAPTER		PAGE NO
CHAPTER 1	Introduction		1-6
	1.1	Motivation	1-2
	1.2	Problem Statements	2-3
	1.3	Objectives	4
	1.4	Contributions of the Proposed Research	4-5
	1.5	Organization of the Dissertation	5-6
CHAPTER 2	Optical and Electrical Techniques of Functional Neuroimaging		7-24
	2.1	Introduction	7-8
	2.2	Fundamentals of fNIR	8-17
		2.2.1 Oximetry & Hemodynamic Response	9
		2.2.2 Optical Measurement	10-12
		2.2.3 The Characteristics of fNIR Signal	12-14
		2.2.4 Hemodynamics of Voluntary and Imagery Movements	14-17
	2.3	Fundamentals of Electroencephalography (EEG)	17-24
		2.3.1 How EEG is Generated?	17-19
		2.3.2 EEG Acquisition Method	19-20
		2.3.3 Rhythmic Properties of EEG Signal	20-22

	2.3.4	Noise Sensitivities of EEG Signal	22-23
	2.3.5	Spatiotemporal Resolution of EEG	23
	2.3.6	EEG Signal behavior for Imagery Movements	23-24
	2.4	Conclusion	24
CHAPTER 3	Signal Processing Techniques		25-54
	3.1	Introduction	25
	3.2	fNIR Signal Preprocessing	25-32
	3.2.1	Motion Artifact Rejection by SMAR Algorithm	26
	3.2.2	Compression	26-27
	3.2.3	Filtering	28-32
	3.2.4	Baseline Correction	32
	3.3	EEG Signal Preprocessing	32-38
	3.3.1	Notch Filter	33
	3.3.2	Elliptic Filter	33-34
	3.3.3	Eye Blink Removal	35
	3.3.4	Wavelet Packet Transformation based Feature Extraction	35-36
	3.3.5	Power Spectral Density Calculation	37-38
	3.4	Combining fNIR and EEG Signals to Produce Neuroimages	38-41
	3.5	Classification	41-54
	3.5.1	Proposed Classification Method	41-42
	3.5.2	Conventional Classification Methods	43-47
	3.5.3	Convolutional Neural Network	47-54
	3.6	Conclusion	54
CHAPTER 4	Statistical Modeling of Voluntary and Imagery Movement		55-74
	4.1	Introduction	55-56
	4.2	Materials and Methods	56-61
	4.2.1	Data Acquisition Protocol	56-57
	4.2.2	Data Acquisition	57-58
	4.2.3	Preprocessing	58-59
	4.2.4	Statistical Analysis and Activation Modeling	59-61

	4.3	Results and Discussions	61-73	
	4.5	Conclusions	73-74	
CHAPTER 5	Predictive Modeling by CNN through fNIR and EEG Signals		75-95	
	5.1	Introduction	75-77	
	5.2	Materials and Methods	77-	
		5.2.1	Data Acquisition Protocol	77-78
		5.2.2	Data Acquisition	78-80
		5.2.3	Methods	80-82
	5.3	Results and Discussions	82-94	
	5.4	Conclusions	95	
CHAPTER 6	Conclusions and Future Perspectives		96-97	
	6.1	Conclusions	96-97	
	6.2	Future Perspectives	97	
References			98-114	
List of Publications			115-117	
Appendix			118-127	

List of Figures

Figure No	Description	Page No
2.1	Absorption coefficients of H ₂ O, HbO ₂ , and dHb.	8
2.2	Relation between hemodynamic response and oxygen concentration.	9
2.3	Position of NIR source and detector on human scalp.	10
2.4	Optode and channel configuration of fNIR devices (Model 1200) head band.	11
2.5	Example of raw fNIR signal (both dHb & HbO ₂) of a particular channel. It is easily discernable that these two signals are negatively correlated.	13
2.6	The PSD of an fNIR (HbO ₂) signal. The magnitudes are not normalized in this figure. The numerical values of frequency spectra are connected by b-spline interpolation.	13
2.7	The movement related brain activations and the significance of the brain lobes in cyclic operations of a complete movement cycle.	15
2.8	These results are based on the 5 sec tasks + 20 sec hemodynamic observation. Here, the mean activation changes in HbO ₂ (solid lines) and dHb (dotted lines) regarding the response of a left and right hand movements in both voluntary and imagery manner. The most significant channel information about mean activation changes in HbO ₂ and dHb has been represented for both hemispheres: right hemisphere (left panel) and left hemisphere (right panel).	16
2.9	The change in concentration of HbO ₂ (solid lines) and dHb (dotted lines) for right hand (left panel) and left hand (right panel) movement execution (upper panel) and imagery (lower panel) of three positions of interest: prefrontal cortex (PFC); primary motor areas (MI); somatosensory motor areas (SMC) regarding the left and right hand movement for both voluntary and imagery tasks.	17
2.10	The procedure of the extracellular voltage field generation from graded synaptic activity. Here, the relationship between the polarity of site of dendritic PSP and surface potentials has been illustrated.	19
2.11	A single plane projection of the head, showing all standard positions and the location. This figure is redrawn according to the recommendation of the international federation.	20
2.12	A typical full band EEG signal and its different rhythmic band signals.	21
2.13	Human brain and its major lobe allocation.	24
3.1	Preprocessing steps of raw fNIR signals and their chronological order.	25

3.2	This figure presents the actual signal dimensions in Eigen-space which is formed by the three principal components of PCA analysis. The figure shows four linearly uncorrelated solution vectors with the channel number.	27
3.3	The characteristics of Hamming window in the time domain (a) and frequency domain (b) for 20 order low pass linear phase FIR filter.	29
3.4	Filtering performance comparison between SG and FIR filter for fNIR signal for both HbO ₂ and dHb signals [11].	32
3.5	Magnitude response of the 50 Hz notch filter with 256 Hz sampling rate. The frequency has been normalized here and the magnitude has been presented in dB.	33
3.6	Frequency response of an elliptical filter of 5 th order with arbitrary pass band and stop band ripple.	34
3.7	Graphical representation of wavelet packets decomposition method that decomposes $I_{0,0}$ into tree-structured subspaces.	36
3.8	Combining the fNIR and EEG data to prepare the spatiotemporal neuroimages for classification by CNN.	39
3.9	Prepared spatiotemporal neuroimage combining the fNIR and EEG data by the proposed method.	40
3.10	Classification mechanism of the proposed method utilizing the proposed activation models.	42
3.11	The overall mechanism of the conventional machine learning based classifiers.	43-44
3.12	The block diagram illustrates the basic concept of deep learning approach with its relationship in the field of machine learning.	48
3.13	Feature extraction as a separate function to be used for the classifier. The feature extraction step was independent to the machine learning.	48
3.14	Basic architecture of a typical CNN.	49
3.15	The basic process of a convolutional layer in CNN.	51
3.16	A simple example of the process of mean and max pooling operation.	53
4.1	An illustration to describe the framework of this research work. This work localizes the significant activated areas regarding voluntary & imagery movements and models those hemodynamic activation patterns. The fNIR signals corresponding to the different movement related tasks have been classified by several machine learning algorithms considering the polynomial regression coefficients as features.	56
4.2	Time schedule of data acquisition protocol for each participant regarding both the voluntary and imagery movements. This is a unit task performing schedule that was repeated four times in each session	57

	to complete 20 individual trials of every task.	
4.3	Schematic illustration of MATLAB based protocol instruction aiding application for the experiment. Regarding the instruction of this application, the participant is asked to move left hand (voluntary or imagery) by Figure 4.3(a) and after that, Figure 4.3(b) instructs to take rest.	57
4.4	The optode and channel configurations of fNIR devices (Model 1200) sensor pad.	58
4.5	Data acquisition procedure from participant connecting by used hardware.	58
4.6	The change in hemodynamic concentration (HbO ₂ and dHb) regarding the movement execution stimuli: LH (a), RH (b), LF (c), and RF (d) correspond to the ROI's: LL, LM, RM, and RL. It is the hemodynamic activations of a single participant. The activations are regarding 20 trials of four movement execution tasks.	62
4.7	The change in the concentration of HbO ₂ and dHb regarding the imagery movement stimuli: iLH (a), iRH (b), iLF (c), and iRF (d) correspond to the ROI's: LL, LM, RM, and RL. It is the hemodynamic activations of the same participant as the data of Figure 7. Here, there are 20 trials of four imagery movement tasks.	63
4.8	The grand average hemodynamic activation pattern (HbO ₂ & dHb) from all the trials of all the participants regarding only the most activated regions of prefrontal cortex. Here the activation pattern of LF and RF movements are excluded due to their insignificant ($p > 0.05$) activation level.	67
4.9	The average activation pattern of HbO ₂ and dHb of different voluntary and imagery movements and their model activation pattern by 5th order polynomial regression.	69
4.10	Subject dependent classification accuracies utilizing the spatiotemporal activation model with the proposed classification method regarding the 2, 4, and 6-class viewpoints.	71
4.11	Subject dependent classification accuracies for 2-class data (iLH & iRH).	71
4.12	Subject dependent classification accuracies for 4-class data (iLH, iRH, iLF, & iRF).	72
4.13	Subject dependent classification accuracies for 6-class data (LH, RH, iLH, iRH, iLF, & iRF).	72
4.14	Average classification accuracies of the different classifiers for 2, 4, and 6-class fNIR data by the applied classifiers.	72
5.1	Time schedule of data acquisition protocol for each participant regarding both the voluntary and imagery movements. This is a unit task performing schedule that was repeated four times in each session	77

	to complete 40 individual trials of every task.	
5.2	The electrodes and the data acquisition module of B-Alert X-10 wireless EEG system.	79
5.3	The combined fNIR-EEG sensor positions on the scalp and prefrontal cortex. The data of parietal lobe are acquired through the main data acquisition period but excluded for proposed offline processing.	80
5.4	Data acquisition of voluntary and imagery movements by concurrent fNIR and EEG modalities.	80
5.5	The training and testing phase of CNN based predictive model to classify the voluntary and imagery tasks for BCI.	81
5.6	Step by step EEG signal pre-processing: (a) Raw EEG signal of a single channel, (b) EEG signal after removing 50 Hz power line noise, (c) Filtered EEG signal upto 45 Hz by third order elliptical filter, and (d) Eye-blink and EOG artifact free EEG signal which is filtered by the EWCA toolbox.	83
5.7	The power of alpha and beta band of left and right hand imagery movement.	83
5.8	The general structure of a CNN based classifier.	87
5.9	The features of the input images with the changes of layers of the CNN based classifiers.	87
5.10	The training and validation accuracy with loss performances with respect to the epoch iterations for 4-class problem.	89
5.11	The training and validation accuracy with loss performances with respect to the epoch iterations for 6-class problem.	89
5.12	The training and validation accuracy with loss performances with respect to the epoch iterations for 8-class problem.	90
5.13	Overall performances (mean± standard deviation) of the classification accuracy through SVM, LDA, and the proposed CNN method while only the fNIR data were considered.	93
5.14	Overall performances (mean± standard deviation) of the classification accuracy through SVM, LDA, and the proposed CNN method while combined fNIR and EEG data were considered.	93

List of Tables

Table No	Description	Page No
3.1	Recommended optimal conditions of SG filter for removing physiological noises from fNIR signal with compared to the conditions of FIR filter.	31
4.1	The statistical results of the activations regarding all voluntary and imagery stimuli. Here, both results of ANOVA and ES are tabularized.	65
4.2	The functional neuroimages of prefrontal cortex regarding different voluntary and imagery movements. These images are prepared from the grand average of all population's trials.	68
5.1	The average neural activations regarding different stimuli. The activation was calculated based on the relative power spectral density of the channels.	84
5.2	Neuroimages from the temporal HbO ₂ and dHb fNIR data of 10 sec task plus 20 sec activation. Here, there are the images of eight types of tasks with 6 trials of each task.	85
5.3	Neuroimages from the combined fNIR and EEG data of 10 sec task plus 20 sec activation.	86
5.4	The details about the layers of the proposed CNN structure applied in this research.	88
5.5	Parameters considerations in the proposed CNN based model training.	88
5.6	The classification accuracy of the SVM, LDA, and the proposed model with the fNIR data only.	92
5.7	The classification accuracy of the SVM, LDA, and the proposed model with the combined fNIR and EEG data.	92
5.8	Comparison of the proposals of the multiple class BCI system.	94

List of Abbreviations

Abbreviated Form	Elaboration
ANN	Artificial Neural Network
ANOVA	Analysis of Variance
AP	Absolute Power
BCI	Brain-Computer Interface
BV	Blood Volume
BVRF	Biological Visual Receptive Field
CNN	Convolutional Neural Network
COBI	Cognitive Optical Brain Imaging
CSP	Common Spatial Filter
CT	Computed Tomography
dHb	Deoxygenated Hemoglobin
DNN	Deep Neural Network
DPF	Differential Path-Length Factor
EAWICA	Enhanced Automatic Wavelet Independent Component Analysis
EEG	Electroencephalography
EOG	Electrooculography
EPSPs	Excitatory Postsynaptic Potentials
ES	Effect Size
FIR	Finite Impulse Response
fMRI	Functional Magnetic Resonance Imaging
fNIR	Functional Near Infrared Spectroscopy
HbO ₂	Oxygenated Hemoglobin
ICA	Independent Component Analysis
IIR	Infinite Impulse Response
IPSPs	Inhibitory Postsynaptic Potentials
iLF	Imagery Left Foot
iLH	Imagery Left Hand
iRF	Imagery Right Foot
iRH	Imagery Right Hand
kNN	k-Nearest Neighbor
KUET	Khulna University of Engineering & Technology
LDA	Linear Discriminant Analysis
LF	Left Foot
LH	Left Hand
LL	Left Lateral
LM	Left Medial
MBLL	Modified Beer-Lambert Law
MEG	Magneto-encephalography
MRI	Magnetic Resonance Imaging
NIR	Near-Infrared
OXY	Oxygenated Blood Volume

PCA	Principal Component Analysis
PFC	Prefrontal Cortex
PSD	Power Spectral Density
PSP	Postsynaptic Potentials
ReLU	Rectangular Linear Unit
RF	Right Foot
RH	Right Hand
RL	Right Lateral
RM	Right Medical
ROI	Region of Interest
RP	Relative Power
SG	Savitzky-Golay
SMAR	Sliding-window Motion Artifact Rejection Algorithm
SMC	Somatosensory Motor Areas
SNN	Shallow Neural Network
SNR	Signal to Noise Ratio
SVM	Support Vector Machine
VLFO	Very Low Frequency Oscillations
WPT	Wavelet Packet Transformation
WT	Wavelet Transformation

CHAPTER 1

Introduction

1.1 Motivation

The brain controls all human activities like movements, mental workload, emotion, vision, thinking, attention, cognitive skills, senses, etc. The brain functions are related to the variation of oxygen saturation of the blood which is called hemodynamics. During the brain functioning, neurons (the unit of brain tissue) communicate with each other by the low potential electric signal. Therefore, changes in the concentration of oxygenated hemoglobin (HbO_2) and deoxygenated hemoglobin (dHb) hemoglobin, as well as electrical potential measurement, provide information about brain functioning, non-invasively. Electroencephalogram (EEG) and functional near infrared spectroscopy (fNIR) are two non-invasive methods to measure electric potential and hemoglobin concentrations in our brain, respectively.

Functional brain imaging has added a new dimension in biomedical engineering and explored the pathway to reach the ideal brain-computer interface (BCI). BCI contributes to various fields of research in biomedical applications like prevention, detection, diagnosis, rehabilitation, and restoration [1-3]. In the field of BCI, EEG and MEG are two non-invasive modalities based on scalp electric potential. EEG has a very high temporal resolution ($\sim 1\text{ms}$) with a poor spatial resolution (EEG: 5 to 9 cm) [4] (Burle, et al. 2015). Though MEG has both high temporal ($\sim 1\text{ms}$) and spatial resolution ($< 1\text{cm}$), it is not suitable for BCI because of its noise sensitivity and heavyweight [5-6]. Based on hemodynamics, functional magnetic resonance imaging (fMRI) provides excellent spatial resolution (3~6mm) but its temporal resolution is poor (1~3sec) [6]. Nonetheless, due to its very high cost, motion sensitivity, and being bulky it is also not suitable for BCI [7-9]. To optimize the aforementioned limitations and requirements, it is a high demand for a new modality. fNIR is such a neuroimaging modality discovered in 1977 by Jöbsis [10]. The researches in [11-13] reported that wavelength of NIR range (650-1000 nm) enables real-time non-invasive detection of hemoglobin oxygenation using fNIR technique. fNIR provides very good spatial resolution ($\sim 1\text{-}1.5\text{cm}$), moderate temporal resolution (up to 100Hz),

portability to use, low cost, high value of signal to noise ratio (SNR), less motion artifact compared to fMRI, MEG, EEG, and PET [9]. Furthermore, fNIR is not as physically confining as fMRI and it allows movement during imaging. Recent publications [14-16] demonstrated that the results of fNIR are comparable to fMRI and reliable for cortical activations measurement. Since fNIR provides finer spatial resolution and EEG provides finer temporal resolution, combined information of fNIR and EEG is getting the most attention for the recent researches [14, 17-25] in the field of neuroimaging and BCI.

According to the statistics of World Bank, around one billion people in the world experience some forms of disability [26]. Since, the brain of the most of these disable persons work partially or completely, BCI could be a possible solution to provide them easier life by declining their physical limitations.

1.2 Problem Statements

There's a large body of existing BCI designs that utilizes a single neuroimaging modality such as either EEG or fNIR. From the current literature review [27] found that the mostly proposed BCI system is based on motor imagery tasks with compared to the other like mental counting, mental arithmetic, word formation, etc. The limitations of the single modality based BCI related to motor imagery as well as motor execution or voluntary movement is lower accuracy for multiple tasks classifications. Therefore high performance BCI system implementation, multimodal imaging methods are proposed. Several research works [19, 22-24, 28] based on movement related tasks classification have been accomplished combination of fNIR & EEG signals for BCI. With the help of neural signals of motor actions, authors in [22-24] showed that the classification efficiency of combining fNIR & EEG is better than that of the individual modalities but in these studies, two class problems were discussed. For multiple motor tasks, asynchronous BCI technique by hybrid fNIR-EEG has been discussed in [19].

Since EEG has very lower spatial resolution, for multiple stimuli the classification accuracy remains lower. As a result to differentiate the multiple tasks like hands and feet imagery and voluntary movement related neural activations, fNIR is a good choice because of it high spatial resolution. The research works [28-31] have been

broadly studied on about motor imagery and voluntary tasks (movements of hands and feet) by fNIR. These research works have drawn their conclusion based on the data acquired from the central part of their brain except the most recent research work [28]. Nonetheless, the movement disordered or paralysed persons have inactiveness of their central part of the brain. On the other hand, it is reported in [28, 32-35] that the motor action planning (related to motor imagery tasks) is occurred in frontal lobe. This motor action sensitivity in prefrontal cortex was checked by our research work described in [36-38] where we found that there is a strong correlation with the prefrontal lobe during upper limb movements or movement imagination (or planning). Therefore, avoiding prefrontal cortex information proper BCI would be inappropriate where multiple motor-tasks are deliberated as stimuli.

In addition, no previous works performed the localized hemodynamic action modelling which is also important for BCI. Since both voluntary and imagery movement create same localized activation, it is also obligatory to differentiate the activations of voluntary and imagery movements. Therefore based on the all existing research works, following limitations are originated:

- Existing research works did not model the localized hemodynamic models of human movements.
- The impacts of motor planning activations are not considered in previous research works for BCI purpose.
- Most of the existing BCI's are designed based on single modality which limits the issue of spatiotemporal resolution.
- No significant research works are accomplished for movement related BCI by multimodal neuroimaging method.

Therefore, some scopes arise to overcome the previous limitations. This proposal scopes to design multimodal BCI and activation modelling of multiple motor actions of voluntary and imagery movements by combining fNIR and EEG.

1.3 Objectives

The objective of this work is to find the neuronal activation pattern of the human brain during the voluntary and imagery movement execution. Since this activation can be measured by the optical method (fNIR) and electrical method (EEG), using both of these modalities proper information about human movements (imagery and voluntary) will be extracted and modeled mathematically for the BCI. The model can be applicable to neuro-rehabilitation and mind controlled device. Eventually, the objectives of this research proposal are-

- To model the pattern of the neuro-activations of movement related tasks based on the motor planning activations from prefrontal fNIR signals.
- To establish statistical relationship between voluntary and imagery events to find the best possible regions of prefrontal cortex.
- To develop a CNN based predictive model for classification of voluntary and imagery tasks from fNIR data.
- To include EEG information with fNIR to cover frontal and central lobe for improving the effectiveness of CNN based predictive model for high performance multiclass BCI.

1.4 Contributions of the Proposed Research

This research work has been contributed into some significant areas of functional neuroimaging those can be presented briefly by the following points:

- ***A novel method to measure the voluntary and imagery movements:***
This research work proposes to measure the voluntary and imagery movements of hands and feet from the prefrontal hemodynamics, for the first, by a novel method. The hemodynamic properties regarding these voluntary and imagery movements in the prefrontal cortex have been widely examined with the proposed method and validated with several statistical methods.

- ***Activation modeling of voluntary and imagery movements:*** The activation pattern of the HbO₂ and dHb due to different voluntary and imagery movements are modeled using polynomial regression method from the prefrontal hemodynamics.
- ***A novel proposal to combine the fNIR and EEG signals for BCI applications:*** A novel approach of fNIR and EEG signal combination has been proposed and examined by this work. The proposed method combines the fNIR and EEG signals to prepare the neuroimages considering its spatiotemporal and time-frequency information.
- ***Development of a CNN based predictive model to classify multiple motor tasks from fNIR-EEG signals:*** A deep neural network, CNN has been deployed to build a predictive model for classifying combining information of fNIR and EEG signals regarding the voluntary and imagery movements. This novel approach can predict the movement activity from the fNIR-EEG signal (converted as the proposed combining method) with very high classification accuracy.

1.5 Organization of the Dissertation

Chapter 1 : Introduction

This chapter includes the motivations of this research work. The current research development and limitations regarding the motivations and further scopes to solve the existing limitations are widely discussed. In addition, this chapter deliberates the objectives of this research work. The fundamental contributions of this research work and organization of the Dissertation have been also mentioned briefly.

Chapter 2 : Optical and Electrical Techniques of Functional Neuroimaging

In this chapter the basic mechanisms of functional neuroimaging with the optical (fNIR) and neuro-electric (EEG) methods are widely explained. The related mathematical models and the fundamental

characteristics of the fNIR and EEG signals are also reflected by the contents of this chapter.

Chapter 3 : Signal Preprocessing Techniques

The processing techniques applied in this research work on fNIR and EEG signal are explained in mathematical and graphical manner to provide a clear conception about them. Several algorithms are explained here with a modified way to cope them with our proposed working methods.

Chapter 4 : Statistical Modeling of Voluntary and Imagery Movement

This chapter describes the one of our basic contribution on the statistical modeling of voluntary and imagery movements through multichannel fNIR signals. The mathematical models of voluntary and imagery movement related neuro-activations are presented in this chapter. In addition, the performance of fNIR modality to classify the movement related multiclass neuro-activations are extensively conferred.

Chapter 5 : Predictive Modeling by CNN through fNIR and EEG Signal

In this chapter, a novel method has been approached to combine the fNIR and EEG signal to make it a multimodal functional neuroimage. Using this proposed functional neuroimages of multiple movements related tasks are classified by CNN. The performance improvement in case of multiclass BCI through the proposed approach has been revealed by the contents of this chapter.

Chapter 6 : Conclusions and Future Perspectives

In this Chapter, we concluded all of the research work briefly. The main contributing objectives of this research work and the final outcomes are compared here comprehensively. The limitations of this work are also discussed and the probable solutions to overcome the limitations are mentioned. There is some recommended future research perspective for the future researcher so that this work can be improved further.

CHAPTER 2

Optical and Electrical Techniques of Functional Neuroimaging

2.1 Introduction

Functional brain imaging is different from other neuroimaging procedures like Computed Tomography (CT) and Magnetic Resonance Imaging (MRI). It provides the functional activities of the brain, not the structure of the brain tissue. By two basic methods, functional brain imaging can be performed: *i*) based on hemodynamic behavior (changes in the concentration of HbO₂ and dHb) and *ii*) based on electrical activities estimation from the scalp of the brain.

Recall that, based on the hemodynamic property, one of the finest functional neuroimaging modalities is fMRI. This modality offers a very high degree of spatial resolution. That's why it is possible to capture the functional images from the surface to very deeper brain. But, its temporal resolution is very poor [1]. In addition, this modality has some more limitations like its noise sensitivity, bulk size, huge cost, and most importantly it is physically confined for the subjects. As a result, fMRI is not suitable for practical BCI implication. On the other hand, fNIR is a functional brain imaging modality based on hemodynamics of the human brain in the superficial layer which provides some nice features like good spatial resolution (~1-1.5cm), moderate temporal resolution (up to 100Hz), portability to use, low cost, high value of SNR, and less motion artifact compared to fMRI [2]. Furthermore, fNIR is not as physically confining as fMRI and it allows more movements compared to fMRI during imaging. As a result, nowadays, fNIR is getting the most attention for the recent researches in the field of neuroimaging and BCI. Consequently, based on the cortical electrical activities, brain function measuring modality is EEG and magnetoencephalography (MEG). MEG is not widely used for functional brain imaging due to its high degree of sensitivity with environmental and magnetic interference [3]. That is why EEG is the best choice for BCI in the context of electrical method of functional neuroimaging. Though EEG has a very excellent temporal resolution, its spatial resolution is quite poor (5 to 9 cm) [4]. For proper BCI, both temporal and spatial information are necessary. Therefore, combined information of fNIR and EEG

signals can be a suitable solution for a highly efficient BCI. In this chapter, the basic methodologies of these two modalities (fNIR and EEG) are discussed with the origin and property of the signals.

2.2 The Fundamentals of fNIR

The most biological tissues are relatively transparent to light in the near-infrared range between 700 to 900 nm because the absorbance of the main constituents in the human tissue like H_2O , HbO_2 , and dHb is small in this range [5-6]. The absorbance coefficients of H_2O , HbO_2 and dHb as well as their optical windows in NIR are given in **Figure 2.1**. When an amount of NIR light is shone through the human scalp, the injected photons of that light follow various paths inside the head. Some of these photons are absorbed by skin, skull, and the brain tissue. Rest of the photons exit the head after following the so-called “banana” shaped path due to scattering effect of the tissue [7, 8]. The main absorbers in the NIR range are blood chromophores of HbO_2 and Hb whereas water and lipid are relatively transparent to NIR light. Therefore, changes in the amplitude of backscattered light can be represented as the changes in the blood chromophore concentrations. The estimating technique of the Hb and HbO_2 concentrations by means of near infrared light is called fNIR.

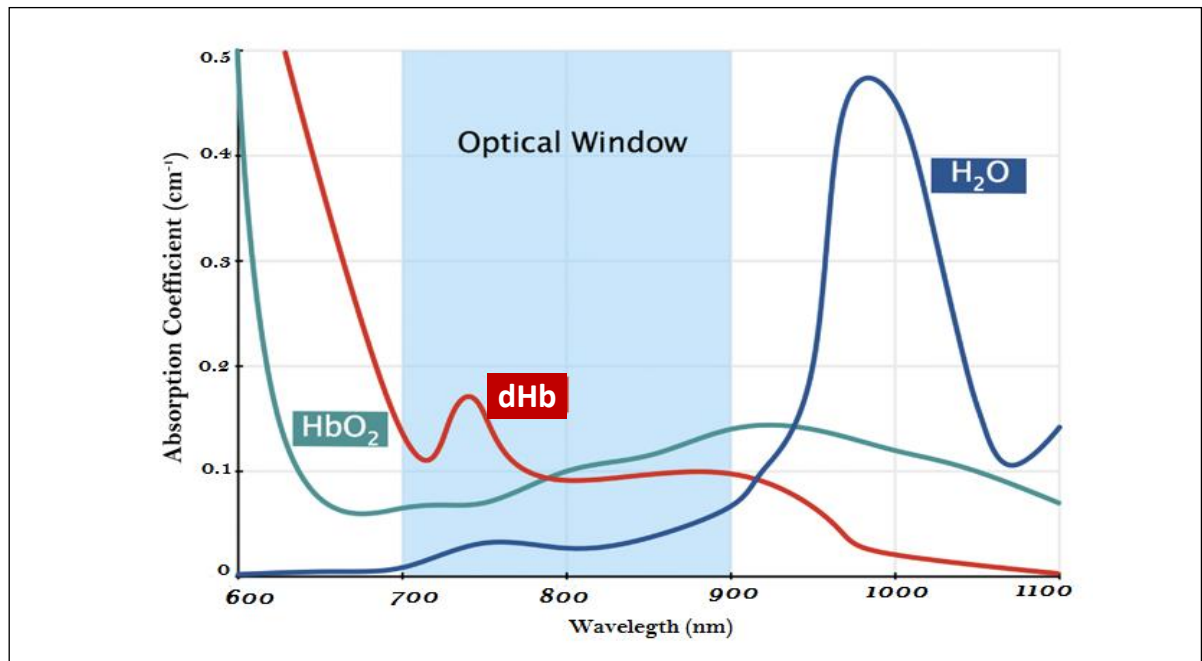


Figure 2.1: Absorption coefficients of H_2O , HbO_2 , and dHb [5].

2.2.1 Oximetry & Hemodynamic Response

According to the change in cognitive activity results the variation in the concentrations of HbO_2 and dHb in the brain tissue. This relationship is not surprising, since cerebral hemodynamic changes are related to functional brain activity through a mechanism called neurovascular coupling [9, 10]. When any part of the brain becomes activated to send some signal to perform any physiological or psychological work, the neurons of that area need energy. To supply proper energy to that area, it is necessary to metabolize the glucose available there. On the other hand, to metabolize the glucose oxygen is necessary. The need of oxygen is supplied by the blood. The hemoglobin, Hb existed in blood combines with oxygen and transformed itself as HbO_2 and transports oxygen to that area. Through capillary bed HbO_2 releases O_2 and transformed itself as dHb again which is also known as deoxidized hemoglobin [11, 12]. Therefore, indirectly we can say that increased rate of HbO_2 and decreased rate of dHb in a specific area indicates the activation of that area. This mechanism of neural activation and concentration change of HbO_2 and dHb is called hemodynamics [13, 14]. The aforementioned mechanism is illustrated in **Figure 2.2**.

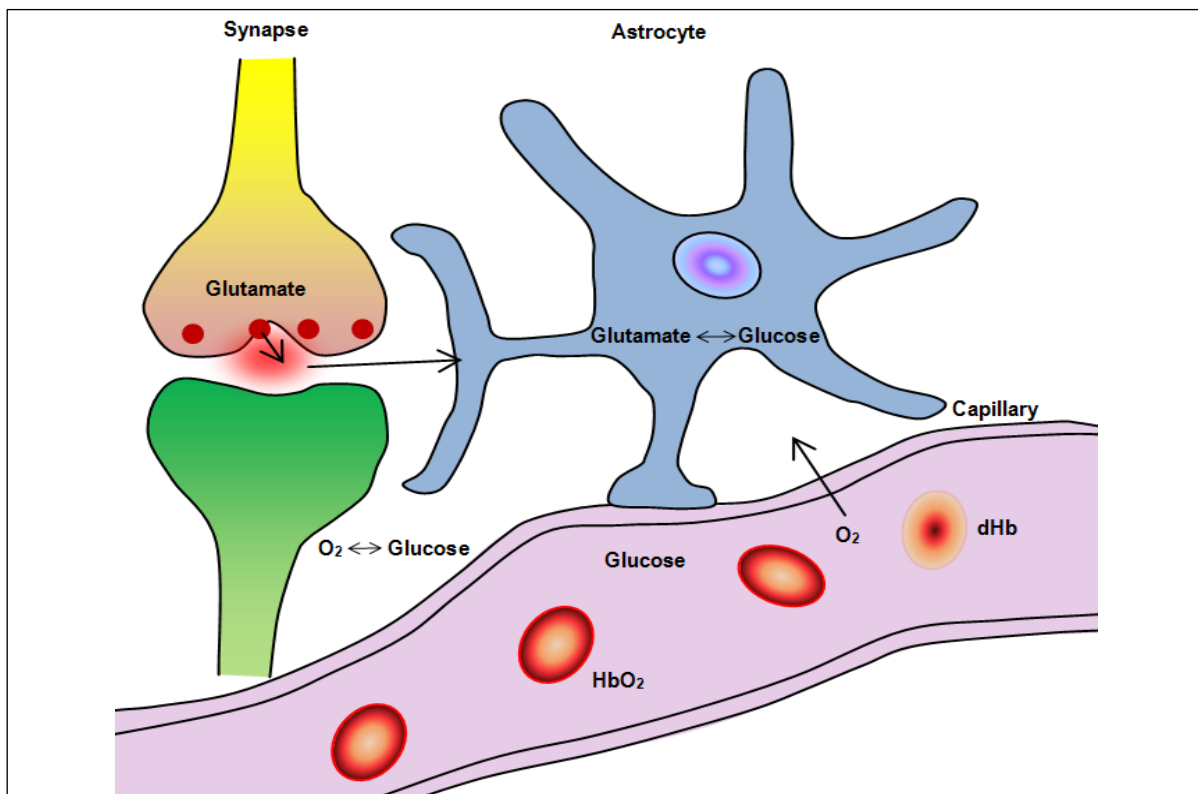


Figure 2.2: Relation between hemodynamic response and oxygen concentration [15].

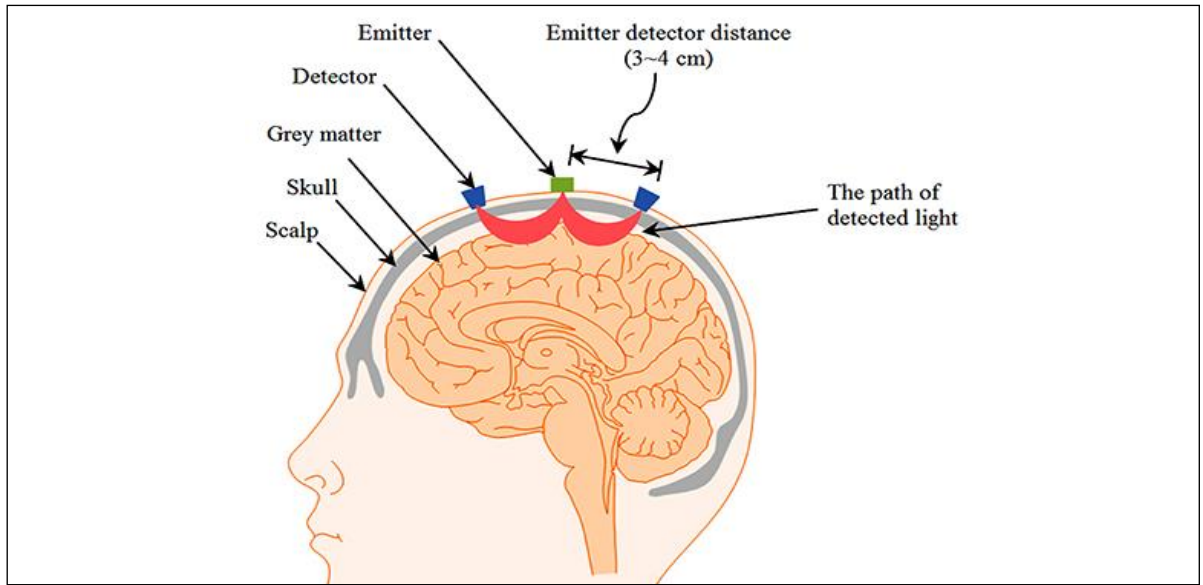


Figure 2.3: Position of NIR source and detector on human scalp [11].

2.2.2 Optical Measurement

In practice the detector and the NIR emitter diode are placed 3-4 cm apart as **Figure 2.3**. As NIR light enters the cerebrum, it traces a banana-shaped path from NIR emitter to detector like **Figure 2.3**. An array of sources and detectors, secured in a headband such as 16 channel fNIR as in **Figure 2.4**, allows the hemoglobin concentrations measurement at various places in the cerebrum. Using the modified Beer-Lambert law, the attenuation of light between the source and detector can be formulated as [16, 17],

$$I_{out} = I_{in} 10^{-OD_{\lambda}} \quad (2.1)$$

Here OD_{λ} is the optical density at the wavelength, λ . The term optical density is generally used in optical spectroscopy that describes the propagation of light wave through a medium. Mathematically, it is a logarithmic ratio of the falling light intensity to the incident intensity through a material. Therefore, according to the previous definition the optical density can be found as,

$$OD_{\lambda} = -\log \frac{I_{out}}{I_{in}} = attenuation = A_{\lambda} + S_{\lambda} \quad (2.2)$$

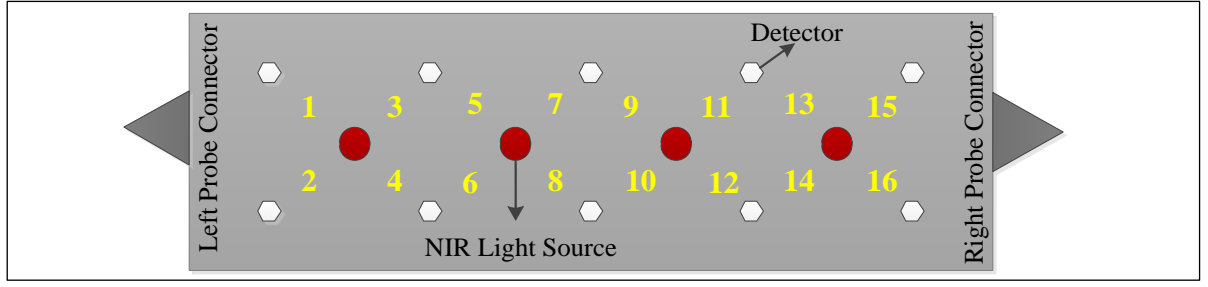


Figure 2.4: Optode and channel configuration of fNIR devices (Model 1200) head band [12].

Here A_λ and S_λ are the absorbing and scattering factors, respectively. In this case, main absorbers of light are blood chromophores HbO₂ and dHb in the NIR spectra. Therefore, absorption of light can be formulated as [17],

$$A_\lambda = \sum_{i=Hb, HbO_2} \varepsilon_{i,\lambda} C_i L_\lambda \quad (2.3)$$

In (2.3), $\varepsilon_{i,\lambda}$ is the specific extinction coefficient of blood chromophore for wavelength λ and C_i is the concentration of blood chromophores and L_λ is the path-length of light at λ . Path-length is a very important parameter which can be expressed in terms of source detector separation as [17],

$$A_\lambda = d \cdot DPF_\lambda \quad (2.4)$$

In (2.4), d is the linear difference between the light emitter and detector and the DPF stands for differential path factor. Differential path-length factor is the actual factor to correct the proper length of the light travels. DPF can apparently calculated as [17],

$$DPF_\lambda \approx \frac{1}{2} \left(\frac{3\mu'_{s,\lambda}}{\mu_{a,\lambda}} \right) \quad (2.5)$$

where μ_a is the absorption coefficient, and $\mu'_{s,\lambda}$ is the reduced scattering coefficient at wavelength λ .

To remove the effect of scattering two successive measurements, yield the differential value of optical density and the procedure can be described as,

$$\begin{aligned} OD_\lambda &= OD_{\lambda,final} - OD_{\lambda,initial} \\ &= \sum_{i=Hb, HbO_2} \varepsilon_{i,\lambda} \Delta C_i \cdot d \cdot DPF_\lambda \end{aligned} \quad (2.6)$$

Now the effect of scattering is cancelled. Since each chromophore has a specific extinction coefficient and differential pathlength factor, measurement with two wavelengths leads to:

$$\overline{\Delta OD} = \overline{M} \times \overline{\Delta C} \quad (2.7)$$

Where the values of OD , C , and M are given below.

$$\overline{\Delta OD} = \begin{bmatrix} \Delta OD_{\lambda_1} \\ \Delta OD_{\lambda_2} \end{bmatrix} \quad (2.8)$$

$$\overline{\Delta C} = \begin{bmatrix} \Delta C_{HbO_2} \\ \Delta C_{dHb} \end{bmatrix} \quad (2.9)$$

$$\overline{M} = d \times \left(\begin{bmatrix} \varepsilon_{HbO_2, \lambda_1} & \varepsilon_{HbO_2, \lambda_2} \\ \varepsilon_{dHb, \lambda_1} & \varepsilon_{dHb, \lambda_2} \end{bmatrix} \times \begin{bmatrix} DPF_{\lambda_1} & 0 \\ 0 & DPF_{\lambda_2} \end{bmatrix} \right)^T \quad (2.10)$$

From (2.8) we get a transformation from light output change to change in blood chromophore concentrations. Using the blood chromophore concentrations as given in (2.9), we can define two other parameters; those are oxygenated blood concentration (OXY) and blood volume (BV) by the following relations,

$$OXY = \Delta C_{HbO_2} - \Delta C_{dHb} \quad (2.11)$$

$$BV = \Delta C_{HbO_2} + \Delta C_{dHb} \quad (2.12)$$

2.2.3 The Characteristics of fNIR Signals: Basically, from the measurement of hemodynamics in the form of optical signal, MBLL gives us the value of dHb and HbO₂ concentration. From the higher concentration of HbO₂ or the lower concentration of dHb, we come to know the activation of the region of human brain because the HbO₂ and dHb signal always shows the negative correlation. The continuous raw (containing physiological noises) fNIR signals (HbO₂ and dHb) for a particular mental activity of a specific channel are given in **Figure 2.5**. In this figure, it can be found that the signals are negatively correlated. Generally, the raw fNIR signals are mixed with some physiological noises. When we are interested to remove the noise from fNIR signal, it is obvious to know the frequency spectral characteristics of fNIR signal. The power spectral density (PSD) of a typical fNIR (HbO₂) signal has been given in **Figure 2.6**. From the spectral information of fNIR

signal, it is generally expected to contain four frequency bands centered on 0.7Hz, 0.2Hz, 0.1Hz, and 0.03Hz [18] - [20]. The neural activation due to hemodynamic response is embedded in the 0.1Hz and 0.03Hz bands. The 0.8Hz and 0.2Hz bands are corresponding to the heart rate and respiration, respectively.

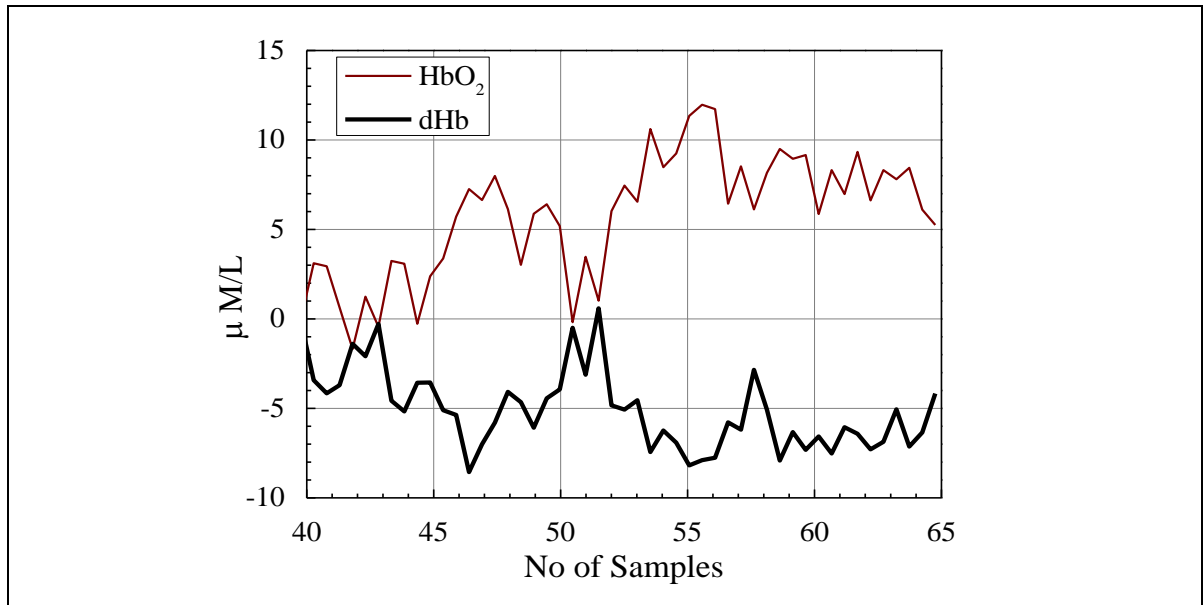


Figure 2.5: Example of raw fNIR signal (both dHb & HbO₂) of a particular channel. It is easily discernable that these two signals are negatively correlated.

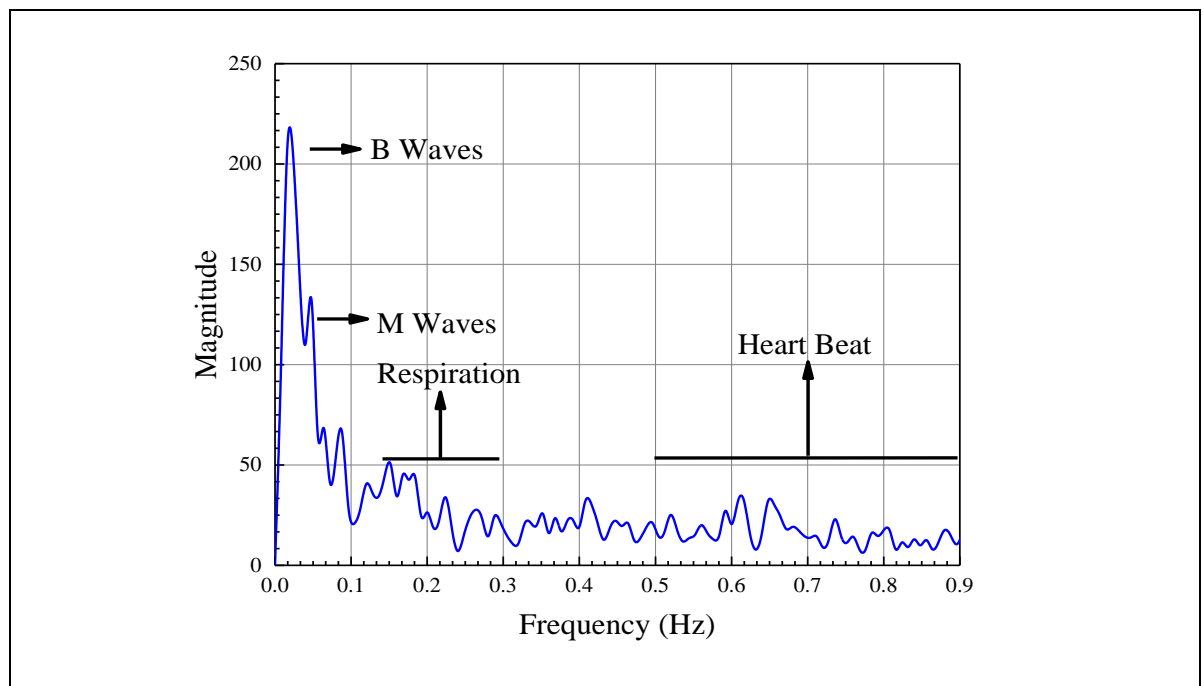


Figure 2.6: The PSD of an fNIR (HbO₂) signal. The magnitudes are not normalized in this figure. The numerical values of frequency spectra are connected by b-spline interpolation.

The 0.03Hz band is known as B-waves and it is very low frequency oscillations (VLFO). It is assumed to reflect the periodic variations generated by the various brain stem nuclei in the vasomotor tone of cerebral arterioles [21]. The 0.1Hz band consists of vasomotive signal (rhythmic dilation and contraction of the pre-capillary sphincters in the cortical capillary beds), B wave, and M-wave. Therefore, this band is considered by far the most influential spectral band on event related optical signal. In this circumstance, different researchers [22-29] proposed to remove noise by considering different frequency bands like 0-0.1 Hz, 0-0.14 Hz, 0.03-0.1 Hz, etc. In this work, all fNIR signals are filtered to remove all the signal components greater than 0.1Hz with a low pass 20 order FIR filter or its equivalent Savitzky-Golay (SG) filter as instructed in [30].

2.2.4 Hemodynamics of Voluntary and Imagery Movements

A number of stimuli have been used for BCI purpose such as arithmetic test, mental work load, visual stimuli, auditory stimuli, etc. The review work [31] has shown that the mostly used stimuli for BCI purpose are motor imagery. All other stimuli except motor imagery need some extra staffs for creating the proper stimuli for neuro-activation. Since we move our upper and lower limb all the time of our consciousness, this work is very easy to consider as neural stimulation as well as it needs no basic training for the participants. The movements we actually execute by our voluntary muscles are called voluntary movements (like movement of hands, feet, tongue, head, finger, etc.) but the planning of the movements of any organ is called imagery movement which is a mental work, actually.

The voluntary movement of an organ of our body is controlled by our brain with a series of tasks. When we think to move an organ, the motor area of prefrontal cortex make a suitable plan for that movement and send a message to the motor cortex which is situated in the central part of our brain. This motor cortex is the lateral part of the frontal lobe. The motor neurons become excited and activated with the frontal cortex message and send the command to the specific voluntary muscle to perform the task [32]. Suppose that the task is to grab a pen or a cup. When we touch the pen and cup, the sensory motor neurons get a message from the muscle nerves and the brain decides the performance of the voluntary movements. Such a procedure is given in **Figure 2.7** illustrating the neural connectivity mechanism of

the planning to completion the voluntary movement related tasks. Therefore, we found that there is a relation of voluntary movement related hemodynamic activation in prefrontal and frontal cortex. There are several research works those have shown that the imagery movements create same pattern of hemodynamic activation properties with lower activation level. The activation of voluntary and its imagery movement are created in a same place of the brain. One of the significant research works [33] compared the activations of voluntary and imagery movement of hands from the primary motor cortex, somatosensory cortex, and prefrontal cortex by fNIR modality. The main outcomes of this research work were presented by two significant graphs. The corresponding research outcomes of this research work are reproduced and presented in **Figure 2.8** and **Figure 2.9**.

From the results we find that in both movement of left hand and right hand in voluntary and imagery manner create activation in both the left and right lobe of the brain. In ever cases, it is clearly observable that the voluntary and imagery movements created almost similar activation pattern but the activation strength of the voluntary movements are higher than that of the imagery movements. In addition, the left hand imagery movement creates the stronger activation in the right lobe of the brain and vice versa. In result, the important information about the neuro-activation is that the concentration change in the HbO_2 is much greater than that of the concentration change of dHb in every case and in every lobe.

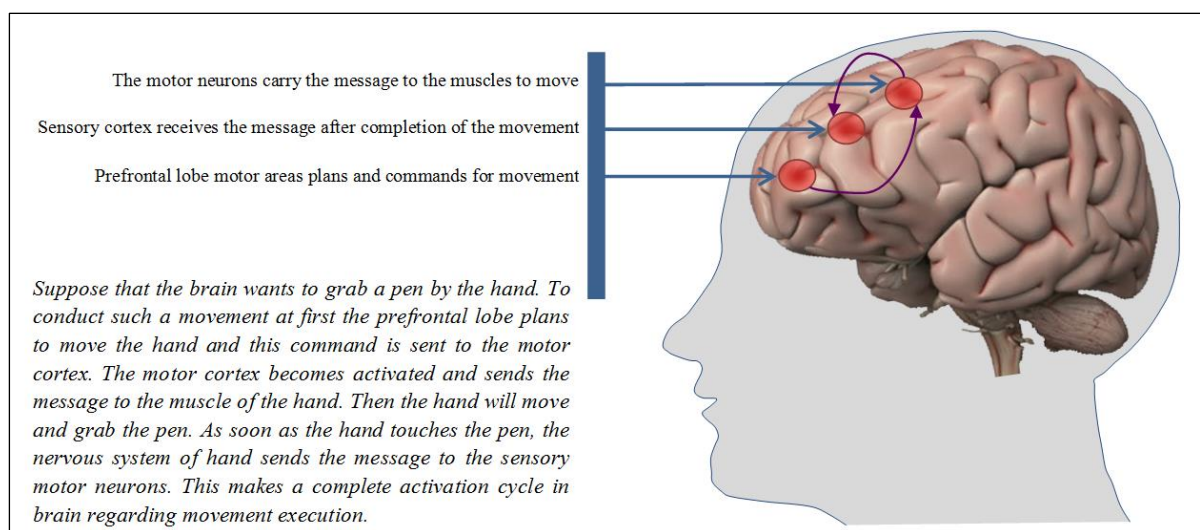


Figure 2.7: The movement related brain activations and the significance of the brain lobes in cyclic operations of a complete movement cycle.

The results given in **Figure 2.9**, describes that the activation pattern in PFC, MI, and SMC are similar. In some cases, their activation strengths are also same for both the voluntary and imagery movements. The hemodynamic properties of these three regions of interest (ROI) are correlated to each other. Therefore, for a significant discriminative signal acquisition we should not concentrate on the central lobe, only, it is also necessary to consider the hemodynamic pattern of the prefrontal cortex as well. This consideration is assumed to be more significant for multiple class stimuli like feet movements in imagery manner. In addition, since the imagery movement is one kind of mental activities there should be a strong correlation of the mental workload to the prefrontal lobe.

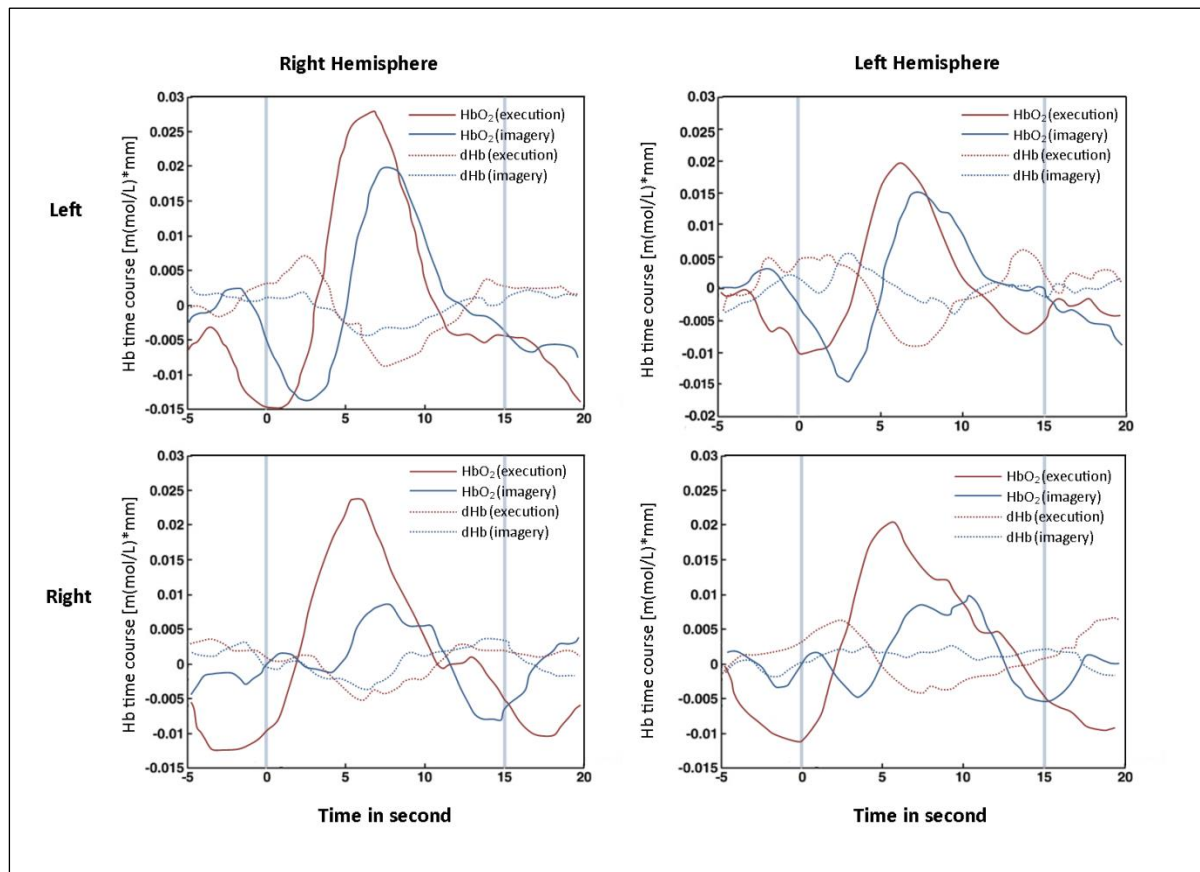


Figure 2.8: These results are based on the 5 sec tasks + 20 sec hemodynamic observation. Here, the mean activation changes in HbO₂ (solid lines) and dHb (dotted lines) regarding the response of a left and right hand movements in both voluntary and imagery manner. The most significant channel information about mean activation changes in HbO₂ and dHb has been represented for both hemispheres: right hemisphere (left panel) and left hemisphere (right panel) [33].

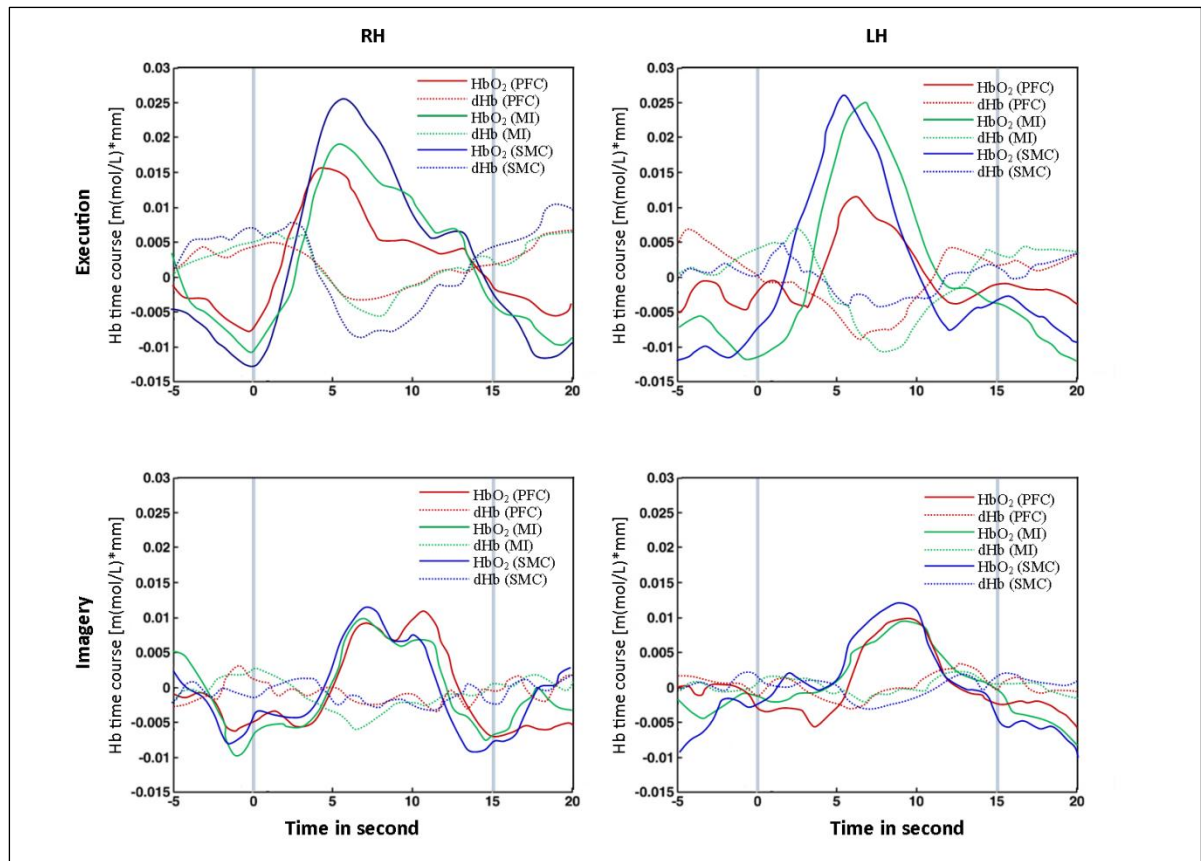


Figure 2.9: The change in concentration of HbO₂ (solid lines) and dHb (dotted lines) for right hand (left panel) and left hand (right panel) movement execution (upper panel) and imagery (lower panel) of three positions of interest: prefrontal cortex (PFC); primary motor areas (MI); somatosensory motor areas (SMC) regarding the left and right hand movement for both voluntary and imagery tasks [33].

2.3 Fundamentals of Electroencephalography (EEG)

A human brain consists of more than 100 billion neurons (unit of brain cell). The connections among these neurons make the complex path and communicate with each other. These communication procedure is electrical that means they communicate with each other by electrical impulses. Therefore, the neural activation of a specific region means indirectly the higher rate of change of electrical activities. The method electroencephalogram or EEG is actually the recording of this change of electrical potentials generated by activation of the neurons of the human cerebral cortex. In this section we describe the procedure of the EEG generation and its fundamental properties.

2.3.1 How is EEG Generated?

There are two types of cells in our brain those are called nervous cells or neurons and glial cells. In case of the both cells, the resting potential is nearly -80mV. The

difference of the concentration of cations: Ca^+ , K^+ , Na^+ and anions: Cl , large organic anions create this potential difference. Actually, the difference of potential is sustained by the active cation K^+ to the inside of the cell and Na^+ to the outside of the cell using the energy provided through the metabolic processes.

Electric activity of neurons is demonstrated by production of action potentials and postsynaptic potentials (PSP). Action potentials are occurred when the electrical excitation of the membrane surpasses a threshold. PSP are the sub-threshold phenomena. The action potential generation is correlated with the prompt increase of permeability for Na^+ ions. The consequent influx causes a prompt increase the inside cell potential and the polarity changes from negative to positive (about +30 mV). Therefore, a subsequent increase is occurred in membrane permeability of the K^+ ions and a decrement is occurred in the permeability of the Na^+ ions. This makes negative the inside of the cell, again compared to the surrounding medium. Such a way, action potential of spike-like shape characteristic is produced. It obeys the “*all or nothing*” rule. This rule can be concluded as: “*For supra-threshold stimuli, a pulse of constant amplitude is generated and for sub-threshold excitation, the neuron doesn't fire*” [34].

If we want to visualize and monitor the microvolt range of cerebral electrical activity (common EEG pattern in temporal domain), there must be a sufficient duration with sustained strength. To place it inappropriately, one has to catch a platform on which both the examiner and the examined brain discover themselves in the similar time-space scale. Only synaptic activity willingly achieves those principles and is most important foundation of EEG potentials. The synapse of the brain tissue works like a battery driving current in a small loop. Both excitatory postsynaptic potentials (EPSPs) and inhibitory postsynaptic potentials (IPSPs) subsidize to the synaptic activity logged as EEG [35]. A demo procedure has been given in **Figure 2.10**.

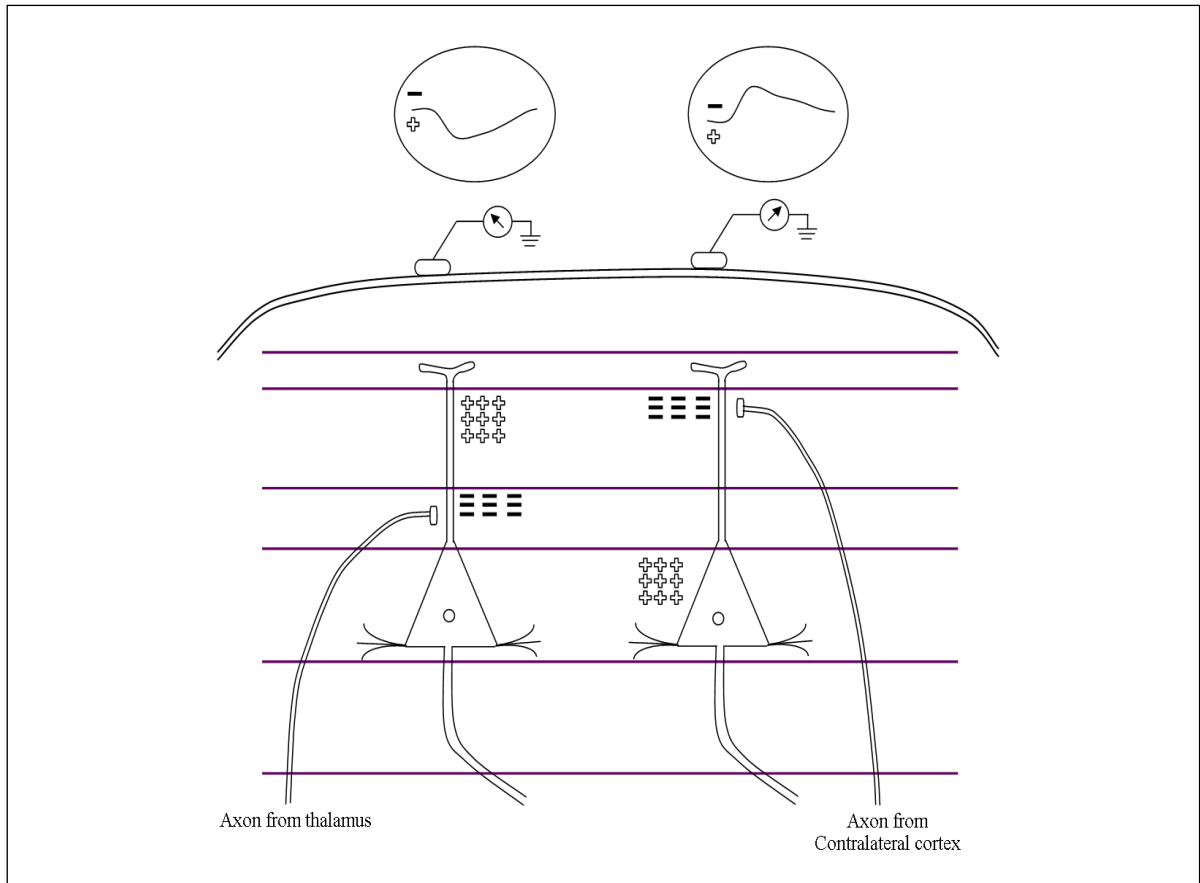


Figure 2.10: The procedure of the extracellular voltage field generation from graded synaptic activity [34]. Here, the relationship between the polarity of site of dendritic PSP and surface potentials has been illustrated.

2.3.2 EEG Acquisition Method

For measuring EEG signal from cerebral cortex, electrode placement is a major concern. For noninvasive recording of EEG signal, 10-20 system is the most widely acceptable technique. To understand the electrode placement on the scalp of human brain according to the international 10-20 system we have presented the following illustration which is given in **Figure 2.11**. This figure represents the external circle at the level of the nasion and inion. The inner circle represents the temporal line of electrodes. This illustration is responsible for an advantageous stamp for the sign of electrode placements in tedious recording. The “10” and “20” are inter-electrodes distances that is either 10% or 20% of the total front-back or right-left distance of the skull based on the number of the electrodes [36, 37].

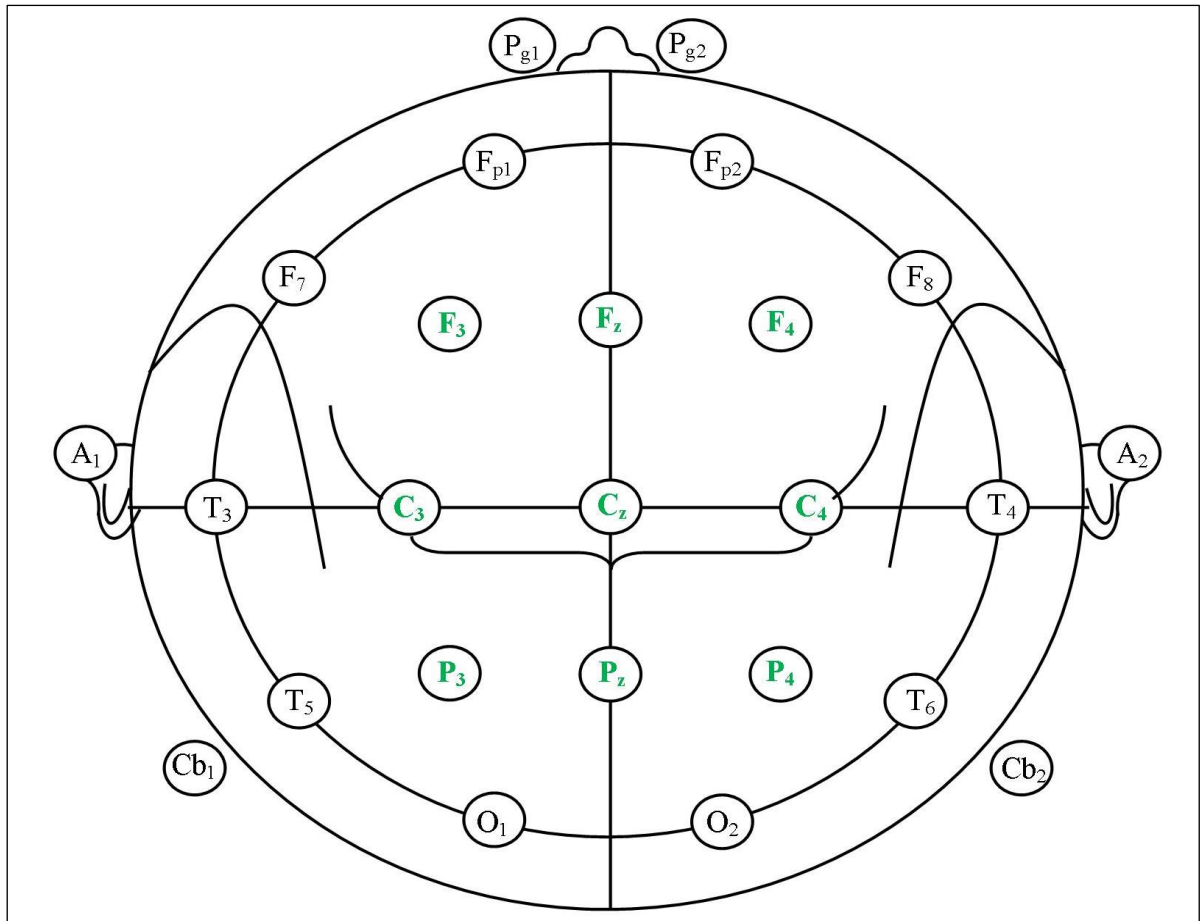


Figure 2.11: A single plane projection of the head, showing all standard positions and the location. This figure is redrawn according to the recommendation of the international federation [38].

2.3.3 Rhythmic Properties of EEG Signal

The EEG signals are often regarded as a random signal. But the information of EEG signal is often described by its rhythmic activities and transients. The rhythmic activities are associated with some specific frequency bands and they play crucial role to make the EEG signals meaningful. The major frequency bands of EEG signals are characterized by the name Delta, Theta, Alpha, Beta, and Gamma. Here, these bands with frequency limit and their characteristics have been shown in **Figure 2.12**.

Delta (δ): This rhythmic activity is found in frequency ranges between 0.5 to 3 Hz. Generally, the amplitude of this band is between 100 and 200 μ V in amplitude. Delta band signals are mostly dominant in frontal lobe and regarded as the highest in amplitude and the slowest in waves. The delta rhythm is primarily responsible for

the mental states related to deep sleep, unconsciousness, serious brain disorder, and waking [39].

Theta (ϑ): The theta band components are found in frequency ranges within 4 to 7 Hz with amplitude of less than $30 \mu\text{V}$. Theta waves are originated in the central and temporal lobe of the human cortex and it is considered that this band is responsible for drowsiness, resting with eyes close, emotional stress or frustration, and deep meditation [39].

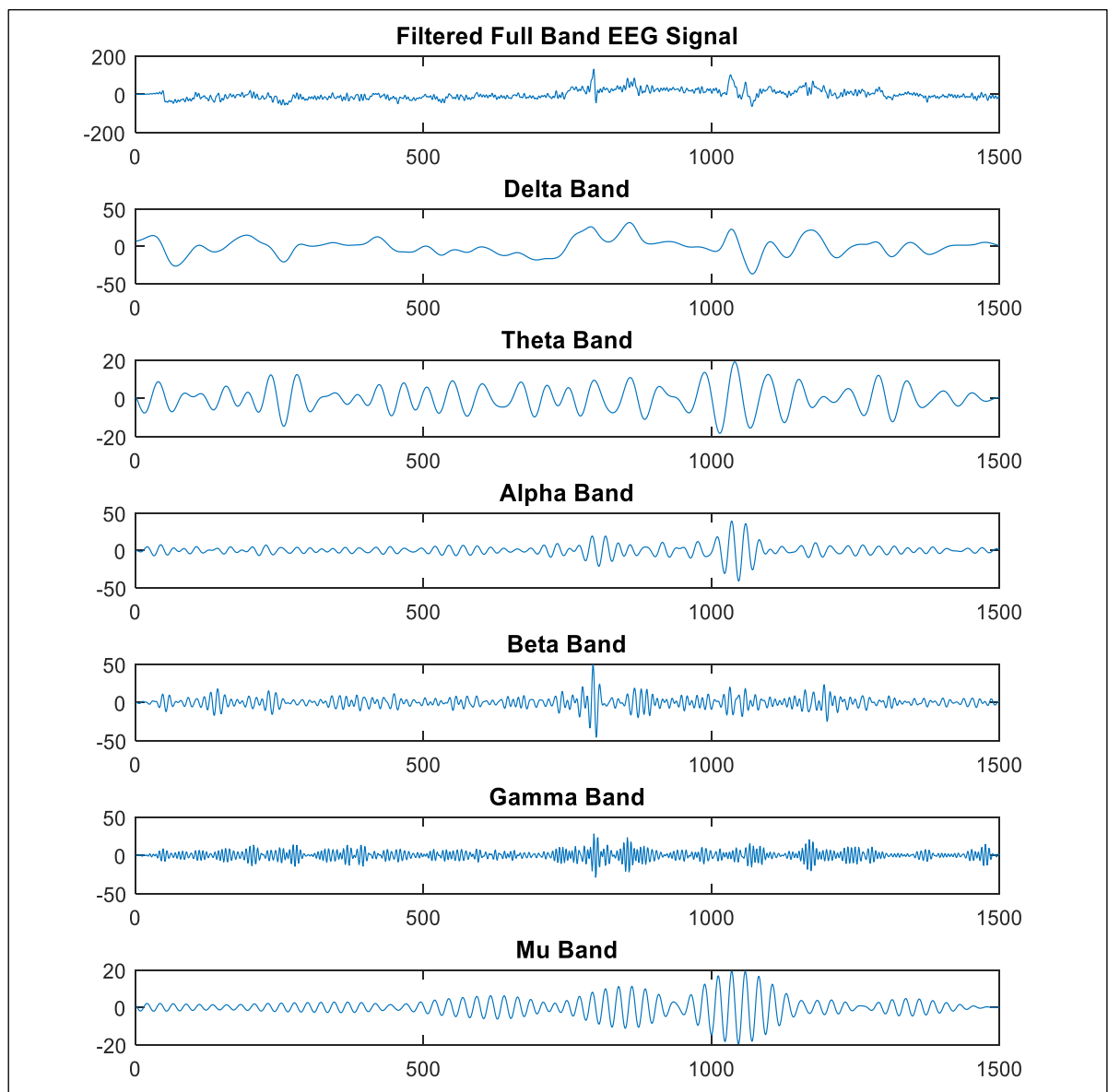


Figure 2.12: A typical full band EEG signal and its different rhythmic band signals.

Alpha (α): Frequency ranges from 8 to 13 Hz are regarded as the alpha band. Alpha band signal's amplitudes are found within the amplitude of 30-50 μ V. This band appears in all over the cerebral cortex which is typically concomitant when a person is in a relaxed state or in stress and tension. When a person awake from the resting state and starts to think, blink then α waves disappear. This is called alpha block. If a person is active with eyes open, α power remains low and in resting conditions with eyes closed, α power increases [40].

Beta (β): The frequency range of beta band lies within 14 to 30 Hz with low amplitude (5-20 μ V). Beta band is generally generated in the frontal area as well as in the parietal lobe. When the brain is actively engaged with mental activities (concentrating, thinking, alert), it generates beta waves [41].

Gamma (γ): This electromagnetic wave has the frequency above 30 Hz with amplitude of between 5 to 10 μ V. It is connected with several cognitive activities, perceptual tasks, and motor functions [39].

Mu (μ): The range of μ is considered 10–12 Hz. It is observed that μ partially overlays with other bands. During resting state it replicates the synchronous firing of motor neurons. The summation of the power of the mu and beta rhythms calculated from common spatial pattern is closely related to the event-related phenomena like imagery movement [42, 43].

2.3.4 Noise Sensitivities of EEG signal

EEG signal is very noise sensitive signal. During data acquisition power line noise (50Hz or 60 Hz) is surely incorporated with EEG signal. In addition to that, some other artifacts are also induced in EEG signal those are created from cardiac activity, electrode displacement, muscle artifact, and ocular artifact. These artifacts have some illogical distribution. It is very important to remove these artifacts from EEG signal for further processing or application. Some artifacts can be primarily removed like electrode displacement. With proper caution and concern can save the signal from such artifacts. Cardiac activity is a slow process that can be easily removed by high pass filtering technique.

The major concern about artifact removal from EEG signal is ocular and muscle activity or electrooculography (EOG) signal impurity removal. To remove the EOG impurity from EEG signal, the most logical technique is to use a separate channel that can be capable to acquire only EOG signal. The distribution of EOG is quite dissimilar to EEG signal. Therefore based on the information of EOG, we can apply ICA (Independent Component Analysis) to extract the EOG impurity from EEG signal and remove it [44, 45].

2.3.5 Spatiotemporal Resolution of EEG

EEG signal has a very high temporal (~10ms) resolution but its spatial resolution is poor (3-6 cm). Due to very high temporal resolution still EEG technology has a great importance in the field of BCI. Nonetheless, the main concerning issue is its spatial resolution. Because of poor spatial resolution it is quite difficult to allocate the position of different physical or mental activities. As a result misclassification can be often occurred for multiple event classification. Modern researchers suggest that the information of EEG signal can be added to the fNIR signal. This combination or hybridization of fNIR and EEG signal would be nice approach to take challenges of spatiotemporal resolution. Eventually, it can be assumed that the combination of fNIR and EEG signal in appropriate way facilitate to find the high classification accuracy during multiple class classifications.

2.3.6 EEG Signal Behavior for Imagine Movement

A number of research works [43, 46-48] based on movement classification by EEG signal have claimed that the activation related to voluntary and imagery movement is occurred in the motor area of the human brain. Motor area is the part of frontal lobe as given in **Figure 2.13**. It is actually situated in the central part of our cortex. Therefore, the channel named by Cz, C3, and C4 are closely associated to the activation acquisition through EEG. It is also found from some research work that there is some activation occurred in the frontal lobe as well. The channel named by F3, Fz, and F4 are also necessary to consider for the EEG signal acquisition of multiple motor tasks. Most of the researchers designed their classification mechanism by the feature extraction of these channels among multiple channels regarding EEG acquisition.

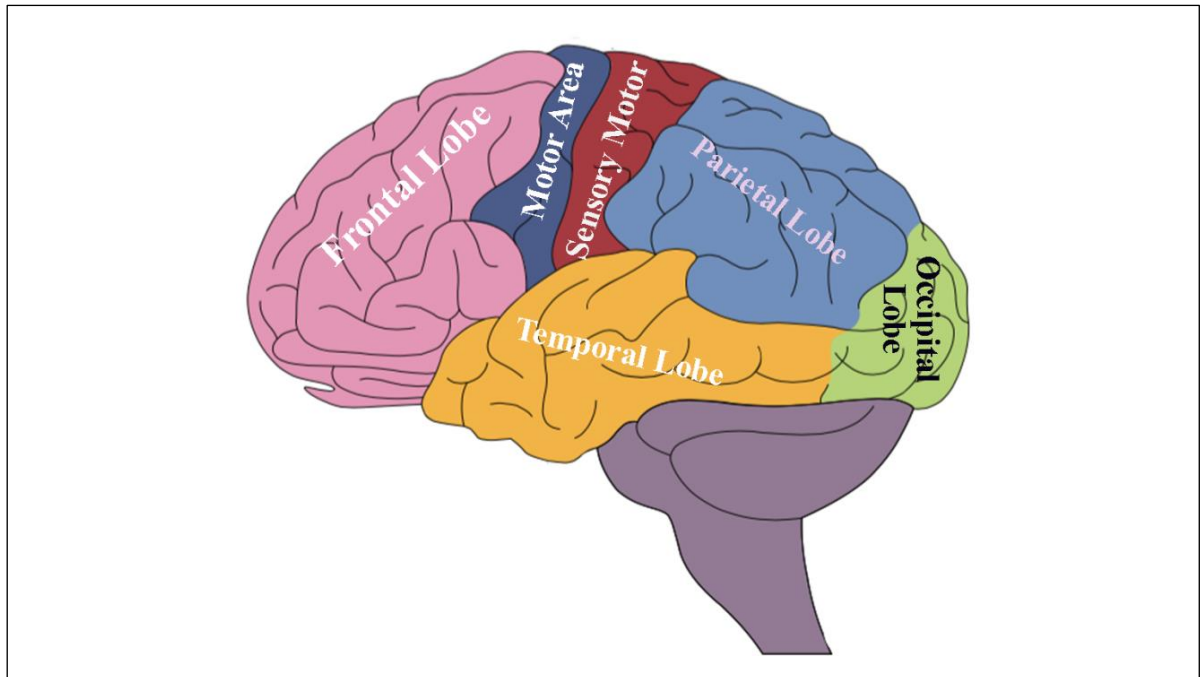


Figure 2.13: Human brain and its major lobe allocation.

Generally, the movement of voluntary and imagery influent the band are mostly responsible in the alpha and beta band. In this work, the PSD of alpha and beta separately calculated with time series EEG signal with a suitable window range so that the variation in the power level of the EEG signal due to voluntary and imagery movements can be observed. Finally, it has been added to the fNIR signal to produce the neuroimages.

2.4 Conclusion

This chapter has been presented the basic mechanism of the optical and electrical neuroimaging methods in the context of fNIR and EEG modality. In addition, the acquisition technologies with multiple channel information from the brain are discussed in this chapter. The voluntary and imagery movement related changes in the neuro-electric and hemodynamic aspects are also widely presented in this chapter. In the next chapter, we would like to present the processing steps of the fNIR and EEG signal with their mathematical interpretations.

CHAPTER 3

Signal Preprocessing Techniques

3.1 Introduction

This chapter describes different signal processing techniques regarding this thesis work. Since this research work is associated with both the fNIR and EEG signal, the signal processing techniques to achieve the objectives of this dissertation are elaborately discussed in this chapter. The mathematical clarifications about the signal and image processing techniques, classification methodologies, combinations of fNIR and EEG signal to prepare the neuroimages are discussed widely. The methodologies of this chapter are implemented for the results found in Chapter 4 and Chapter 5.

3.2 fNIR Signal Processing

In the context of fNIR signal preprocessing, several techniques are necessary to be performed to make it ready for further analysis like filtering, baseline correction, compression, feature extraction, classification, modeling, etc. The preprocessing steps are to perform in chronological order and this series of signal processing methods are to perform as presented by the following flow diagram in **Figure 3.1**.

At first, the raw fNIR signal is tested to check its perfectness in the context of signal quality. Generally, in this case sliding window motion artifact rejection algorithm (SMAR) [1] is applied to the raw signal to reject the effect of motion artifact from the signal. After that, signal is sometimes compressed to reduce the dimension of the signal based on the similar correlated characteristics of the signals.

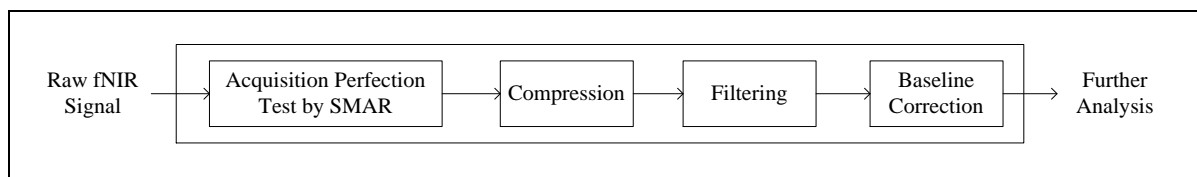


Figure 3.1: Preprocessing steps of raw fNIR signals and their chronological order.

3.2.1 Motion Artifact Rejection by SMAR Algorithm

Sometimes the acquired fNIR signals can be infected by head movement and some special noises are introduced in raw fNIR signals. Due to the motion of participant during optical brain imaging through fNIR causes coupling or the changes of pressure in the light sources and detectors. This reason and its corresponding effect can be captured within the raw fNIR signals as noise. This noise is found as spikes or burst noise with much higher or lower amplitudes than regular cortical activity.

Additionally, the temporal sequences of these abrupt variations by reason of motion artifact in the raw fNIR signal are much faster than the typical raw signals. Sliding-window motion artifact rejection or SMAR algorithm can scan the fNIR signal to identify the segments with such characteristics. This algorithm measures light intensity at two different wavelengths (730nm and 850nm) and also a dark current condition to estimate the existence of any possible ambient light leakage. The detail mathematical interpretation regarding the SMAR algorithm is given in appendix section.

3.2.2 Compression

Since the data are acquired with 16 channels, the processing could have faced the curse of high dimensionality. To check the actual dimensions, the data was transformed by principal component analysis (PCA) and we found that the actual dimensions of the signals are 4 instead of 16. The result of PCA has been shown in **Figure 3.2** with the similar channel numbers of ilk dimension. The resulting 4 dimensions are termed as Left Lateral (LL: channel 1, 2, 3, 4), Left Medial (LM: channel 5, 6, 7, 8), Right Medial (RM: channels 9, 10, 11, 12), Right Lateral (RL: channels 13, 14, 15, 16). The signals having the same dimensions are to average which is also known as common averaging method. Therefore, the 16 channel information become compressed from $i \times 16$ to $i \times 4$. This compression helps to reduce the feature dimension which is very important for achieving high classification accuracy in machine learning approach.

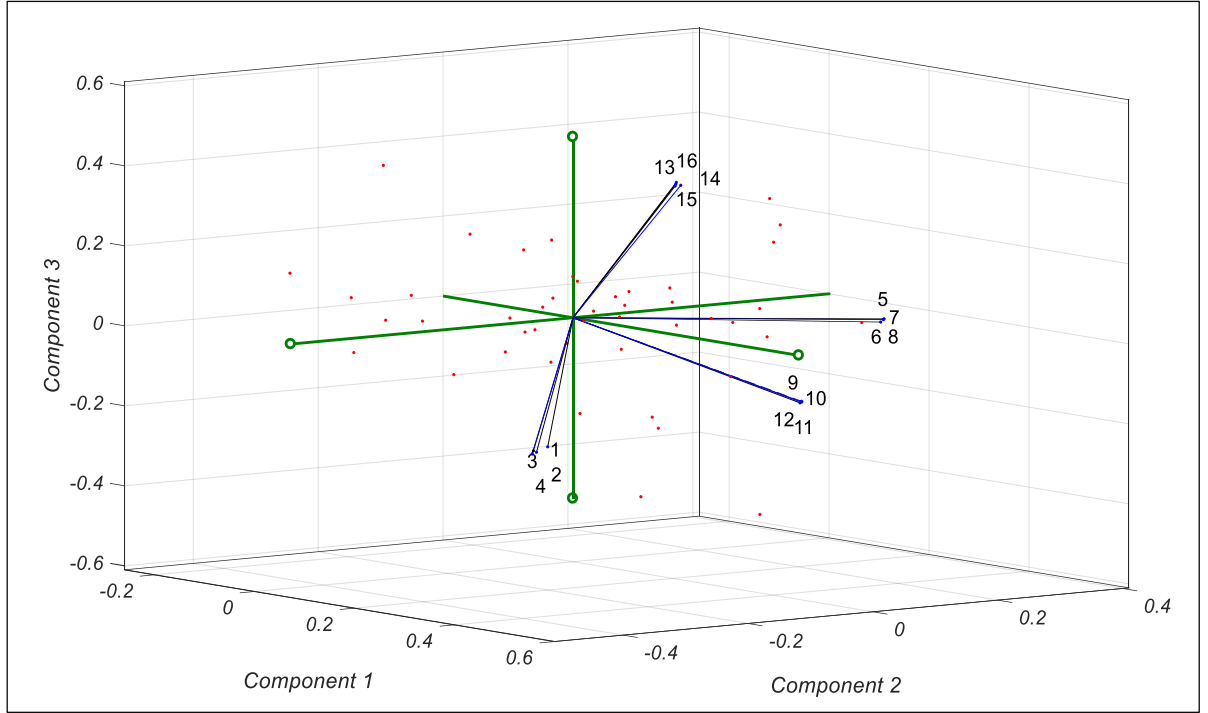


Figure 3.2: This figure presents the actual signal dimensions in Eigen-space which is formed by the three principal components of PCA analysis. The figure shows four linearly uncorrelated solution vectors with the channel number.

Therefore, the prefrontal cortex can be divided into four major areas of interest those are- LL, LM, RM, and RL. [2]. It is found that the 4 signals corresponding four channels in every defined region show very strong correlation ($0.95 < r < 1$). Therefore, these four signals can be averaged to compress the total dimension $i \times 16$ to $i \times 4$. Here, i means the sample number. If, a signal, $X(N)_{i \times 16}$ is of $i \times 16$, then the procedure to reduce its dimensions according to the previous description as,

$$LL(N)_{i \times 1} = \frac{1}{4} \sum_{k=1}^4 X(N)_{i \times k} \quad (3.1)$$

$$LM(N)_{i \times 1} = \frac{1}{4} \sum_{k=5}^8 X(N)_{i \times k} \quad (3.2)$$

$$RM(N)_{i \times 1} = \frac{1}{4} \sum_{k=9}^{12} X(N)_{i \times k} \quad (3.3)$$

$$RL(N)_{i \times 1} = \frac{1}{4} \sum_{k=13}^{16} X(N)_{i \times k} \quad (3.4)$$

3.2.3 Filtering

To filter the noisy fNIR signal generally a low pass filter based on FIR hamming window method is applied. The order of FIR filter should be considered as 20 for 2Hz fNIR signal. The cut-off frequency should be taken 0.1 Hz because meaningful information remains usually inside the band [3]. An FIR filter of order M with the input sequences $x[n]$ and output sequences $y[n]$ is described as [4],

$$\begin{aligned} y[n] &= b_0x[n] + b_1x[n-1] + b_2x[n-2] + \dots + b_{M-1}x[n-M+1] \\ &= \sum_{k=0}^{M-1} b_kx[n-k] \end{aligned} \quad (3.5)$$

In (3.5), b_k denotes filter coefficient or weight. We can express the output sequences as the convolution form of the unit sample response of $h[n]$ as,

$$y[n] = \sum_{k=0}^{M-1} h[k]x[n-k] \quad (3.6)$$

Here, $b_k = h[k]$ and $k = 0, 1, 2, 3, \dots, M-1$. In this work, we are interested to design window based linear phase FIR filter. For this method, we have to begin with the desired frequency response specification $H_d(\omega)$ as well as we also find out the corresponding unit sample response, $h_d[n]$. Frequency response, $H_d(\omega)$ and unit sample response, $h_d[n]$ are related to each other by Fourier transform as,

$$H_d(\omega) = \sum_{n=0}^{\infty} h_d[n]e^{-j\omega n} \quad \text{where, } h_d[n] = \frac{1}{2\pi} \int_{-\pi}^{\pi} H_d(\omega)e^{j\omega n} d\omega \quad (3.7)$$

Thus, with our desired frequency response, $H_d(\omega)$, we are able to determine the unit sample response $h_d[n]$ by estimating the integral in (3.7). Here, it is a fact that the unit sample response $h_d[n]$ is infinite in duration and it is necessary to truncate at some point. If the FIR filter designed for the length of M , it must be truncated at $n=M-1$. Truncation of $h_d[n]$ to a length $M-1$ is equivalent to multiplying $h_d[n]$ by a window, $w[n]$ of length M . There are a number of window functions named by Rectangular, Hamming, Hanning, Blackman, Kaiser, Lanczos, Tukey, Barlett, etc.

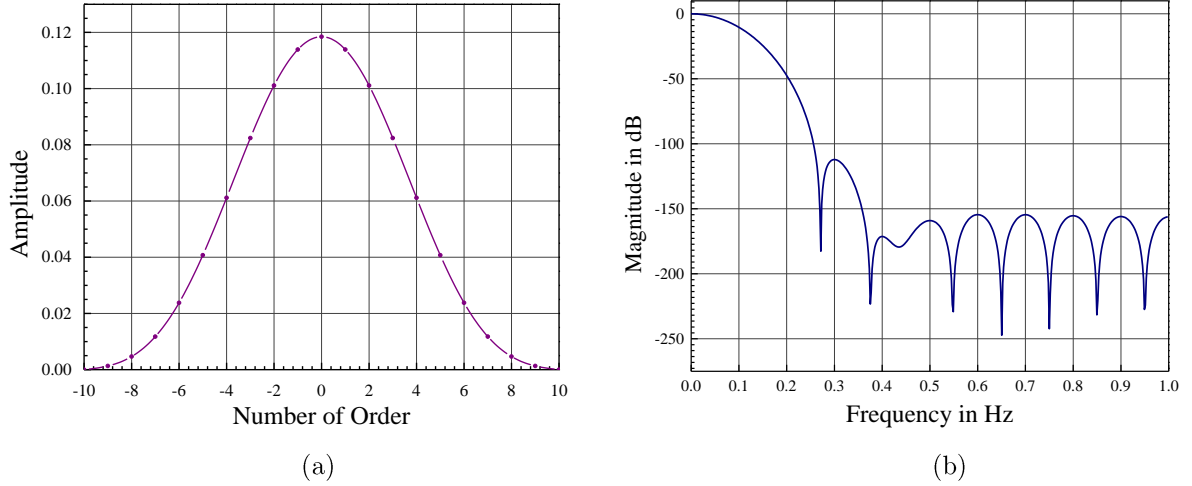


Figure 3.3: The characteristics of Hamming window in the time domain (a) and frequency domain (b) for 20 order low pass linear phase FIR filter.

By default, the Hamming window is considered to filter the fNIR signals in this work. The Hamming window is defined by the following equation [4].

$$w[n] = \begin{cases} 0.54 - 0.46 \cos \frac{2\pi n}{M-1}, & n = 0, 1, 2, \dots, M-1 \\ 0, & \text{otherwise} \end{cases} \quad (3.8)$$

The relation given in (3.8) represents the time domain characteristics of the Hamming window to be applied in low pass FIR filtering. The time domain and frequency domain characteristics of 20 order low pass Hamming window are shown in **Figure 3.3**. According to the relationship explained by (3.8), the unit sample response of our desired filter will be as,

$$h(n) = h_d(n)\omega(n) \quad (3.9)$$

A number of research works [5-8], used SG filter to remove the physiological noises from the fNIR signals. The basic technique of SG filter is to fit a data vector with the different polynomial order. A center data point with a set of the data point at the behind and front create a frame and then the data set is fitted with considering the polynomial order. The smoothed points are computed and the central point is replaced by the new one and the frame is shifted to consider the next center point. More succinctly, SG filter is a least square error polynomial fitting procedure that is deliberated as piece-wise fitting of a polynomial function to the signal. This time domain filter has some benefits over the FIR filter. The Euclidian distance of FIR

filter between the signal variations related to the original and noisy signals is higher than that of SG filter. The higher Euclidian distance for the FIR filter is due to its shifting effect (group delay). This shifting effect may damage the structure of the original signal pattern in the time-frequency plane. Since SG filter has the intrinsic ability to remove the high-frequency noise from the signals, we are concerned about the applicability of SG filter with optimal conditions to remove physiological noises (high-frequency noise) from the fNIR signals.

In the procedures of SG filtering technique, the fitting is done by the least square error estimation. Suppose, we have a sequence of samples $x[n]$ of the fNIR signal. We are interested to perform a smoothing or filtering procedure by SG filter. SG filter is designed based on local least-squares polynomial approximation. Suppose, the moment of the group of $2M+1$ samples and their center is considered at $n=0$. In case of any polynomial of n , the coefficients can be represented as,

$$f[n] = \sum_{j=0}^n n^j a_j \quad (3.10)$$

According to the least-square error, we are interested to minimize the error between raw actual value and estimated value. Therefore, the consequent error function can be predicted by the following consideration given in (3.11).

$$\begin{aligned} e &= \sum_{n=-M}^M (f[n] - x[n])^2 \\ &= \sum_{n=-M}^M \left(\sum_{j=0}^n n^j a_j - x[n] \right)^2 \end{aligned} \quad (3.11)$$

If we consider any other group of $2M+1$ input samples, the analysis will be the same. Here, M is the half width of the total sample length of the group. Therefore, the actual frame size is $2M+1$. According to the original paper by Savitzky and Golay [9], the set of $2M+1$ input samples within the approximation interval is effectively combined by a fixed set of weighting coefficients that can be computed once for given polynomial order N and approximation interval of length $2M+1$ [10]. Eventually, the output samples can be computed by a discrete convolution of the form,

$$y[n] = \sum_{m=-M}^M h[m]x[n-m] \quad \text{or} \quad y[n] = \sum_{m=n-M}^{n+M} h[n-m]x[m] \quad (3.12)$$

The impulse response could be used to compute the output samples instead of using the polynomial fit process at each sample with its 0th polynomial coefficient. The mathematical explanation is described in detailed nicely in [10]. In addition to that, the coefficients of different frame and order are given in [9]. Therefore, with coefficients of different orders and frame sizes of SG, the signal is filtered.

In addition to that, by SG filter with appropriate order and frame length same filtering effect can be achievable which is shown in our research work [11]. A concluding remarks of this research work has been presented by Table 3.1, where we find the equivalent performance of the FIR filter and SG filter with their specifications. For smoothing the fNIR signals, we can use SG filter because of its special benefit *i.e.*, SG filter is better than FIR filter for removing high frequency contents from fNIR signals. Because, in case of FIR filter, Euclidian distance between original and filtered signal is more than that of the SG filter [12]. Furthermore, employing SG needs no delay correction as FIR filter. The results of FIR filter and corresponding SG filter on the raw FIR filter has been given in **Figure 3.4**. From this result we get that the output by the two methods are almost similar after being filtered.

Table 3.1: Recommended optimal conditions of SG filter for removing physiological noises from fNIR signal [11] with compared to the conditions of FIR filter.

Serial Number	FIR Filter Specification		Optimal Conditions of SG Filter	Level of Correlation, r
	Order Number	Cut-off Frequency (Hz)	(Order, Frame Size)	
1	20	0.1	(3,21)	0.9916
2	30	0.1	(1,11)	0.9912
3	40	0.1	(1,13)	0.9908
4	20	0.14	(1,7)	0.9961
5	30	0.14	(3,19)	0.9942
6	40	0.14	(4,27)	0.9921
7	20	0.03-0.1	(1,9)	0.9937
8	30	0.03-0.1	(3,19)	0.9910
9	40	0.03-0.1	(4, 31)	0.9790

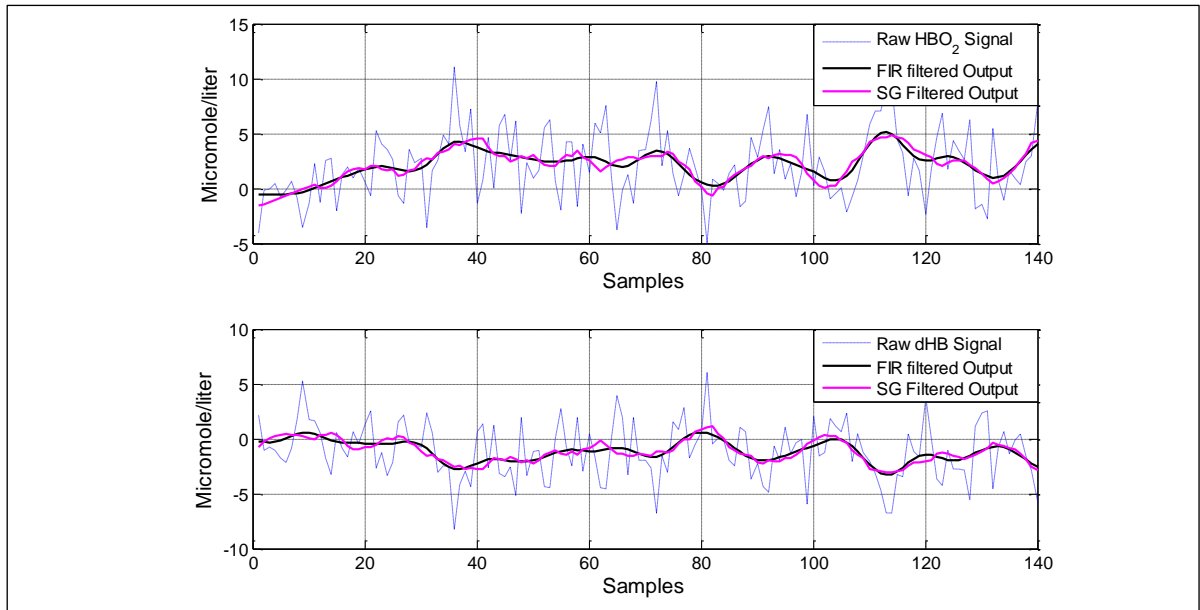


Figure 3.4: Filtering performance comparison between SG and FIR filter for fNIR signal for both HbO₂ and dHb signals [11].

3.1.4 Baseline Correction

For each trial of the fNIR data had been corrected by subtracting baseline from the original signal. Baseline was calculated from the average of the first five seconds of the task. This consideration helps to represent the activation in such a way that the starting of the task, the hemodynamic activation remains at the baseline and that is zero or the value closed to zero. Baseline is calculated from the average of the first 2 seconds of the task. This consideration [13, 14] ensures the initial signal points regarding each trial to remain at the zero level or the value closed to zero. After baseline correction, the signals can be considered for the further analysis like statistical inference, feature extraction, classification, etc.

3.3 EEG Signal Preprocessing

For EEG signal preprocessing, the most important action is to filter the EEG signal. EEG signals are filtered in several steps because EEG signal is very noise sensitive and complex in nature. A number of noises are incorporated in EEG signal like power line noise, eye blink, EOG etc. those are already discussed in previous chapter. To filter the EEG signal several steps have been considered in this work those are discussed gradually. In addition, the most significant features from EEG signal was extracted by relative PSD calculation from alpha and beta band of EEG signal.

3.3.1 Notch Filter

In the field of signal processing, a notch filter is a special type of band-stop filter. A band-stop filter permits to pass all frequencies except a specific range of frequency band. Therefore, it acts as the opposite characteristics of a band-pass filter. The band-stop filter rejects a very narrow frequency band with very high quality factor is often called a notch filter. The characteristic of a notch filter is given in **Figure 3.5**. For a 256 Hz sampling rate EEG signal, a notch filter has been designed to remove 50 Hz noise. From the magnitude response of the notch filter in **Figure 3.5**, it has been found that the 60 Hz frequency will be stopped by the filter.

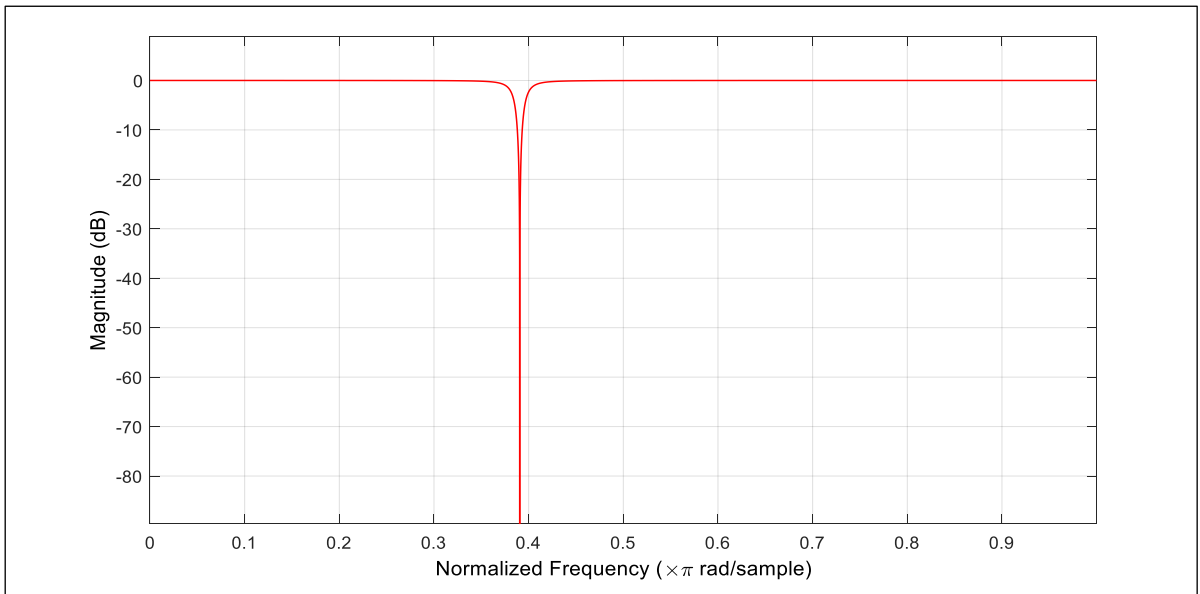


Figure 3.5: Magnitude response of the 50 Hz notch filter with 256 Hz sampling rate. The frequency has been normalized here and the magnitude has been presented in dB.

3.2.2 Elliptic Filter

The elliptic filter provides sharp cut off frequency and less values of filter order than the other IIR filters like Chebyshev, Butterworth, Bessel, etc. [15]. It is also known as Zolotarev or Cauer filters. This filter shows equi-ripple characteristics both in the pass-band and stop-band. Since elliptic filter achieves the minimum order value for a given specification, it is considered as optimal filter [16]. Eventually, it is slightly complex to design and it often needs several complex algorithms to design and implement it. The response of an elliptical filter in the magnitude-square aspect in frequency domain can be presented as [16],

$$|H(i\omega)| = \frac{1}{1 + \delta^2 J_N^2\left(\frac{\omega}{\omega_c}\right)} \quad (3.13)$$

Here, ω and ω_c are for the frequency and cut off frequency, respectively. In addition, the pass band ripples are presented by δ . Here, $J_N(\bullet)$ is the N^{th} order Jacobian elliptical function. Though analysis to solve the relation (3.13) is difficult, the order calculation procedure is compact at all [17-19] and which is given by,

$$N = \frac{\psi(k) \psi(\sqrt{1-k_1^2})}{\psi(k_1) \psi(\sqrt{1-k^2})} \quad (3.14)$$

In (3.14), $k = \frac{\omega_p}{\omega_s}$ and $k_1 = \frac{\delta}{\sqrt{A^2 - 1}}$ where, ω_s is stop band frequency and A is stop

band attenuation. Besides, $\psi(k) = \int_0^\pi \frac{d\theta}{\sqrt{1 - k^2 \sin^2 \theta}}$ which is a complete elliptical

integral. This elliptical filter is used to filter the signal according to the interest of the frequency band of the EEG signal. With arbitrary pass band and stop band ripple, the frequency response of an elliptical filter having 5th order has been given in

Figure 3.6.

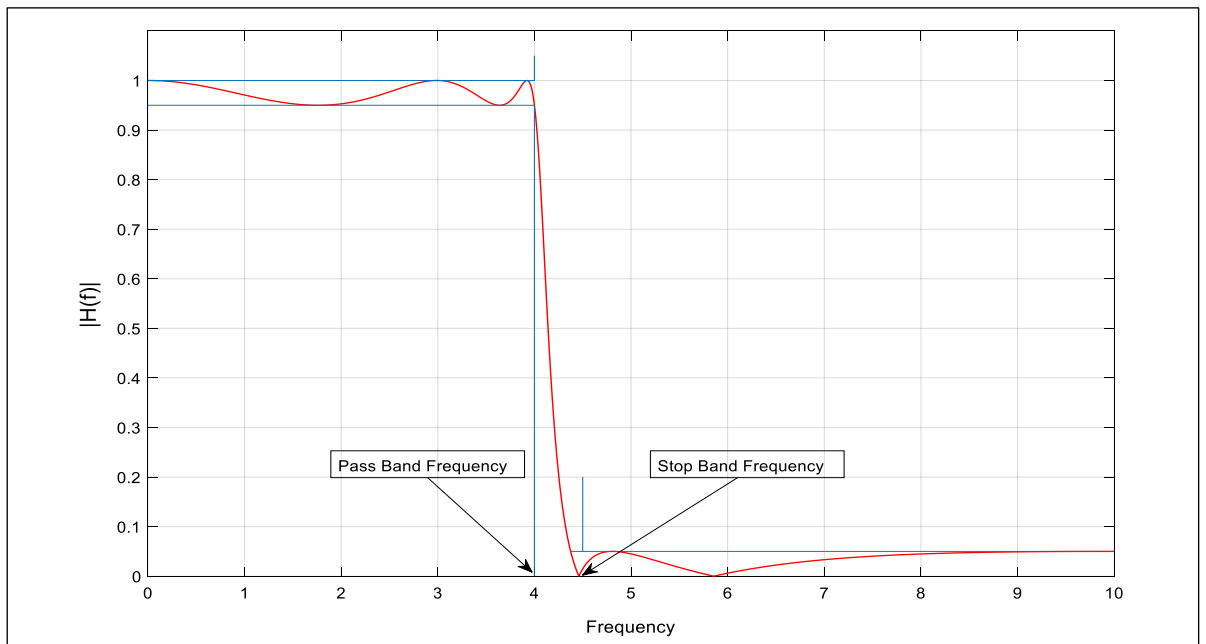


Figure 3.6: Frequency response of an elliptical filter of 5th order with arbitrary pass band and stop band ripple.

3.2.3 Eye Blink Removal

Eye blink removal is an important step of EEG signal filtering. Eye blink removal is a complex process. Various proposals have been proposed to remove eye blink from EEG signal. The most significant eye blink removal technique from the EEG signal is wavelet based ICA. We have applied this method to remove the eye blink from the EEG signal. To do this, we have used the enhanced automatic wavelet independent component analysis (EAWICA) toolbox [20] on or EEG data. The detail about the EAWICA has been added in Appendix.

3.2.4 Wavelet Packet Transformation based Feature Extraction

The EEG signals are complex in nature and its properties belong both time and frequency domain. Therefore wavelet analysis is quite logical for the EEG signal feature extraction. In this work the EEG signals are separately utilized to extract feature using wavelet packet transformation (WPT) so that single modality EEG-based classification performance of multiclass problem can be measured. The WPT is a concept that is different from conventional wavelet transformation (WT). WPT decomposes both the approximate coefficients and the detailed coefficients. The extracted coefficients through WPT up to a defined level could be considered as the features of the EEG signals, because the value of the coefficients depends on the time and frequency domain characteristics of the EEG signal. This concept has been utilized in this work for feature extraction from the EEG signal for classification through conventional classifiers like artificial neural network, support vector machine, k-nearest neighbor, linear discriminant analysis, etc.

The WPT may be considered as a subspace tree. We can present the original signal as $\Pi_{0,0}$ which reflects the root mood of the tree in the original signal space. Generally the notation j and k in $\Pi_{j,k}$ denotes the scale and sub-band space. The WPT decomposes an original signal $\Pi_{j,k}$ into two different subspaces: an approximation space $\Pi_{j,k} \rightarrow \Pi_{j+1,2k}$ and a detailed space, $\Pi_{j,k} \rightarrow \Pi_{j+1,2k+1}$. This space decomposition utilizes the concept of dividing the orthogonal basis function $\{\phi_j(t - 2^j k)\}_{k \in \mathbb{Z}}$ of the original signal space into two new orthogonal bases, i)

$\{\phi_{j+1}(t - 2^{j+1}k)\}_{k \in \mathbb{Z}}$ of approximate space $\Pi_{j+1,2k}$ and *ii*) $\{\psi_{j+1}(t - 2^{j+1}k)\}_{k \in \mathbb{Z}}$ of detailed space $\Pi_{j+1,2k+1}$. Here, $\phi_{j,k}(t)$ and $\psi_{j,k}(t)$ represents the scaling and wavelet functions, respectively. These functions are equated as [21, 22],

$$\phi_{j,k}(t) = \frac{1}{\sqrt{|2^j|}} \phi\left(\frac{t - 2^j k}{2^j}\right) \quad (3.15)$$

$$\psi_{j,k}(t) = \frac{1}{\sqrt{|2^j|}} \psi\left(\frac{t - 2^j k}{2^j}\right) \quad (3.16)$$

Here 2^j is the scaling parameter that measures the scaling or compression degree of the original signal. In addition, $2^j k$ is the location parameter or translation parameter that indicates the time location of the wavelet. The aforesaid process can be repeated J times, where J must be less than $\log_2 N$. Here, N is the total number of samples in the original signal. This process of WPT $J \times N$ finds coefficients. Therefore, at any level of transformation j [$j = 1, 2, \dots, J$], the tree has $N/(2^j)$ coefficient blocks. This iterative process in a WPT can be treated as a tree-like structure, where the tree nodes represent the subspaces of different frequency localization characteristics. The corresponding decomposition procedure can be presented as **Figure 3.7** [22, 23].

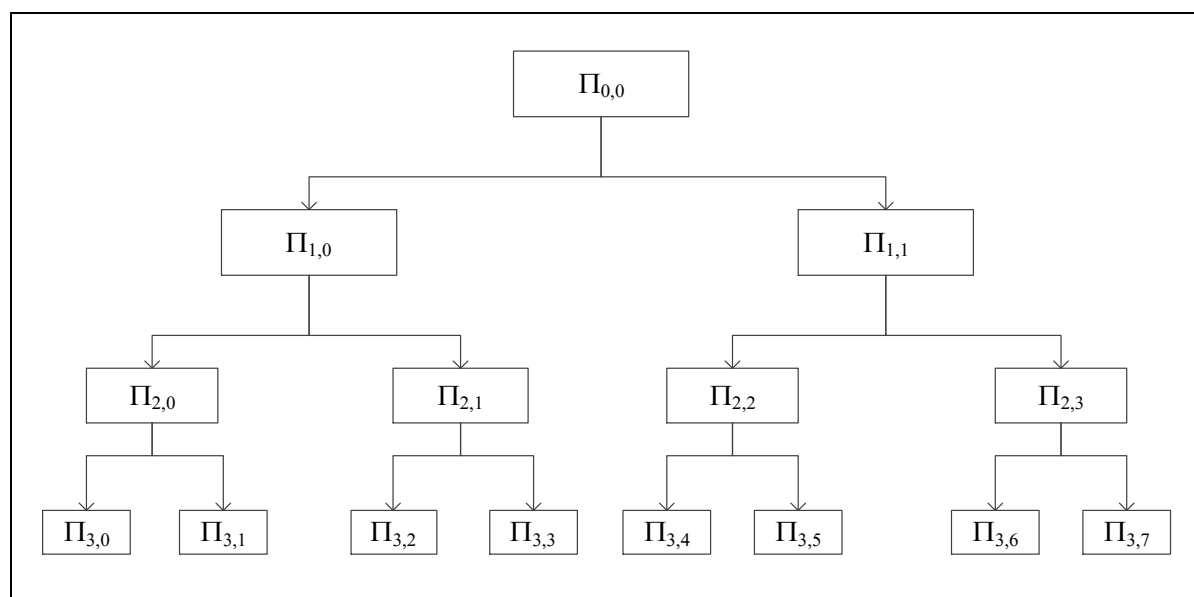


Figure 3.7: Graphical representation of wavelet packets decomposition method that decomposes $\Pi_{0,0}$ into tree-structured subspaces

3.2.5 Power Spectral Density Calculation

For random signals, it is only possible to propose probabilistic reports about the dissimilarity of the signals based on the probability of occurrence. To assess EEG signal PSD as a frequency domain feature provides crucial information about the distribution of power. Power spectrum or spectral analysis of the signal $x(t)$ is the distribution of power over its frequency components. In this research work, beta PSD is calculated from each to point out the variation of PSD ($\mu\text{V}^2/\text{Hz}$) according to the different tasks using the FFT algorithm. A random signal usually contains finite average power which is characterized as average power spectral density. The average power, P of the signal $x(t)$ during the total length of the signal period is defined as,

$$P = \lim_{T \rightarrow \infty} \int_{-T}^T |x(t)|^2 dt \quad (3.17)$$

The mathematical relation given in (3.17) is for a continuous time signal. For discrete time signal, the notation $x(t)$ becomes $x(n)$ where $t=nT$ (T is sampling time interval and n is the sequence number). Therefore, for analyzing the frequency content of the discrete time signal, PSD is the Fourier transform of the auto-correlation function which can be represented as [24],

$$P_x(e^{j\omega}) = \sum_{k=-\infty}^{\infty} r_x(k) e^{-jk\omega} \quad (3.18)$$

In (3.18), $r_x(k)$ means autocorrelation for the periodic signal. But for the ergodic process,

$$r_x(k) = \lim_{N \rightarrow \infty} \left\{ \frac{1}{2N+1} \sum_{n=-N}^N x(n+k) \otimes x(n) \right\} \quad (3.19)$$

Where ‘ \otimes ’ denotes convolution of two signals [24, 25].

PSD calculation adopting windowing method is very important for nonparametric such as EEG signal. For nonparametric power spectral density estimation, the Welch method is most renowned method than the other methods (Periodogram and Bartlett). Let’s assume that the successive sequences are offset by D points and that each sequence is L point long, then the i^{th} sequence is,

$$x_i(n) = x(n + iD) \quad (3.20)$$

Thus L-D points are overlapped. If entire U data points are covered by K sequences then,

$$N = L + D(K - 1) \quad (3.21)$$

According to the previous conditions, Welch's method is written as,

$$\hat{P}_w(e^{j\omega}) = \frac{1}{KLU} \left| \sum_{i=0}^{K-1} \sum_{n=0}^{L-1} w(n)x(n + iD)e^{-jn\omega} \right|^2 \quad (3.22)$$

Therefore, the expected value by Welch's estimation [26] is,

$$E\{\hat{P}_w(e^{j\omega})\} = E\{\hat{P}_M(e^{j\omega})\} = \frac{1}{2\pi LU} P_x(e^{j\omega}) * |W(e^{j\omega})|^2 \quad (3.23)$$

The absolute power (AP) of a frequency band is calculated by the summation of all the power values in its frequency range. Relative power (RP) for each band was originated through articulating AP in apiece frequency band as the percent of the AP over the two frequency bands. If any band relates to specific neural activities, its relative power also increases with respect to resting condition. Therefore, relative power plays important roles in finding the specific electrical activities from the EEG signal. In this research work, AP is calculated from 1 to 100 Hz (50 Hz already filtered by notch filter). Due to the aforementioned consequences, the RP is calculated as [5, 26],

$$RP(\varphi_1, \varphi_2) = \frac{P(\varphi_1, \varphi_2)}{P(1, 100)} \times 100\% \quad (3.24)$$

Here, P indicates the power, RP represents the Relative Power, and φ_1 & φ_2 is the low and high frequency, respectively.

3.4 Combining fNIR and EEG Signal to Produce Neuroimages

A two dimensional data arrangement of the combined fNIR-EEG data has been proposed in this work. Since the sampling rate of fNIR (2Hz) and EEG (256Hz) are not similar, the data of EEG signal has been transformed into frequency domain to represent it into the similar sampling rate of the fNIR signal. According to this proposal, fNIR signal length was 30 sec (10 sec stimuli + 20 sec activation). There are 16 channels of both HbO₂ and dHb data. The 16 channel data of HbO₂ and dHb are arranged as the procedure shown in **Figure 3.8**.

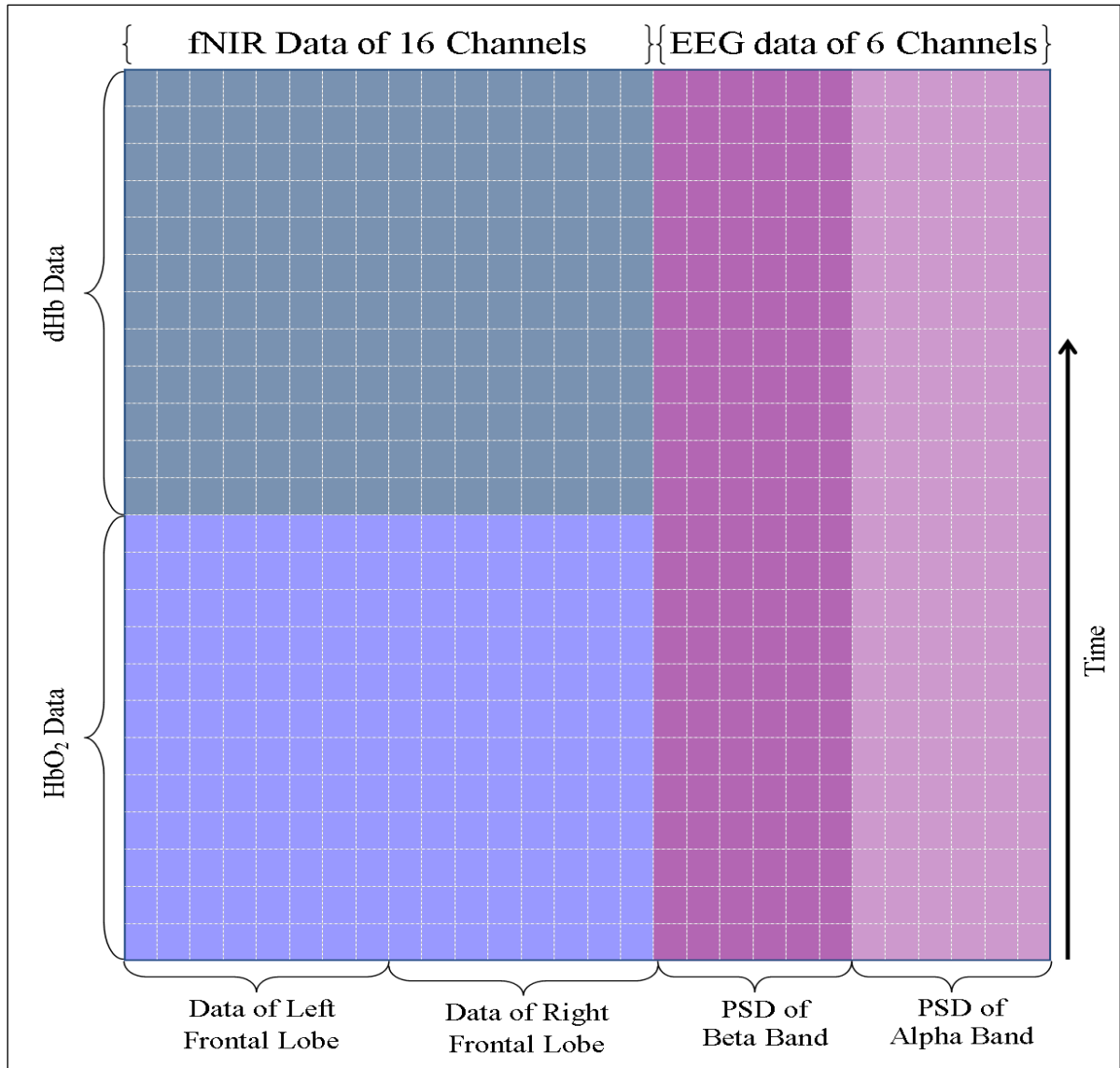


Figure 3.8: Combining the fNIR and EEG data to prepare the spatiotemporal neuroimages for classification by CNN.

Now, the data samples per channel become 120. Since the EEG data has been taken as the same time frame of the EEG signal during the concurrent fNIR-EEG recording. As, a result a suitable window length can be taken with 50% overlapping mode to calculate the PSD of the alpha and beta band of the EEG signal to get the exact 120 samples from per channels. In case of the EEG signal, only frontal and central channels are taken into account. Therefore, in total 6 channels (F3, Fz, F4, C3, Cz, and C4) are considered for the PSD calculation. We exclude the parietal (P3, Pz, and P4) lobe EEG data from the acquired 9 channels. The PSD data of alpha and beta band of the EEG signal are placed at the side of the fNIR data as given in **Figure 3.8**. These data are used to make the spatiotemporal neuroimages for using

in CNN classifier. Furthermore, before applying the combined fNIR-EEG data to make the required neuroimages the HbO₂, dHb, alpha PSD, and beta PSD are normalized separately using the following equation:

$$\pi' = \frac{\pi - \pi_{\min}}{\pi_{\max} - \pi_{\min}} \quad (3.25)$$

Here, π' are the feature values those are rescaled between the range 0 and 1. On the other hand, $\pi' \in \mathbb{R}^n$ are the actual values of the features. The maximum and minimum value of the features are presented as π_{\max} and π_{\min} , respectively.

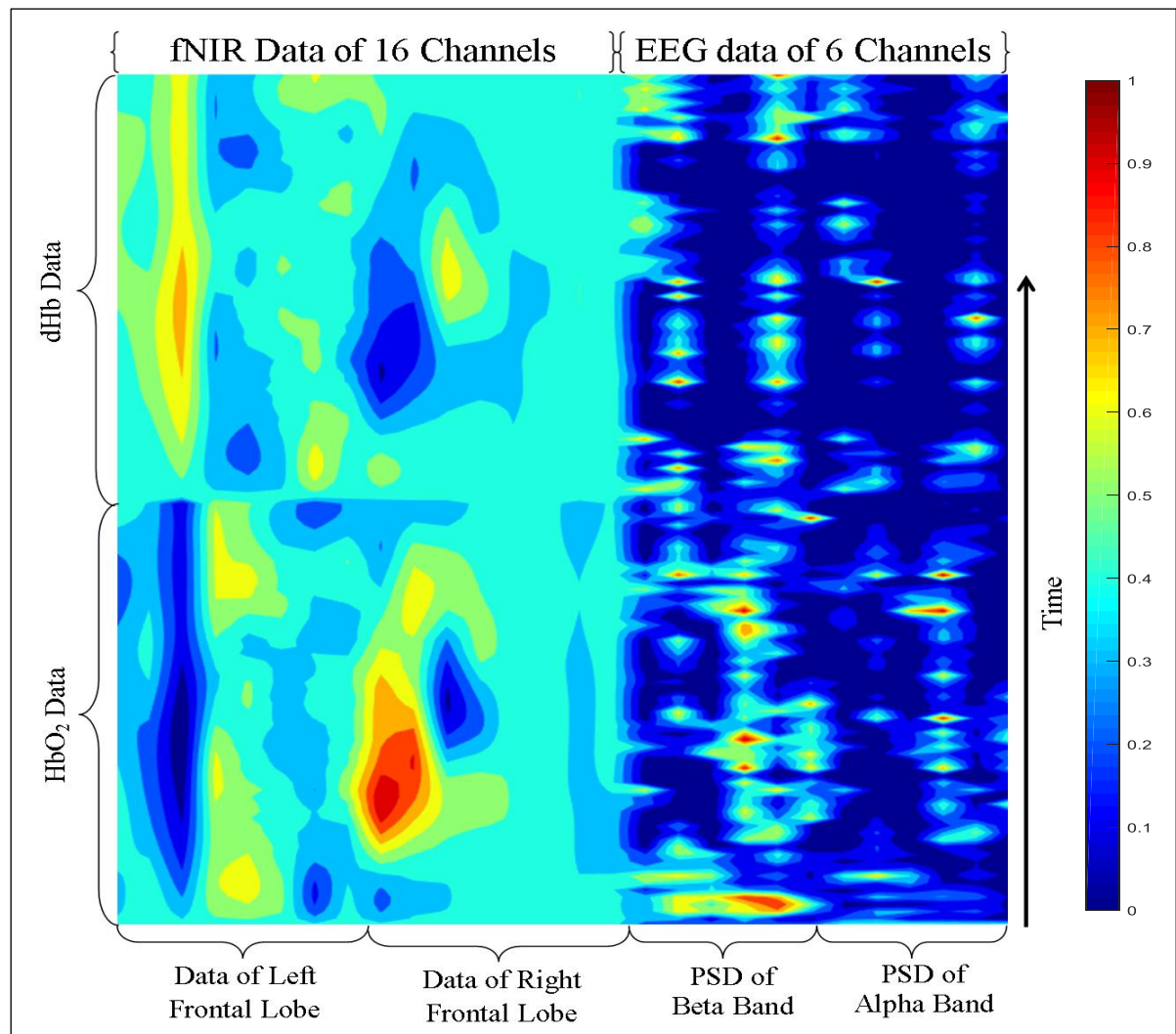


Figure 3.9: Prepared spatiotemporal neuroimage combining the fNIR and EEG data by the proposed method.

According to our novel proposal of the fNIR-EEG combined spatiotemporal EEG data, a typical fNIR and EEG data of a particular stimulus has been considered to make the neuro-image and the found image is given in **Figure 3.9**. The colorbar is given in the right side of the **Figure 3.9**. Therefore, using the proposed method the combined fNIR-EEG data can be transformed into images those can be applied to the input of the CNN. The Matlab code of the image generation has been given in Appendix. This is a novel approach of presenting the combined fNIR-EEG time series data because so far our knowledge, no research work has not proposed such style of fNIR and EEG data combination process.

3.5 Classification

For classification the voluntary and imagery tasks from the fNIR signal, conventional feature extraction and classification technique can be applied. Moreover, in this work, we have proposed a statistical way to classify the fNIR signal utilizing the proposed activation model of the HbO_2 and dHb concentration. Although the proposed classification method is not too powerful to the conventional classifiers, it is very simple to implement and significant in the results. Here, both the proposed method and the conventional classification method have been applied to compare the results. Additionally, to classify the combined information of EEG and fNIR, CNN has been used. The fundamentals of the CNN have also been explained here.

3.5.1 Proposed Classification Method

Suppose that an fNIR signal is to test whether it is the signal of LH, RH, iLH, iRH, iLF, or iRF stimuli. The testing signal can be presented as, $S_k = [S_{LL} \ S_{LM} \ S_{RM} \ S_{RL}]$ that contains 4 columns of data of 4 different ROI's of the prefrontal cortex and every column of signal contain N number of data sample. The value of $k = 1, 2, 3,$ and 4 indicates the positions (LL, LM, RM, and RL, respectively). Again, we have six model equations of six different stimuli (voluntary and imagery). The temporal activation model can be represented as, M_τ^c where the notation $\tau = 1, 2, 3, 4, 5,$ and 6 (LH, RH, iLH, iRH, iLF, and iRF, respectively) represents the index of the stimuli and $c = (1, 2) = (HbO_2, dHb)$ represents the concentration information. Therefore, M_3^2 means the activation model of iLH in HBR concentration. To measure the maximum

similarity index of the testing signal S_k with the models M_τ^c , the following error has been calculated.

$$e_{\tau,k}^c = \frac{1}{N} \sum_{i=1, k=1}^{i=N, k=4} (S_k(i) - M_\tau^c)^2 \quad (3.26)$$

Therefore, testing with the six different models we get two final error matrices, $e_{\tau,k}^1$ and $e_{\tau,k}^2$ for the HbO₂ and dHb, respectively where, $e_{\tau,k}^c = [e_{1,k}^c \ e_{2,k}^c \ e_{3,k}^c \ e_{4,k}^c \ e_{5,k}^c \ e_{6,k}^c]$. Moreover, the size of $e_{\tau,k}^c$ is 1×24 . According to the proposed methodology, the maximum similarity pattern will show the minimum error. Therefore, the minimum value in the elements of the error matrix $e_{\tau,k}^c$ indicates the signal class. Therefore, the index of the minimum valued element, I_{dx} of the error matrix $e_{\tau,k}^c$ can be found by applying the following argument,

$$I_{dx} = index(\min(e_{\tau,k}^c) = e_{\tau,k}^c) \quad (3.27)$$

If the model activation patterns are loaded in the algorithm of data testing in the proposed sequences, the proposed model suggests that the minimum valued index of a specific task will follow a fixed pattern. The aforementioned methodology has been briefly presented with a flow diagram in **Figure 3.10**. The index for the value of τ will be 3, 6, 11, 14, 20, and 21 for all six classes, respectively. This same design can be regarded as two to six classes. For that proposition, the value of τ is to set according to the number of the classes. In this work, classifications of the two, four, and six class approaches were conducted.

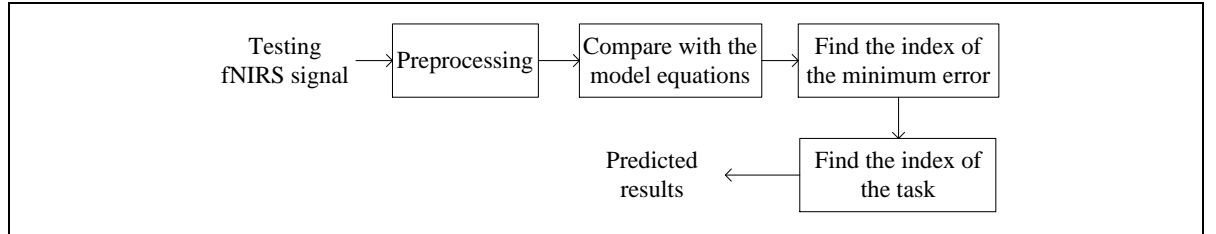
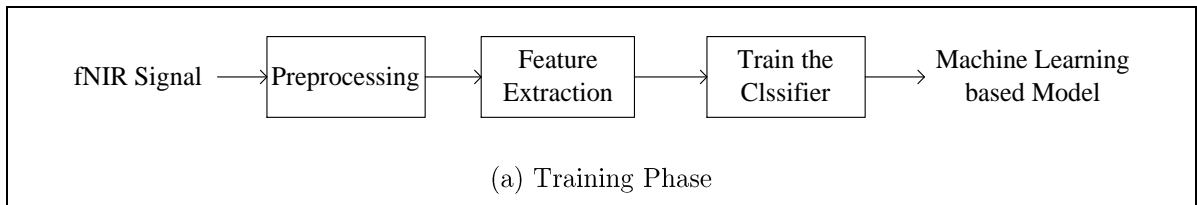


Figure 3.10: Classification mechanism of the proposed method utilizing the proposed activation models.

3.5.2 Conventional Shallow Network-based Classification Methods

In the conventional classification approaches, feature extraction is a primary step to classify the data set. Although there are many techniques to extract features from the signals like ICA, PCA, CSP etc., these methods are often used in the feature extraction of the complex signals like EEG, MEG, EOG, etc. for its time and frequency domain properties. Since fNIR signals exhibit simple time-domain characteristics, most of the classification techniques need only time domain features like mean, slope, skewness, median, maximum, minimum, etc. [27-29] to classify the signals. For classification purpose, the signals are generally separated into two parts: *i*) for training purpose and *ii*) for testing purpose. For a 5-fold cross-validation technique, 4/5 portion of the data is used to train the classifier to make a model and the rest of the data are used to predict the performance of the model. The training and testing files are separated with 5-different combinations from the original data set. Then the overall classification accuracy is found by averaging the results of the 5 different classification accuracies. This training and the testing procedures are shown in **Figure 3.11** where there are two phases: training phase **Figure 3.11(a)** and testing phase **Figure 3.11(b)**.

Although “*No Free Lunch*” theorem claims that no classification mechanism is entirely superior to the other [30], the most commonly used classifiers in fNIR based event classification was utilized in this work. The review work [31] found that four classifiers are repeatedly used by the researchers of fNIR based BCI and those are linear discriminant analysis (LDA), support vector machine (SVM), k-nearest neighbor (kNN), and artificial neural network (ANN). These four classifiers were used to classify the events. Though the detail mathematical explanations of these machine learning based algorithms are out of the scope of this research work, a short note on the working method of each individual classification method is given here.



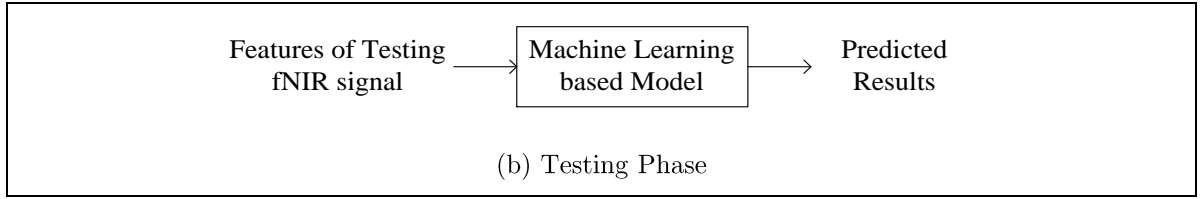


Figure 3.11: The overall mechanism of the conventional machine learning based classifiers.

LDA: LDA is the widely used classification technique in fNIR signal classification due to its low computational complexity and high speed [32, 33]. To classify or separate the two or more that two classes data, LDA employs discriminant hyperplane(s). Since the main mechanism of the LDA is dimension reduction, it chooses the hyperplane(s) by minimizing the ratio of within-class variance and maximizing the ratio of between-class variance (*i.e.*, Fisher’s criterion [33]) assuming the data of the classes are Gaussian distributed with equal covariance. Based on Fisher’s criterion, the effective projection matrix P is calculated in LDA as [29, 33],

$$f(P) = \frac{\det(P^T \tau_b P)}{\det(P^T \tau_w P)} \quad (3.28)$$

In (3.28), τ_b and τ_w stand for the between-class scatter matrix and the within-class scatter matrix, respectively. Besides, $\det(\bullet)$ represents the determinant of the matrix.

We can define τ_b and τ_w by the following relations [31, 34]:

$$\tau_b = \sum_{i=1}^m \nu_i (\mu_i - \bar{X})(\mu_i - \bar{X})^T \quad (3.29)$$

$$\tau_w = \sum_{i=1}^m \sum_{x_k \in \text{class } i} (x - \mu_i)(x - \mu_i)^T \quad (3.30)$$

Here, x ’s are the samples of the feature vector of a class, μ_i and \bar{X} represent the sample mean of class i and the grand mean of all the samples of m classes, respectively. The number of total samples is represented by ν where, ν_i represents the number of samples in class, i . The solutions of (3.29) and (3.30) can be found considering them as an eigenvalue problem that leads to finding the optimum values of the projection matrix, P . In Matlab 2018a, `fitlda()` was used to construct the LDA based predictive model which was further utilized with 5-fold cross-validation to check the classification performance.

SVM: SVM is an extensively employed classifier for its high prediction accuracy in high-dimensional features [35-37]. SVM can be used as a linear or nonlinear method. The main mechanism followed by SVM is to generate the hyper-planes that maximize the margin among the classes. The nearest points of the hyper-planes are called support vectors. The discriminating hyper-plane in a 2D feature space can be formularized as,

$$\varphi(x) = d \cdot x + c_1 \quad (3.31)$$

In (3.31), $x, d \in \mathfrak{R}^2$ and $c \in \mathfrak{R}^1$. To find the optimal results of d^* maximizes the distance between the hyper-plane and the support vectors. This maximization procedure is obtained by minimizing the following cost function (3.32) cogitating the restrictions given in (3.33) [37, 38].

$$\varphi(d, \xi) = \frac{1}{2} \|d\|^2 + \Gamma \cdot \sum_{z=1}^Z \xi_n \quad (3.32)$$

$$\begin{aligned} (x_n \cdot d + c_1) &\geq 1 - \xi_n & \text{for } y_n = +1 \\ (x_n \cdot d + c_1) &\geq -1 + \xi_n & \text{for } y_n = -1 \\ \xi_n &\geq 0 & \forall_n \end{aligned} \quad (3.33)$$

In (3.32) $d^T d = \|d\|^2$ and Γ is a regularization parameter that can be chosen by the users based on the penalty factor of classification errors. Besides, ξ_n represents the measurement of error during the training period, Z represents the number of samples those are misclassified, and y_n represent the class label for the n^{th} sample (for a binary classification problem, it is +1 and -1). In this work, we used the Matlab toolbox as one versus all approach of SVM. The SVM structure was defined with polynomial kernel function with default order value 3.

kNN: Although kNN is known as a lazy nonparametric classifier, till now it is chosen by the researchers of various fields because of its simplicity. This method does not need any explicit training phase to generalize the training feature vectors. Therefore, the training phase is precisely fast. During the training period, kNN actually keeps all the training features with their labels for the testing phase. The kNN algorithm finds the points from the training data those are nearest to be considered for the selection of the class of a new testing observation. To take a

decision on the nearest points, there are several distance calculating formulas like Euclidean, Minkowski, Cityblock, Manhattan, Mahalanobis, Cosine, Chebychev, etc. Therefore, we find there key steps of the kNN approach: *i*) a set of training feature vectors with label information *ii*) a distance metric to measure the distance between objects, and *iii*) the number of the nearest neighbors, k . Suppose, we have a training set, $(T(\phi, y) \in T)$ that contains the feature vectors, ϕ with their labels, y and a test object $t = (\phi', y')$ where ϕ' is the feature vectors of the test object and y' is its class. Now, the kNN algorithm measures the distance between $(\phi', y') \in t$ and the training objects $(\phi, y) \in T$ to estimate the nearest neighbor list, $(\phi_i, y_i) \in T_t$. From the list of the nearest neighbors, the class of the object will be decided by the following majority voting condition [39],

$$\text{Majority Voting : } y' = \arg \max_v \sum_{(\phi_i, y_i)} I(v = y_i) \quad (3.34)$$

where v is a class label. On the other hand, y_i is the class label for the i^{th} nearest neighbors and $I(*)$ is a function that indicates the value 1 for the true argument and 0 otherwise. In our proposed kNN based predictive model, the distance calculation was performed by the Euclidean method with $k = 3$ for two class and $k = 5$ for four and six class classification.

ANN: ANN is a complex but very efficient classifier. This algorithm was also used in this research work to find the highest classification accuracy of fNIR based BCI system [40]. ANN has a quality to mimic the comportment of the human brain. For the feedforward networks, commonly multilayer perceptrons consist of three type layers: input, output, and hidden layers. The objective of the input layer is to buffer the distribution of the input signals $x_n (n = 1, 2, 3, \dots)$ towards the hidden layer neurons. Each hidden layer neuron adds the input signals (x_n) after weighing the input signals by the strengths W_{jn} from the input layer and calculate the output, Y where Y is a function of their summations [40].

$$Y_j = f \left(\sum_{n=1}^n W_{jn} x_n \right) \quad (3.35)$$

Here j is neuron numbers, ΔW_{jn} is the adjustment weight of a connection between n and j according to their relation, $\Delta W_{jn} = \eta \delta_j x_n$. Here, η is the rate of learning parameter and the factor, δ_j depends on the condition whether j is an input or hidden neuron. The adjustments of the weights are generally estimated by the back-propagation algorithm. Let, V_i be the prediction for j^{th} observation in an ANN system and is a function of the network weights vector $\underline{W} = (W_1, W_2, \dots)$. Therefore, e , the total prediction error will also be a function of W as, $e(W) = \sum [Y_j - V_j(W)]^2$ [40]. For every weight W_i , according to the gradient descent algorithm the updating formula is considered as, $W_{new} = W_{old} + \alpha (\partial e / \partial W)_{W_{old}}$. Here, α is the learning parameter and the value of α lies between 0 and 1. In this work, we used two hidden layers for two class classifications and four hidden layers for the four and six class classification problems. In every case, the classification accuracy was calculated with a 5-fold cross-validation technique.

3.5.3 Convolutional Neural Network (CNN)

Previously, the structures and the applying methodologies of the ANN, kNN, SVM, and LDA classifiers are discussed. These classifiers are known as shallow network. There are some limitations of these shallow networks. With the variations of the features, the classification accuracies of these networks are varied. In addition, for a wide number of classes having the similar properties classification accuracies fall in unacceptable ranges. Therefore, to outtake these pitfalls of shallow neural network, deep neural networks (DNN) are often used. In short, we can say that DNN is a machine learning method that employs the deep neural network. A DNN contains the multi-layer neural network having two or more hidden layers. The concept of a DNN can be expressed briefly by **Figure 3.12**.

Although DNN works much better than that of the shallow neural network (SNN), it actually does not need any critical technologies to imply. The innovation of DNN is actually a result of a number of small technical improvements [38]. In case of neural network with deeper layers provide poor performance because the network cannot be properly trained. During the training period, three major difficulties: *i*) Vanishing Gradient, *ii*) Overfitting, and *iii*) Computational Load are experienced by the

backpropagation algorithm which makes it unable to attain the expected outcomes [41].

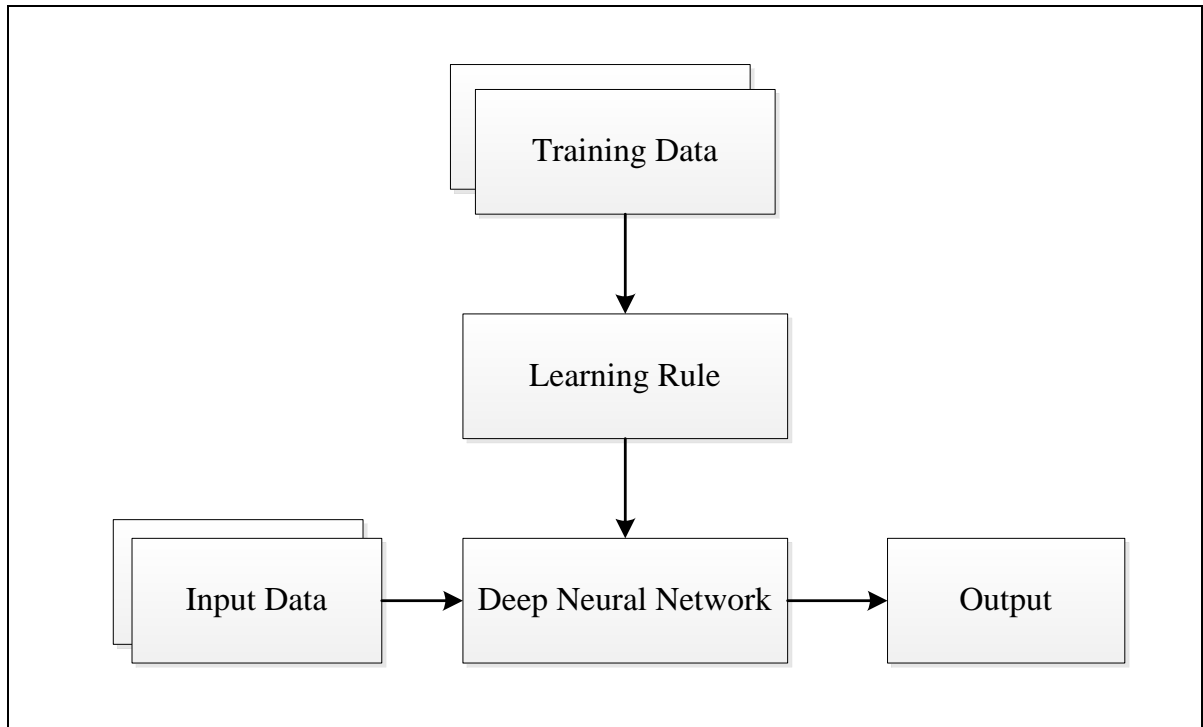


Figure 3.12: The block diagram illustrates the basic concept of deep learning approach with its relationship in the field of machine learning.

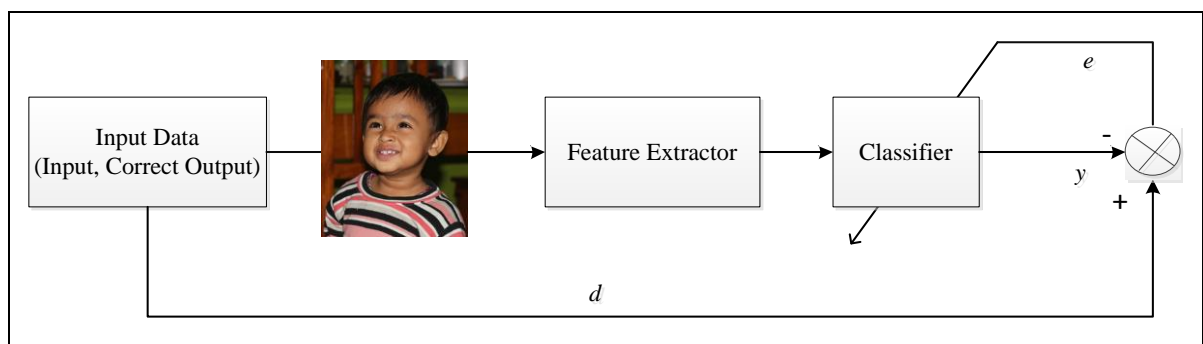


Figure 3.13: Feature extraction as a separate function to be used for the classifier. The feature extraction step was independent to the machine learning.

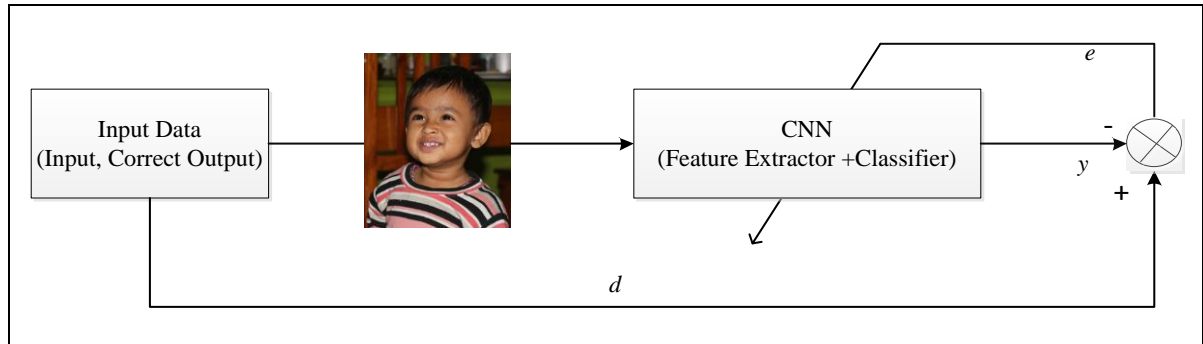


Figure 3.14: Basic architecture of a typical CNN.

The CNN is one of the best approaches in the field of DNN. CNN is quite alike to the ordinary neural networks having learnable weights and biases. Each neuron receives some inputs, performs a dot product and optionally follows it with a non-linearity. CNN represents a specialization of the conventional neural networks where the individual neurons create a mathematical estimation of the biological visual receptive field (BVRF) [42]. It means the CNN is not only a DNN that contains the many hidden layer but also it imitates the procedure of human visual cortex to recognize images. Before the usage of the CNN, the network designer has to extract the features of the training images for SNN that needs experts in that field. So, it required unusual time and cost and it also returned an unexpected level of performance. Such a procedure of SNN can be briefly explained in **Figure 3.13**. On the other hand, CNN includes this feature extraction step in its training process rather than manual performing step as the SNN. The CNN uses a special kind of neural network where the weights are determined itself inside its training process. So, CNN reduces the time and cost of the feature extraction step for the classification. Using the CNN, we get the benefit of automated process of feature extraction and classification as its internal training process which is shown in **Figure 3.14** as the training concept of CNN.

Architecture of A CNN: The basic structure of a CNN consists of a number of layers. In each parallel path, there is a convolutional layer. A convolutional layer is followed by a batch normalization layer, a rectified linear unit (ReLU) activation layer and a max pooling layer. An inception block extracts the feature maps from the input images which are concatenated and passed on to a global average pooling layer. Eventually, there is a two unit dense layer with a softmax activation layer which

gives the categorical probability. To prevent the overfitting problem, the weights of the dense layers are L2 regularized. The individual steps of the different layer are described below.

i) Convolutional Layer: A convolution layer generates a set of new images those are called *feature maps*. The feature map highlights the exclusive features of the actual image. The convolution layer operates in a very different way compared to the other neural network layers. This layer is not involved in the measures of the weights or weighted sum. The impact of the convolutional layer can be compared to filtering effect and it is also known as *convolution filters*. **Figure 3.15** exhibits the functioning of the convolution layer where ‘ \otimes ’ denotes the convolution operation and ‘ \square_{φ} ’ denotes the activation function. In case of a traditional CNN, the filters of a particular layer could have the same window length and this procedure is gradually reduced in the subsequent layers [43]. Although there is no exact rule to consider the window length of the filter, the window length is generally considered experimentally. The feature maps are computed through the convolutional layers by convolving the preceding layer with a defined kernel. Suppose that, M^l is a feature map regarding the layer l as well as M^{l-1} is a feature map of the previous layer. Again consider that M_w and M denotes the width and height of the feature map, respectively and the width and height of the kernels are indicated by the K_w and K_h . During a convolution operation, consider that S_w and S_h characterizes the horizontal and vertical steps of the kernels, respectively.

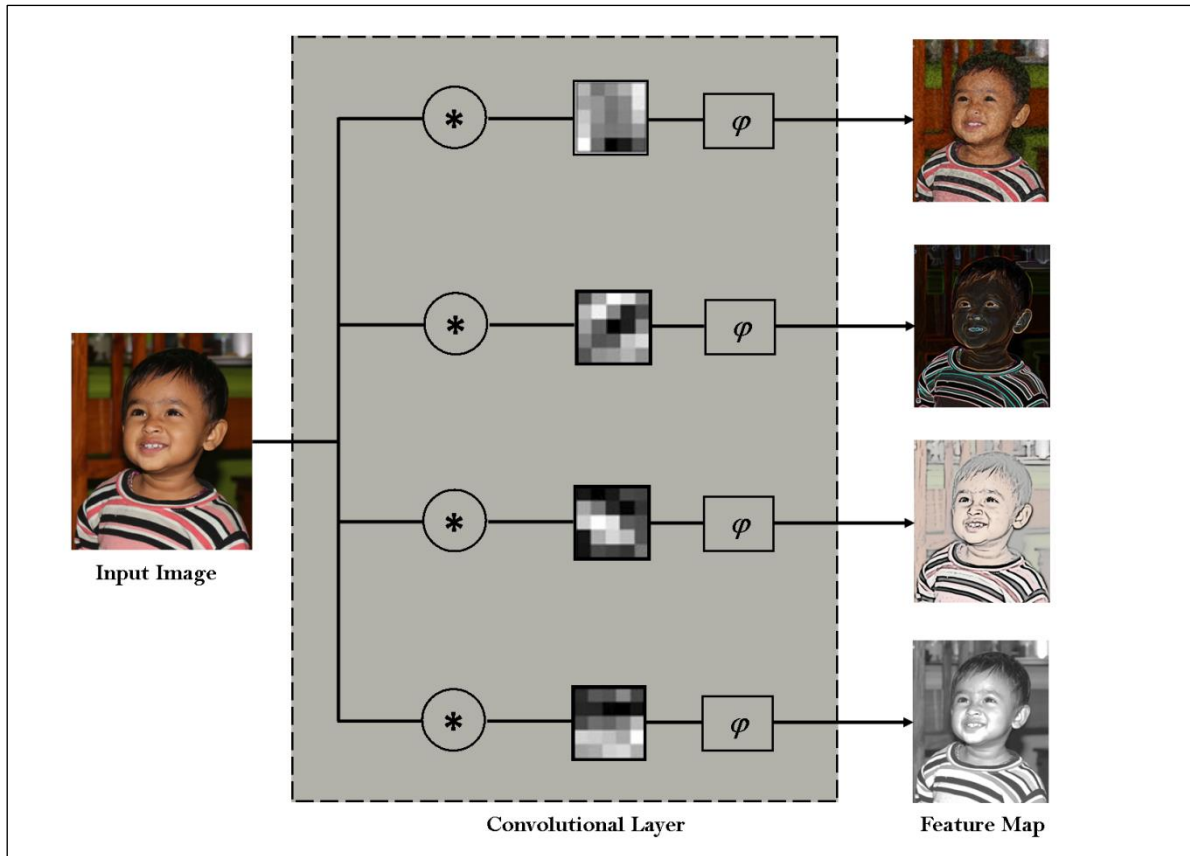


Figure 3.15: The basic process of a convolutional layer in CNN.

Therefore, the size of the output feature map depends on the size of feature maps of the previous layer, kernels and stepping factors [44]. The output width and height of the feature maps are then found as,

$$M_w^l = \frac{M_w^{l-1} - K_w}{S_w} + 1 \quad (3.36)$$

$$M_h^l = \frac{M_h^{l-1} - K_h}{S_h} + 1 \quad (3.37)$$

ii) Batch Normalization Layer: According to the changes of the training parameters of a convolutional layer, the corresponding output will also be changed. The regarding layers are to adapt continuously to the new distributions that require it to be a slow learning rate. This occurrence is known as internal covariate shift [45]. To overcome this issue, an additional layer is to add after the convolutional layer which is referred to a *batch normalization layer* or regularizer. This layer performs a normalization step that is able to fix the mean and variance of the regarding layer

inputs. As a result, faster training time can be achieved using higher learning rate. A typical batch normalization algorithm has been presented below.

Input: Values of x over a mini-batch: $B=\{x_1, x_2, \dots, x_m\}$;
Parameters to be learned δ, β

Output: $\{y_i=BN_{\delta,\beta}(x_i)\}$ [$BN(\circ)$ =Batch Normalization Function]

$$\mu_B \leftarrow \frac{1}{m} \sum_{i=1}^m x_i \quad // \text{ mini-batch mean}$$

$$\sigma_B^2 \leftarrow \frac{1}{m} \sum_{i=1}^m (x_i - \mu_B)^2 \quad // \text{ mini-batch variance}$$

$$\hat{x}_i \leftarrow \frac{x_i - \mu_B}{\sqrt{\sigma_B^2 + \epsilon}} \quad // \text{ normalize}$$

$$y_i \leftarrow \delta \hat{x}_i + \beta \equiv BN_{\delta,\beta}(x_i) \quad // \text{ scale and shift}$$

iii) ReLU layer: The word ReLU means rectified linear [46] layer which persuades a nonlinearity in the incoming layer's values. This ReLU layer can be summarized as a mathematical function given below.

$$f(x) = \begin{cases} x & \text{if } x > 0 \\ 0 & \text{if } x \leq 0 \end{cases} \quad (3.38)$$

So, this function passes the values x in the condition of being greater than 0. Some other functions are also utilized in this case to upsurge non-linearity, such as the saturating hyperbolic tangent function $f(x) = |\tanh(x)|$, logistic function

$$f(x) = \frac{2}{1 + e^{-\beta x}} - 1 [47], \text{ hyperbolic tangential sigmoidal function } f(x) = 1.7159 \tanh\left(\frac{2}{3} x\right)$$

[48], and the sigmoidal function $f(x) = \frac{1}{1 + e^x}$. It is often preferred utilizing the ReLU

layers with the other functions because it helps to train the neural network faster beyond facing a significant penalty to the generalization accuracy.

iv) Max Pooling Layer: The *pooling layer* combines the neighbor pixels of a defined area of the image into a group of features by one feature and thus it reduces the dimensionality of the feature maps. There are several types of pooling operations but the widely used pooling layers are mean pooling layer and maximum pooling

layer. Usually, the mean pooling layers are used in earlier works [49] whereas recent works prefer the maximum pooling layer because it always outperforms the mean pooling operation [50]. Suppose, we have a 4×4 pixel input image as given in **Figure 3.16**. The operation of a mean pooling and a max pooling are given in the example. We also get that the dimensionality of the input image of the pooling layer becomes reduces after being the operation of the pooling layer. Since the pooling process reduces the image size, it is highly helpful for the getting rid of the computational load and avoiding the issue of overfitting.

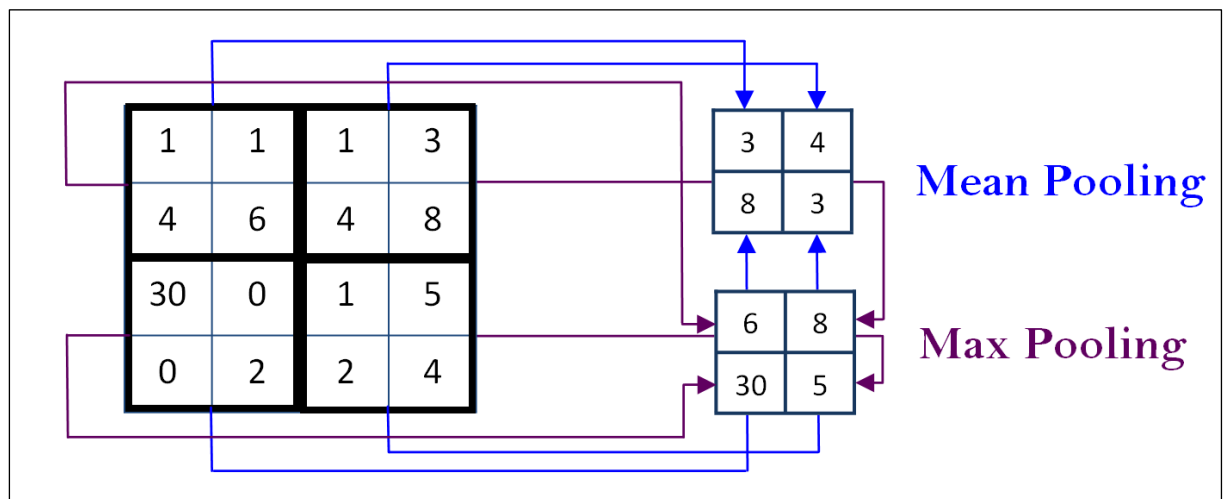


Figure 3.16: A simple example of the process of mean and max pooling operation

v) Fully Connected Layer: To detect the high level features, a fully connected layer is attached to the end of a CNN. This layer basically takes the output of the conv or ReLU or pooling layer as input and set an output as an N dimensional vector where N is the number of defined classes to be classified. As for example, if we want to classify the digits then the number of N will be 10. The individual number of this N dimensional vector presents the classification probability of a specific class. Suppose that, in case of digit classification problem the resulting vector we get is $[0.1 \ 0.2 \ 0.65 \ 0 \ 0 \ 0 \ 0 \ 0.05]$. Therefore, the result gives that the number has a chance to be 1 (10%), 2 (20%), 4(65%), and 9 (5%) (according to the softmax approach). By this way, fully connected layer looks at the output and determines which features most correlate to a particular class. Basically, a fully connected layer looks at what high level features most strongly correlate to a particular class and has particular weights

so that when you compute the products between the weights and the previous layer, you get the correct probabilities for the different classes [51].

3.6 Conclusion

In this chapter, the basic steps of the signal processing methods have been widely discussed. In addition, this chapter proposes a novel approach to combine the fNIR and EEG signal to produce a neuroimage compatible to the CNN classifier. Besides, a novel classification mechanism is proposed in this chapter to classify the voluntary and imagery related prefrontal hemodynamics from the proposed model equation obeying the rule of maximum likelihood approach. The conventional feature extraction procedure and the existing widely used classifiers are also discussed in this chapter with their mathematical interpretation. These methods will be used frequently for the processing and finding the objective outcomes of this dissertation. In the next chapters, these methods will be mentioned without its mathematical details and presented the effect of these methodologies in the signal processing aspects.

CHAPTER 4

Statistical Modeling of Voluntary and Imagery Movement

4.1 Introduction

This chapter concerns with the modeling and classification of voluntary and imagery movements from the prefrontal fNIR signals. In this work, four different movements of hands and feet have been considered as both voluntary and imagery manner. According to these stimuli, fNIR data were recorded from the prefrontal cortex of several young and healthy male subjects. With proper signal pre-processing, the fNIR data were separated based on their class. Then, analysis of variance (ANOVA) was used to localize the most significantly activated area regarding the stimuli. The ANOVA results were verified by effect size (ES) estimation. The temporal pattern of the change in the concentration of both HbO₂ and dHb signals regarding the mostly significant areas were modeled by polynomial regression. Utilizing the model activation patterns, a simple statistical classifier has been proposed based on the spatiotemporal maximum similarity approach. This proposed classification algorithm has been utilized to classify the movement related fNIR signals. For classification of the fNIR signal, two, four, and six class problems were considered. Plus, we utilized the conventional time domain feature extraction and classification strategy to classify the signals by four different classification algorithms. We found that the classification accuracies of the proposed and conventional methods are almost similar. Eventually, this work has contributed to revealing- *i*) The most significant activation regions for the different voluntary and imagery movements in the prefrontal cortex, *ii*) The modelled hemodynamic activation pattern based on the HbO₂ and dHb concentration, and *iii*) Classification of the multiple-class fNIR signals using the model activation pattern. The overall idea of the proposed research framework is given in **Figure 4.1**.

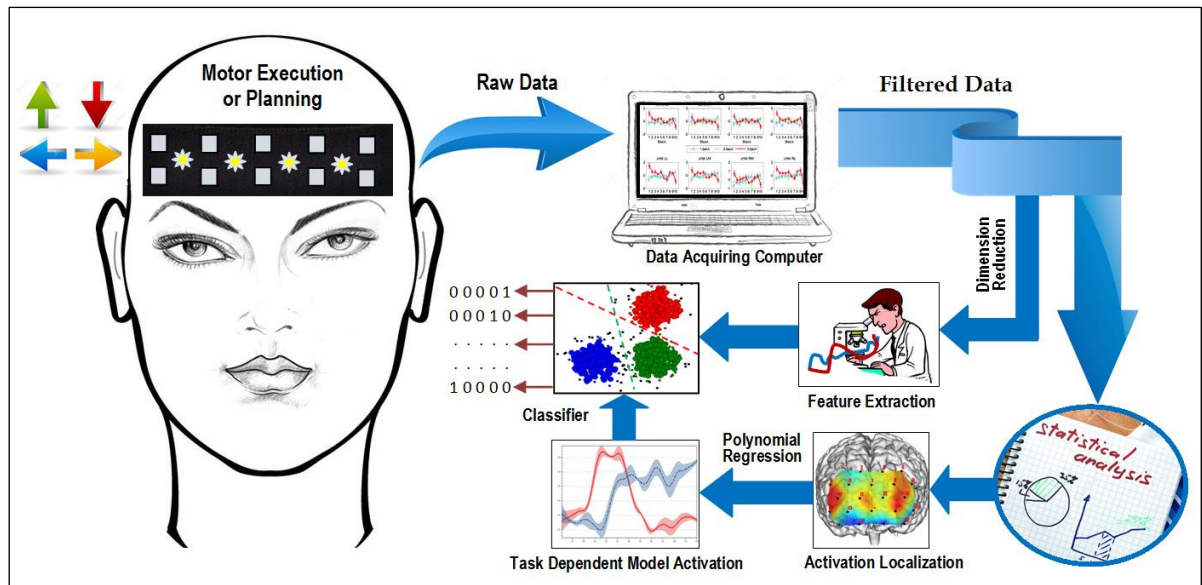


Figure 4.1: An illustration to describe the framework of this research work. This work localizes the significant activated areas regarding voluntary & imagery movements and models those hemodynamic activation patterns. The fNIR signals corresponding to the different movement related tasks have been classified by several machine learning algorithms considering the polynomial regression coefficients as features.

4.2 Materials and Methods

4.2.1 Data Acquisition Protocol

In this work, every participant performed eight different movement related tasks (four voluntaries + four imageries). Since most significant voluntary movements of the human beings are performed by hands and feet, the movements by hands and feet (by means of voluntary and imagery) were considered for the neural stimuli. The subjects were verbally informed about the protocol of the data acquisition and according to the protocol all the subjects lifted their left hand, right hand, left foot, and right foot, sequentially.

These four movements were performed in two compartments: *i*) voluntary and *ii*) imagery. The time scheduling for the data acquisition protocols is given in **Figure 4.2**. In one session this unit protocol was performed four times by a participant. After every session, each participant took rest at least five minutes. Eventually, every participant performed 20 trials for each movement related task. A Matlab based graphical protocol (as **Figure 4.3**) was designed for this research work that helped the participants by providing the instructions to make the data acquisition procedure easy with proper scheduling. The code of the designed graphical protocol is

freely available in [1]. This program blinked according to the scheduled tasks and instructed the participant to follow and perform the tasks. In this graphical program, five different tasks were arranged and those were movements of the left hand, right hand, left foot, right foot, and rest. Finally, eight different tasks have been considered for analysis those are voluntary left hand (LH), right hand (RH), left foot (LF), right foot (RF) and imagery left hand (iLH), right hand (iRH), left foot (iLF), and right foot (iRF).

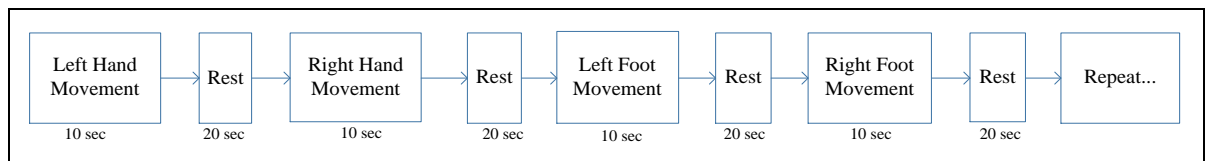


Figure 4.2: Time schedule of data acquisition protocol for each participant regarding both the voluntary and imagery movements. This is a unit task performing schedule that was repeated four times in each session to complete 20 individual trials of every task.

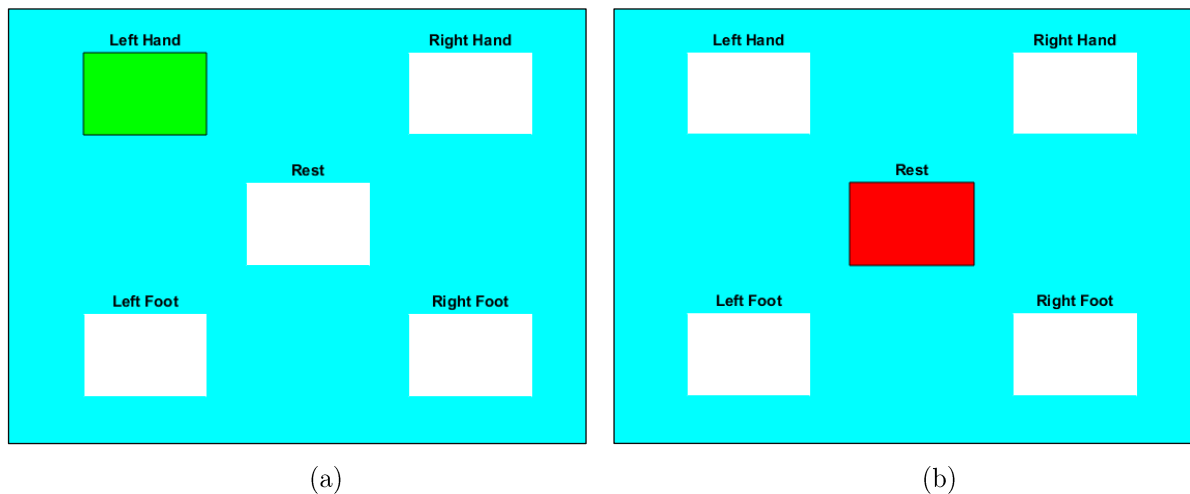


Figure 4.3: Schematic illustration of MATLAB based protocol instruction aiding application for the experiment. Regarding the instruction of this application, the participant is asked to move left hand (voluntary or imagery) by Figure 4.3(a) and after that, Figure 4.3(b) instructs to take rest.

4.2.2 Data Acquisition

Thirty-five male subjects (age range=20 to 25) participated in the data acquisition procedure among them the recorded signals of four participants were excluded due to their poor signal quality. All participants were tested and found right handed depending on the recommendation of Edinburg Handedness Inventory [2]. No participants had any history of the psychiatric, neurological or visual disorder. In addition, no participant had pain in their both hands and feet. Also, their verbal consents were taken before the data acquisition related to this research work as the

rule of the university. All data acquisition procedures were completed in the Neuroimaging Laboratory of the Biomedical Engineering department of KUET obeying the declaration of Helsinki [3].

For this work, a 16 channel continuous-wave fNIR system (model: Biopac 1200 fNIR imager) was used. By the system, hemodynamic signals from the prefrontal cortex were acquired from all the participants. The optode band for data acquisition for this fNIR system contains four NIR light sources and 16 detectors. The physical configurations of the optode band on prefrontal cortex are given in **Figure 4.4**. The data sampling rate was 2 Hz and COBI (cognitive optical brain imaging) software [4] was used for data acquisition. The total hardware configuration associated with the data acquisition is presented in **Figure 4.5**.

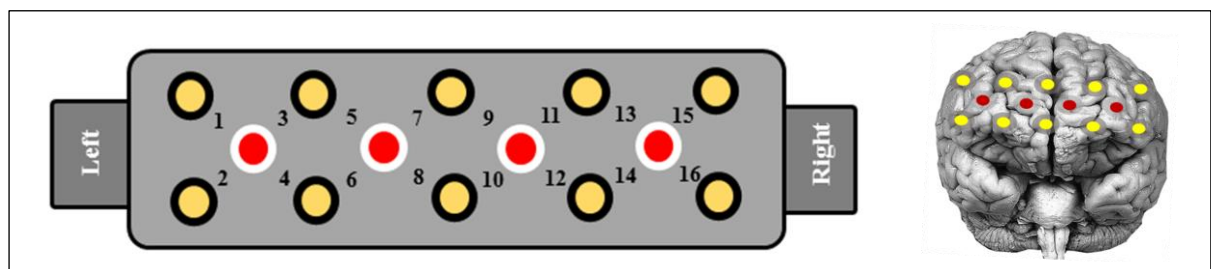


Figure 4.4: The optode and channel configurations of fNIR devices (Model 1200) sensor pad.

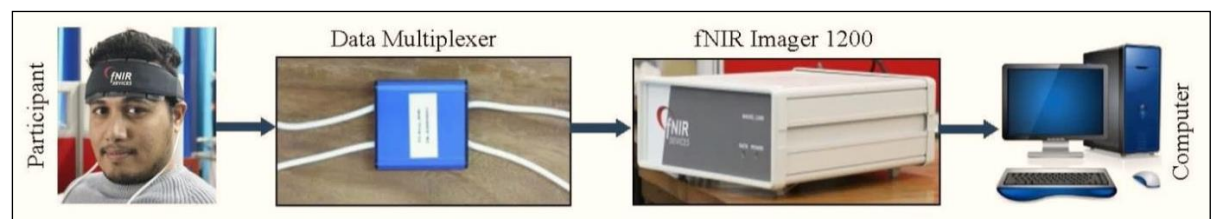


Figure 4.5: Data acquisition procedure from participant connecting by used hardware.

4.2.3 Preprocessing

At first all the fNIR signals were separated according to the tasks and thereafter signals of same tasks for all the participants were arranged in individual arrays. Since we used 16 channel fNIR system, the 16 channel fNIR data carry the information of 16 different spatial positions of the prefrontal cortex. The positions and corresponding channels are shown in **Figure 4.3**. Interestingly, all these channels are not linearly uncorrelated. To check the linearly correlated and uncorrelated channels,

principal component analysis (PCA) was applied and found that the signals are of four dimensions. The linearly uncorrelated profiles of the channels have been shown in **Figure 3.2** where the Eigen-space is formed by the three principal components. In this consequence, the prefrontal cortex has been divided into four major region of interest (ROI) those are- Left Lateral (LL: includes channels 1, 2, 3, & 4), Left Medial (LM: includes channels 5, 6, 7, & 8), Right Medial (RM: includes channels 9, 10, 11, & 12), and Right Lateral (RL: includes channels 13, 14, 15, & 16) [5]. It is found that the 4 signals corresponding to four channels in every defined region show a very strong correlation ($0.95 < r < 1$). The detail mechanism of the fNIR data compression has been given in the previous chapter.

SG filter with frame length 19 and order 3 was used to filter the noisy fNIR signal. For smoothing the fNIR signals, we have used SG filter because of its special benefit *i.e.*, SG filter is better than FIR filter for removing high-frequency contents from signals. Because, in the case of FIR filter, the euclidian distance between original and filtered signal is more than SG filter [6]. Furthermore, employing SG filter needs no delay correction as an FIR filter. For each trial of the fNIR data had been corrected by subtracting the baseline from the original signal. Baseline was calculated from the average of the first 2 seconds of the task. The baseline correction procedure has been already discussed in Chapter 3.

4.2.4 Statistical Analysis & Activation Modeling

One-way repeated ANOVA was used to find the significant ROI for each activity, separately. The signal mean was taken from three sample window (0-10, 10-20, and 20-30 samples) for one-way repeated measures of ANOVA. The mathematical detail of the ANOVA has been described in the Appendix section. Student's *t*-distribution statistics were also used to find the significant difference between the hemispheres regarding any voluntary or imagery event. Since the *p* values of ANOVA is not enough to find the significance level for a big dataset [7], we also calculated effect size (ES) of the event to localize the hemodynamic activation. Statistically, we can find the difference of activation level by the use of ES calculation. ES is a simple statistical method of measuring the difference between groups of mental activation due to external excitation and resting state activation. The common way to

calculate ES is *Cohen's d* method. Suppose that, x_1 and x_2 are the mean values of the entries of group 1 and 2, respectively, then, the ES between x_1 and x_2 is calculated by the method as [8],

$$d = \frac{\bar{x}_1 - \bar{x}_2}{\sqrt{\frac{(N_1 - 1)S_1^2 + (N_2 - 1)S_2^2}{N_1 + N_2}}} \quad (4.1)$$

Here, N_1 and N_2 are the numbers of entries in each vector and S_1 and S_2 are the standard deviation of the dataset, respectively. The ROI's satisfied the significance by both ANOVA and ES test were considered for most significant activated ROI for a specific event. After that, the signals of all trials from all subjects were averaged to fit as model activation pattern regarding the event by polynomial regression. To fit a time series of data by polynomial fitting or regression, we generally consider a polynomial equation as an estimation function and suppose the estimation function, $E(x)$ is of k^{th} degree polynomial that can be presented as,

$$E(x) = a_0 + a_1x + a_2x^2 + \dots + a_kx^k \quad (4.2)$$

Therefore, the difference between actual value, Y and the estimated value derived by the proposed model estimating equation, $E(x)$ is termed as residual, $R^2 = |E(x) - Y|^2$. For achieving the best fitted estimated model equation, it is the foremost target to minimize the value of the residual. It is reported in [9][26] that hemodynamic activations can be modeled by polynomial fitting with the value of $k = 5$. In this work, $k = 5$ has been taken to get the minimum value of residual and for the coefficient, a^i at the minimum error condition, the partial derivative of R^2 is zero. To achieve the regression with k^{th} polynomial we get,

$$\begin{bmatrix} y_1 \\ y_2 \\ \cdot \\ \cdot \\ y_n \end{bmatrix} = \begin{bmatrix} 1 & x_1 & x_1^2 & \cdot & \cdot & x_1^k \\ 1 & x_2 & x_2^2 & \cdot & \cdot & x_2^k \\ \cdot & \cdot & \cdot & \cdot & \cdot & \cdot \\ \cdot & \cdot & \cdot & \cdot & \cdot & \cdot \\ 1 & x_n & x_n^2 & \cdot & \cdot & x_n^k \end{bmatrix} \begin{bmatrix} a_0 \\ a_1 \\ \cdot \\ \cdot \\ a_k \end{bmatrix} \quad (4.3)$$

The previous relation can be represented as,

$$Y = Xa \quad (4.4)$$

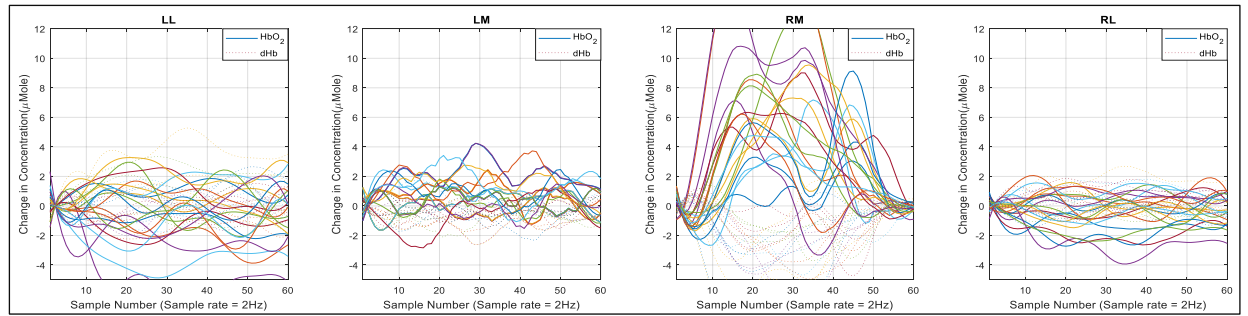
Here, X is a vandermonde type matrix. This can be solved as,

$$\begin{aligned} X^T Y &= X^T X a \\ \text{or, } a &= (X^T X)^{-1} X^T Y \end{aligned} \quad (4.5)$$

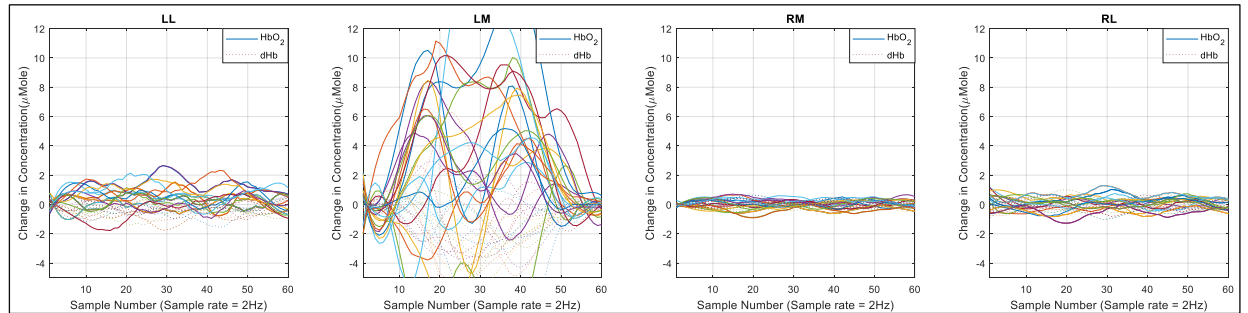
The order of the polynomial equation was estimated from the error performance of the fitted results. A satisfactory level of error was taken as the threshold for different activation modeling.

4.3 Results and Discussions

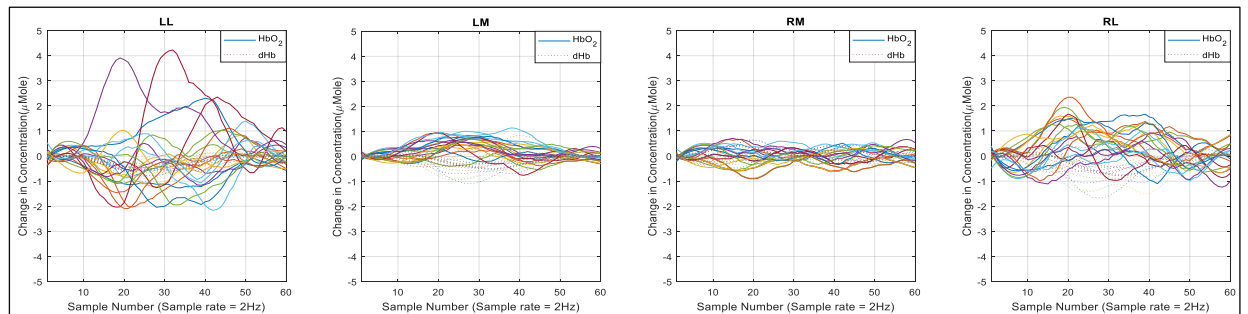
The activations of the four voluntary and imagery movements have been presented in **Figure 4.6** and **Figure 4.7**, respectively. This is a result of an arbitrarily selected participant. The results have been presented after separating the data based on the ROI's, correcting baseline, and filtering. In the figures, both HbO₂ and dHb activation patterns have been presented. From the graphical depiction of the neural activations, the most significant activated areas and the activation patterns can be assessed. From the hemodynamic responses (HbO₂ and dHb) of four voluntary and four imagery tasks have been given regarding four ROI's (LL, LM, RM, and RL). From the results of **Figure 4.6**, we get the voluntary hand movements to create significant activation in the prefrontal cortex. The hemodynamic responses due to voluntary movements of the left and right hand show contralateral activation in the opposite hemisphere. Due to the left-hand movement, the activation is noticeable in the RM region of the prefrontal cortex and oppositely the LM region is activated due to the right-hand movement. The other regions show the random activation which does not indicate the clear hemodynamic activation. On the other hand, the voluntary movements of the left and right feet also show random activations as given in **Figure 4.6(c)** and **Figure 4.6(d)**. From the results of imagery movements given in **Figure 4.7**, we find that the hemodynamic activations due to the imagery hand movements show similarity with the voluntary movements but the activation strength is lower than that of the voluntary movements. In addition, the imagery feet movements show significant activation in the lateral area of the prefrontal cortex. The imagery left and right foot activates the right and left hemisphere of the prefrontal cortex, respectively where the activations of the RL and LL regions are mostly noticeable as given in **Figure 4.7(c)** and **Figure 4.7(d)**.



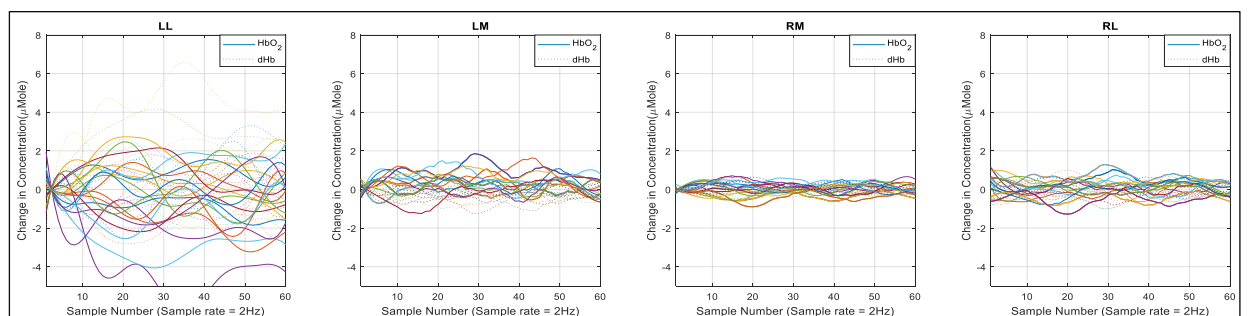
(a)



(b)

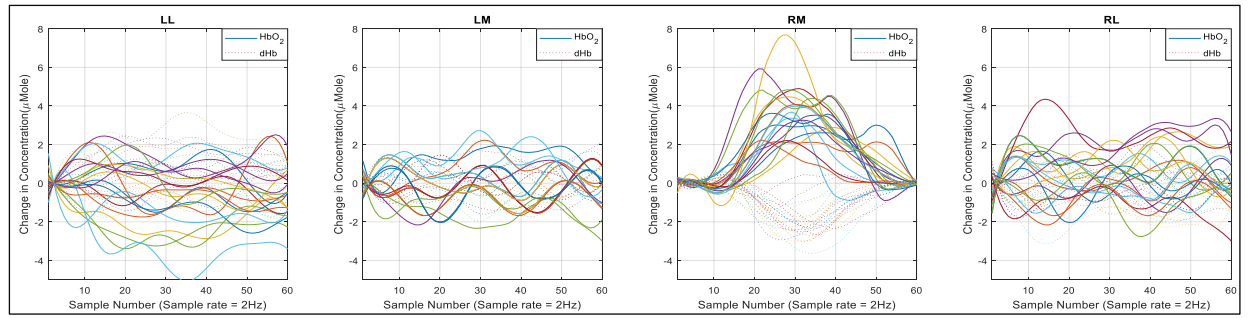


(c)

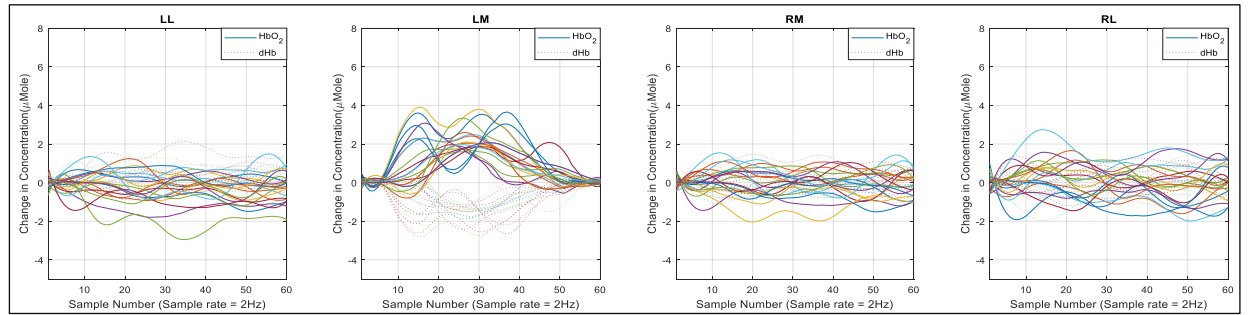


(d)

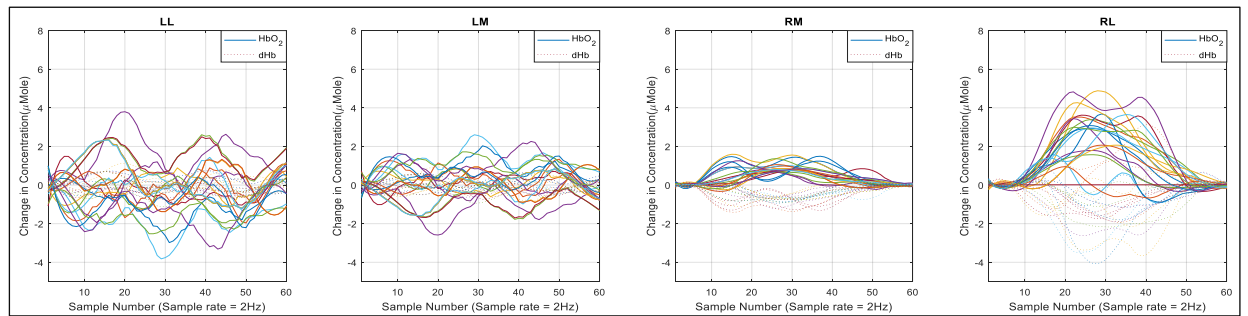
Figure 4.6: The change in hemodynamic concentration (HbO_2 and dHb) regarding the movement execution stimuli: LH (a), RH (b), LF (c), and RF (d) correspond to the ROI's: LL, LM, RM, and RL. It is the hemodynamic activations of a single participant. The activations are regarding 20 trials of four movement execution tasks.



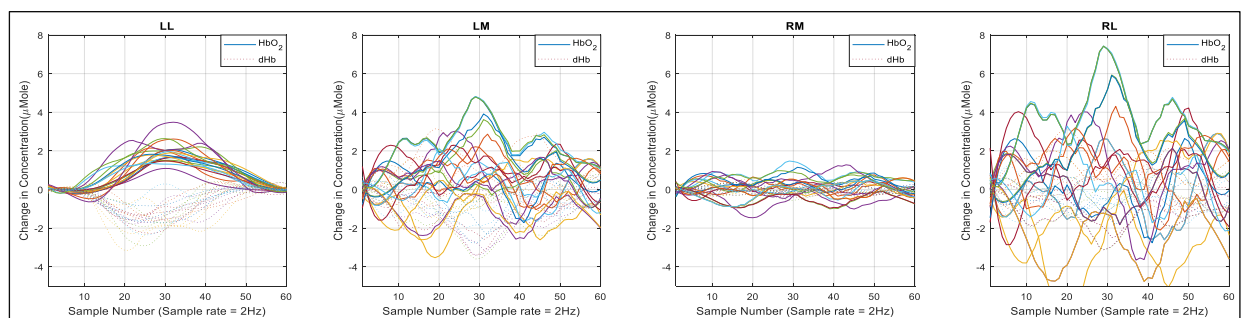
(a)



(b)



(c)



(d)

Figure 4.7: The change in the concentration of HbO_2 and dHb regarding the imagery movement stimuli: iLH (a), iRH (b), iLF (c), and iRF (d) correspond to the ROI's: LL, LM, RM, and RL. It is the hemodynamic activations of the same participant as the data of Figure 7. Here, there are 20 trials of four imagery movement tasks.

To examine the significant neuro-activation considering the data of the total population involved in this research, statistical analysis, ANOVA was performed. One way repeated measures (three levels: 0-5, 5-10, and 10-15 sec) ANOVA was performed on the fNIR data of the tasks (left-hand, right-hand, left-foot, and right-foot movement as voluntary and imagination manner) to reveal the significant activation localization of the region of interests (LL, LM, RM, and RL). The ANOVA was conducted on the mean value of HbO₂ and dHb concentration. From the results of ANOVA, the following significant hypothesis has been found:

LH & iLH: Due to the left hand movement execution and imagination, significant ($p < 0.001$) increase of HbO₂ concentration ($F(2,90) = 108.34$, for voluntary movement, $F(2,90) = 106.35$ for imagery movement) and decrease of dHb concentration ($F(2,90) = 103.58$ for voluntary movement, $F(2,90) = 80.73$ for imagery movement) were occurred in RM region of PFC. Moreover, other regions showed insignificant activations ($p > 0.01$). The effect of the hemisphere on the left-hand movement (voluntary and imagery) was tested by t -distribution on the mean value of HbO₂ concentration of left and right hemisphere. The right hemisphere (RM+RL) showed the significant difference ($t = 6.7510$, $p < 0.001$ for movement execution and $t = 5.6555$, $p < 0.001$ for imagery movement) than the left hemisphere (LL+LM). Moreover, the activated region (RM) due to the task (left hand voluntary and imagery movement) showed significant ES (2.4439 and 1.5233) with compared to the control (rest) state.

RH & iRH: Due to the right hand movement as voluntary and imagery, significant ($p < 0.001$) increase of HbO₂ concentration ($F(2,90) = 195.67$ for voluntary movement & $F(2,90) = 56.62$ for imagery movement) and consequently there occurred a significant decrement in dHb concentration ($F(2,90) = 138.8$ for voluntary movement, $F(2,90) = 40.39$ for imagery movement) in LM region of PFC. Moreover, other regions showed insignificant activations ($p > 0.01$). The effect of the hemisphere on the left-hand movement (voluntary and imagery) was tested by t -distribution on the mean value of HbO₂ concentration of left and right hemisphere. The left hemisphere (LL+LM) showed the significant difference ($t = 13.4297$, $p < 0.001$ for movement execution and $t = 4.2874$, $p < 0.001$ for imagery movement) with the right hemisphere (RM+RL). Moreover, the activated region (LM) due to the task (movement of the right-hand as voluntary and imagery manner) showed significant ES (1.6527 and

1.1997) than the control (rest) state. In case of voluntary and imagery movements of LH and RH some other regions showed significant activation ($p < 0.01$) based on the results of repeated ANOVA (see **Table: 4.1**) but for large observations the p value is not enough [51] for taking a statistical decision. Therefore, we also considered the value of ES to confirm the activation strength of the concerned ROI. The regions showed the significant ES have been considered as the significantly activated regions for the corresponding task (see the **Table: 4.1**).

Table 4.1: The statistical results of the activations regarding all voluntary and imagery stimuli. Here, both results of ANOVA and ES are tabularized.

Region of Interest (ROI)	F(2,90), p values [significance level=(<0.001)]				Effect Size (ES)	
	Movement Execution		Imagery Movement			
	LH				Movement Execution	Movement Imagery
	HbO ₂	dHb	HbO ₂	dHb		
LL	5.16, 0.0092	4.9, 0.0109	6.12, 0.0032	5.9, 0.0039	-1.6009	-0.9602
LM	2, 0.1416	1.8, 0.1718	0.1, 0.9068	0.09, 0.9116	-0.6344	-1.1246
RM	108.34, <0.001	103.58, <0.001	106.3, <0.001	80.73, <0.001	2.4439	1.5233
RL	0.46, 0.6323	0.44, 0.6455	0.13, 0.8793	0.12, 0.8851	0.4930	0.6684
	RH					
LL	2.4, 0.1126	1.8, 0.1718	0.83, 0.4372	0.78, 0.4593	0.1305	0.0321
LM	195.67, <0.001	138.8, <0.001	56.62, <0.001	40.39, <0.001	1.6527	1.1997
RM	3.53, 0.0129	6.73, 0.0018	0.45, 0.6379	0.42, 0.66	-0.6590	-1.3082
RL	20.32, <0.001	24.99, <0.001	0.48, 0.6321	5.9, 0.0039	0.0232	-0.4930
	LF					
LL	0.49, 0.6149	0.42, 0.6598	2.0, 0.1416	1.8, 0.1718	-1.011	-0.5641
LM	0.43, 0.6506	0.49, 0.613	2.0, 0.1416	1.8, 0.1718	-0.7519	-0.6344
RM	0.77, 0.4652	0.94, 0.3954	56.62, <0.001	40.39, <0.001	-0.73477	-0.2693
RL	5.85, 0.0041	5.6, 0.0051	330.16, <0.001	265.94, <0.001	0.2631	3.0541
	RF					
LL	2.43, 0.094	0.57, 0.6598	300.71, <0.001	246.56, <0.001	0.2097	1.1872
LM	0.52, 0.5949	0.41, 0.8667	358.22, <0.001	314.48, <0.001	-0.7654	-0.2292
RM	0.22, 0.7998	0.23, 0.7929	2.95, 0.0573	2.5, 0.0878	-0.8489	-0.6692
RL	0.37, 0.6929	0.4, 0.6747	10.47, <0.001	12.87, <0.001	-1.1874	0.6232

LF & RF: The data regarding the voluntary movements of the left and right foot showed no significant activation either in HbO₂ or dHb concentration with

insignificant ES. Since the activation region of the lower body part is situated in the deep brain, this inactiveness may occur. This result suggested us to advise the participants to concentrate deeply to imagine the feet movement during data acquisition so that there a significant cognitive load may occur in the prefrontal cortex. In case of left and right foot imagery movement, several ROI's were found as significant according to the results of ANOVA. Due to the LF imagery movement showed the significant activations in RL ($F(2,90)= 56.62$, $p<0.001$ for HbO₂ and $F(2,90)= 40.39$, $p<0.001$ for dHb) and RM ($F(2,90)= 330.16$, $p<0.001$ for HbO₂ and $F(2,90)= 265.94$, $p<0.001$ for dHb). However two different regions (RM & RL) showed significant activations with the ANOVA outcomes, only the RL region showed significant ES (3.0541). As a result, only the RL region can be considered as the responsible area of interest for the activation of LF imagery movement. Similarly, from the one-way repeated ANOVA test several significant activated regions are found for the right foot movement (LL: $F(2,90)= 300.71$, $p<0.001$ for HbO₂ and $F(2,90)= 246.56$, $p<0.001$ for dHb, LM: $F(2,90)= 358.22$, $p<0.001$ for HbO₂ and $F(2,90)= 314.48$, $p<0.001$ for dHb, and RM: $F(2,90)= 10.47$, $p<0.001$ for HbO₂ and $F(2,90)= 12.87$, $p<0.001$ for dHb). Although three different regions were found as activated according to the ANOVA results, two of them showed significant ES values (LL: 1.1872 and RL: 0.6232) and between them, only the LL showed the highest (around two times than RL) ES value. Therefore, LL is the most significant region of activation due to the imagined movement of RF. All the results regarding ANOVA and the ES have been tabulated in **Table 4.1**. The statistical results of ANOVA and ES, the most significant areas were selected according to the stimuli. Based on these results, the concentration changing pattern of HbO₂ and dHb regarding the most activated area were averaged from the data of all the trials of all participants. The activation patterns of HbO₂ and dHb of the corresponding stimuli have been presented with their error disparity by **Figure 4.8**. Moreover, to show the activation pattern due to the voluntary and imagery movements in the total area of the prefrontal cortex the functional neuroimages are given in **Table 4.2**. These functional neuroimages have been prepared based on the grand average value of the total population dividing five equal windows from the beginning of the task to the end of the trial. The concentration changes of the HbO₂ were considered here to

construct the neuroimages where the activation level was registered on the MRI brain images. The total area covered with the activation level of the 16 channels was done with 20 point B-Spline interpolation technique using the fNIRSoft [10],[67].

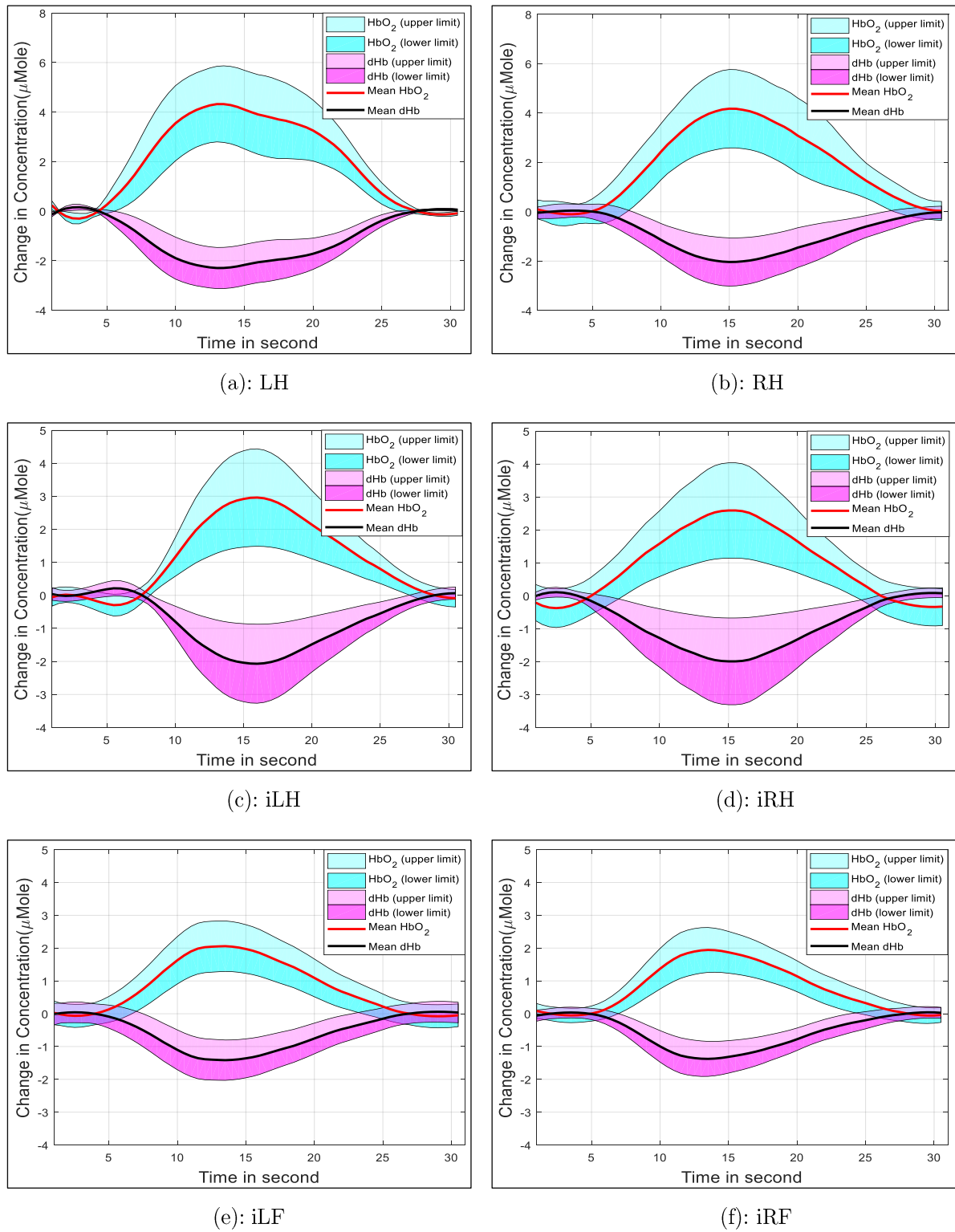
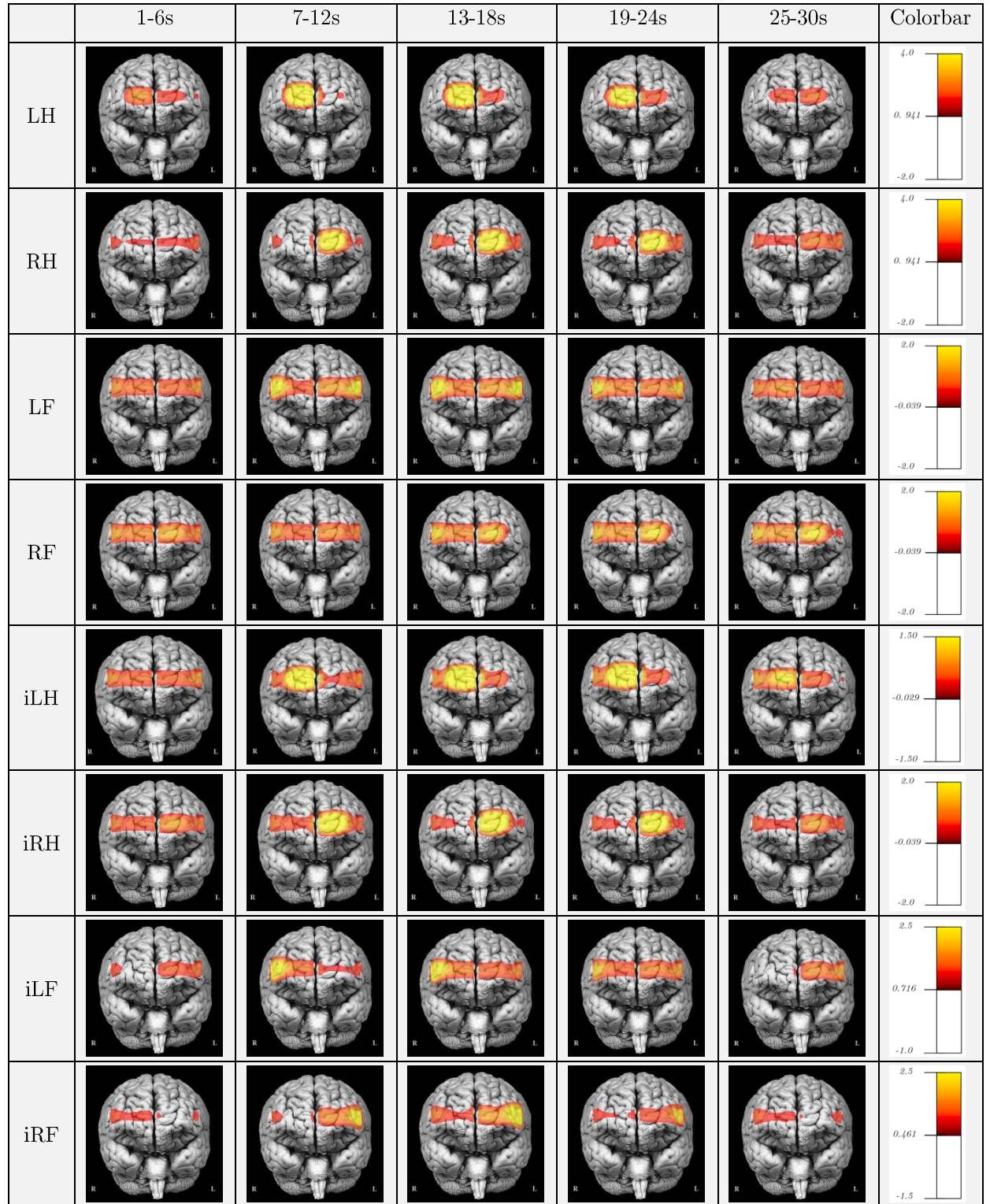


Figure 4.8: The grand average hemodynamic activation pattern (HbO₂ & dHb) from all the trials of all the participants regarding only the most activated regions of prefrontal cortex. Here the activation pattern of LF and RF movements are excluded due to their insignificant ($p > 0.05$) activation level.

Table 4.2: The functional neuroimages of prefrontal cortex regarding different voluntary and imagery movements. These images are prepared from the grand average of all population's trials.



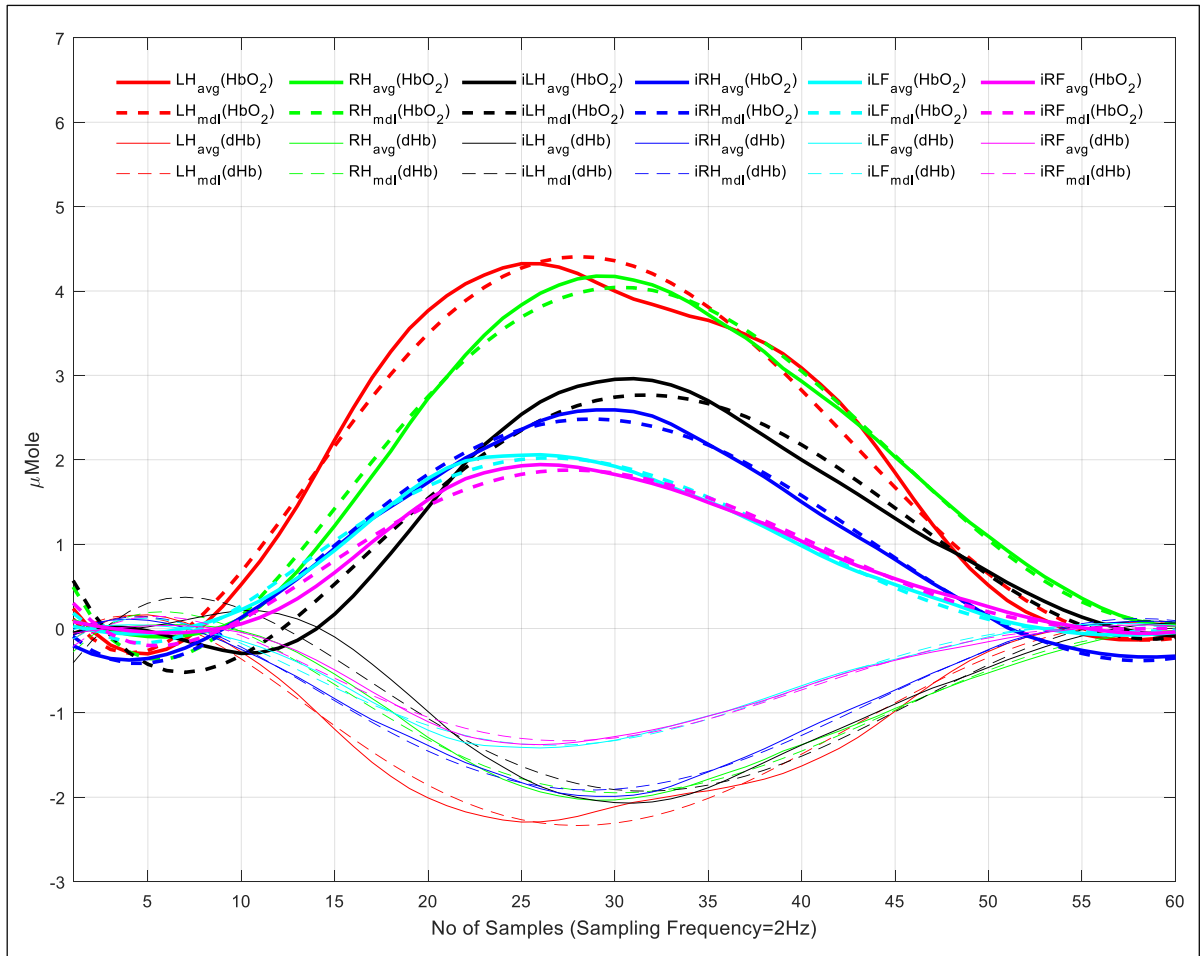


Figure 4.9: The average activation pattern of HbO₂ and dHb of different voluntary and imagery movements and their model activation pattern by 5th order polynomial regression.

The mean value of HbO₂ concentration due to voluntary hand movements (both hands) are more than that of the imagery movements of hands. In addition, the activation level of imagery feet movements is comparatively lowest than the voluntary and imagery movements of the hand. These results reveal that the voluntary and imagery movements of upper limbs show more activation than that of lower limbs. To observe the difference in the concentration of HbO₂ and dHb corresponding to the different stimuli the mean concentrations are given in **Figure 4.9**. The mean concentration changes of HbO₂ and dHb in **Figure 4.9** have been considered as the model activation pattern regarding the stimuli. The model activation patterns of voluntary and imagery movements were modeled by the 5th order polynomial regression. The dotted lines in **Figure 4.9** represent the fitted line by the polynomial regression. The mean concentration of the HbO₂ and dHb have been presented with the solid lines and corresponding fitted curves with 5th order polynomial regression have been presented by the dotted line with the same color of

solid lines. The model equations of the significant voluntary and imagery stimuli regarded activation patterns in the concentration change in HbO₂ and dHb have been given by the following relations (4.6) and (4.7), respectively.

$$\begin{bmatrix} LH(x)_{RM} \\ RH(x)_{LM} \\ iLH(x)_{RM} \\ iRH(x)_{LM} \\ iLF(x)_{RL} \\ iRF(x)_{LL} \end{bmatrix} = \begin{bmatrix} -0.33090 & 0.85623 & 1.58377 & -3.88827 & -1.83626 & 4.20650 \\ -0.26068 & 0.91684 & 0.97558 & -3.90405 & -0.74627 & 4.00871 \\ -0.15412 & 0.80454 & 0.43885 & -3.14731 & -0.12502 & 2.76679 \\ -0.17562 & 0.58642 & 0.82504 & -2.55847 & -0.96458 & 2.39623 \\ -0.27519 & 0.40188 & 1.22956 & -1.75371 & -1.32351 & 1.81244 \\ -0.24658 & 0.43323 & 1.02428 & -1.79568 & -0.99342 & 1.75589 \end{bmatrix} \times \begin{bmatrix} x^5 \\ x^4 \\ x^3 \\ x^2 \\ x^1 \\ x^0 \end{bmatrix}_{HbO_2} \quad (4.6)$$

$$\begin{bmatrix} LH(x)_{RM} \\ RH(x)_{LM} \\ iLH(x)_{RM} \\ iRH(x)_{LM} \\ iLF(x)_{RL} \\ iRF(x)_{LL} \end{bmatrix} = \begin{bmatrix} 0.17856 & -0.44935 & -0.85301 & 2.04847 & 0.98713 & -2.22508 \\ 0.14227 & -0.45453 & -0.52526 & 1.90815 & 0.39006 & -1.92825 \\ 0.10783 & -0.56848 & -0.30631 & 2.21202 & 0.08637 & -1.92738 \\ 0.12302 & -0.41530 & -0.58965 & 1.81203 & 0.69179 & -1.85155 \\ 0.18331 & -0.82022 & -0.82071 & 1.21678 & 0.88556 & -1.24722 \\ 0.18479 & -0.30402 & -0.77679 & 1.25893 & 0.76680 & -1.22939 \end{bmatrix} \times \begin{bmatrix} x^5 \\ x^4 \\ x^3 \\ x^2 \\ x^1 \\ x^0 \end{bmatrix}_{dHb} \quad (4.7)$$

It can be hypothesized that the most activated region for a typical stimulus shows the activation pattern closely correlated with its model equation. Therefore, the maximum temporal similarity pattern with its proper spatial region according to the proposed activation model gives us the class of the signal. Implementing the proposed methodology of the signal classification technique, subject dependent task classification was conducted based on the 2, 4, and 6-class perspectives. The subject dependent classification accuracies of the proposed method have been given in **Figure 4.10**. Here, the results of 2, 4, and 6-class movement-related tasks are given. Moreover, the data classes have been oriented as two classes with iLH and iRH, four classes with iLH, iRH, iLF, and iRF, and six classes with LH, RH, iLH, iRH, iLF, and iRF. From the results we found that utilizing the model activation pattern of the proposed work, the average classification accuracies are 75.16 ± 7.12 (2-class), 57.58 ± 6.69 (4-class), and 38.11 ± 7.74 (6-class). Since the spatiotemporal activation pattern of the LH & iLH and RH & iRH are similar (see **Figure 4.8** and **Figure 4.9**), 6-class classification accuracies are slightly inferior. Further processing is necessary to improve the classification accuracies of 6-class problems. On the other hand, the average classification accuracies of the 2 and 4-class aspects are quite convincing.

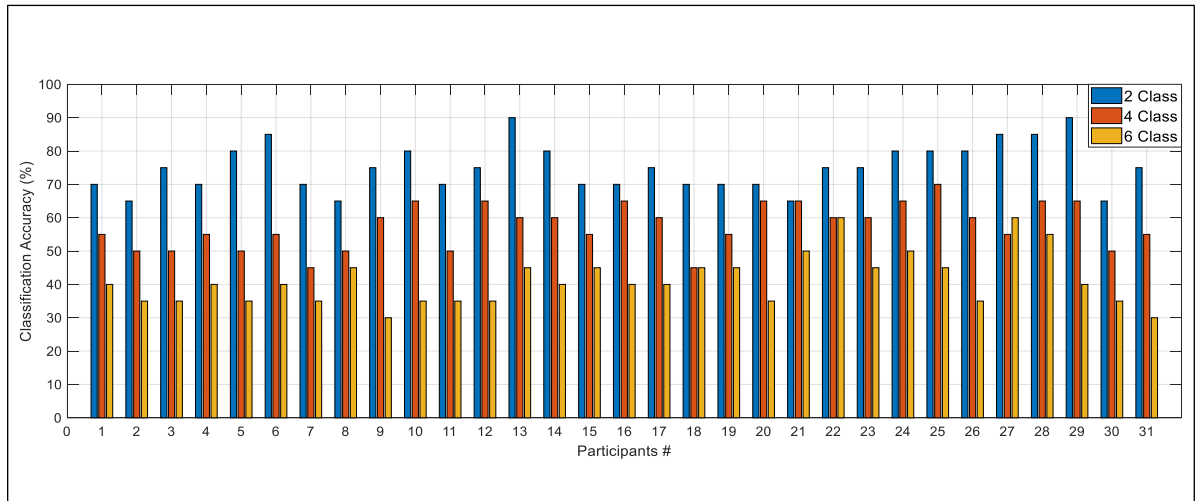


Figure 4.10: Subject dependent classification accuracies utilizing the spatiotemporal activation model with the proposed classification method regarding the 2, 4, and 6-class viewpoints.

We also classified the fNIR data of voluntary and imagery movements considering the time domain features (mean, slope, variance, and maximum). The HbO₂ and dHb signals of proposed ROI's were considered for these time domain feature extraction. The signal window for feature extraction was considered as 5-15s since this window is the mostly activated period (see **Figure 4.9**). The features of 2, 4, and 6-class data were used to train and test the LDA, kNN, SVM, and ANN classifiers. The classification accuracies of the 2, 4, and 6-class data by the four different classifiers are given in **Figure 4.11**, **Figure 4.12**, and **Figure 4.13**, respectively. The classification accuracies have been presented as the subject dependent approach.

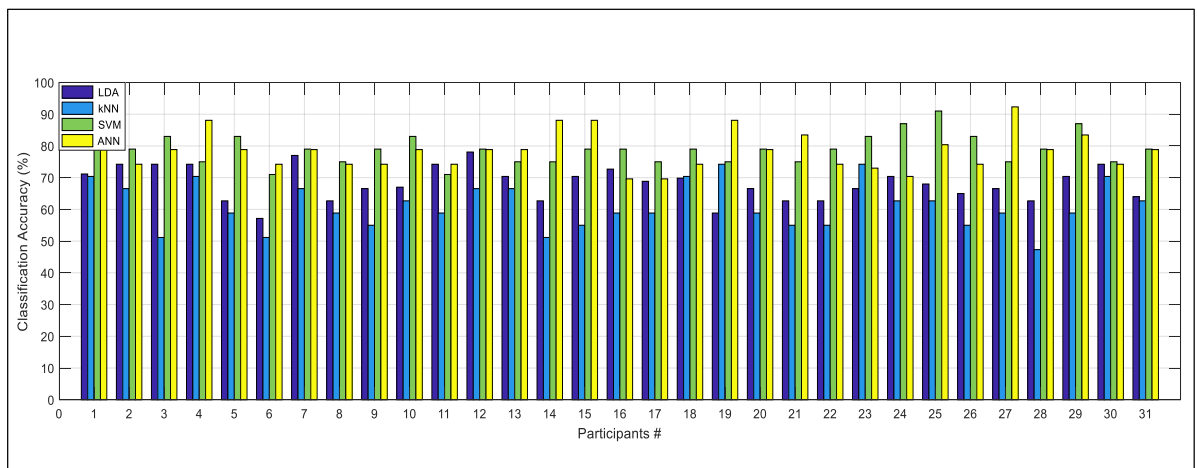


Figure 4.11: Subject dependent classification accuracies for 2-class data (iLH & iRH).

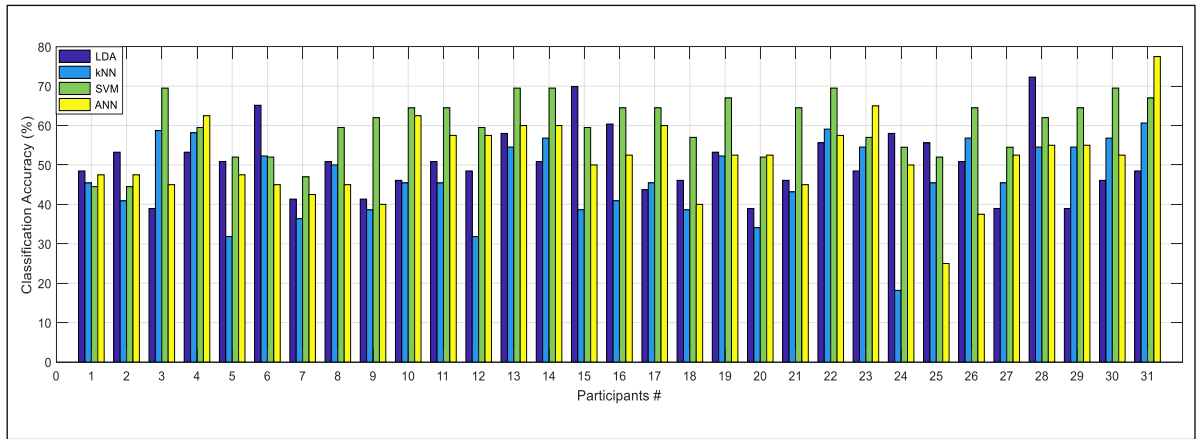


Figure 4.12: Subject dependent classification accuracies for 4-class data (iLH, iRH, iLF, & iRF).

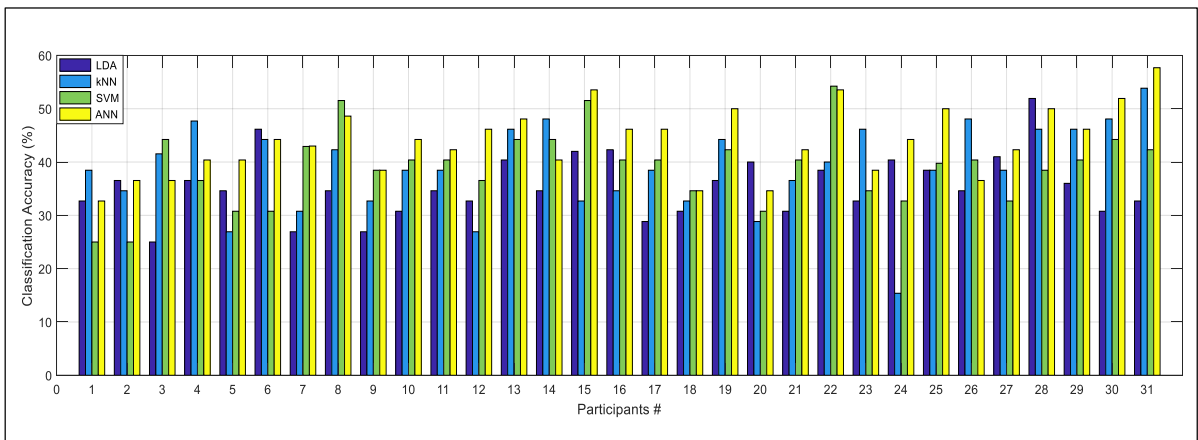


Figure 4.13: Subject dependent classification accuracies for 6-class data (LH, RH, iLH, iRH, iLF, & iRF).

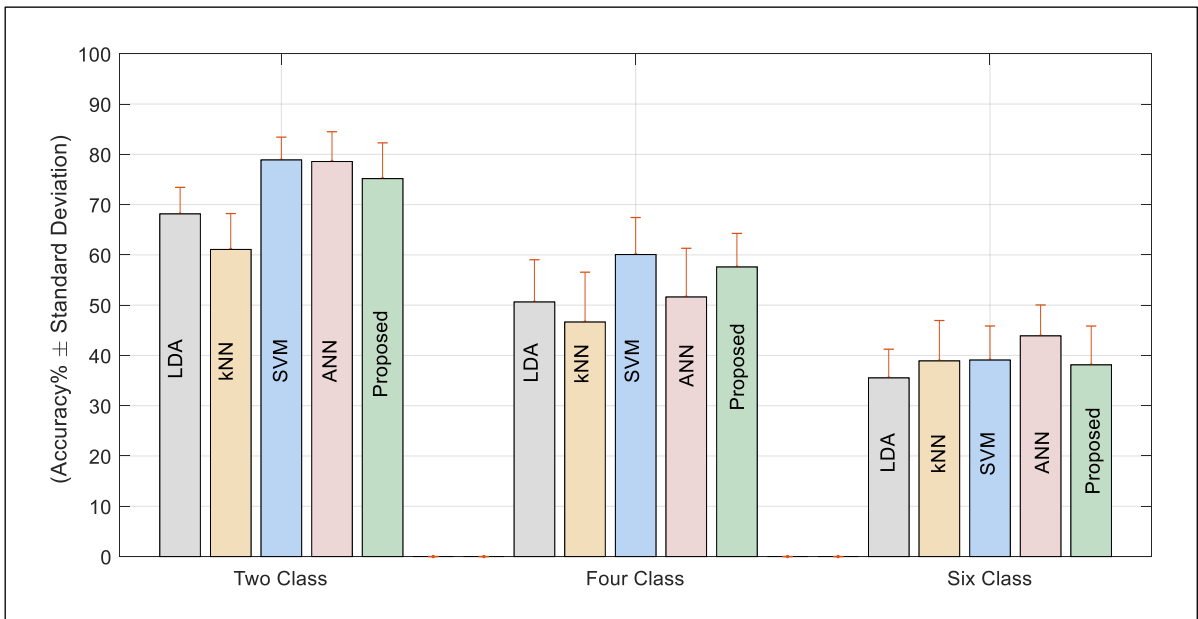


Figure 4.14: Average classification accuracies of the different classifiers for 2, 4, and 6-class fNIR data by the applied classifiers.

The average classification accuracies of the conventional classifiers along with the proposed activation model are given in **Figure 4.14**. From the results, we can see that the classification accuracies found by ANN and SVM are better than the kNN and LDA. Although LDA provides better results for 2 class problem, the accuracies are decreased with the increment of the number of the class, significantly. It can be happened due to its linear characteristics. In case of ANN and SVM, the nonlinear kernel function has been used and the accuracies are quite good for 4 and 6 class problem. On the other hand, the proposed classification method shows significant classification accuracies. Although it provides slightly lower classification accuracies than that of the ANN and SVM, the proposed method has no training stage like the conventional classifiers (ANN, SVM, kNN, and LDA). Therefore, by utilizing the proposed mechanism it is easier to implement a classifier to find the class of a signal from its activated region (spatial information) and the temporal pattern of the activation.

4.4 Conclusion

This research reports the localization of activations in prefrontal cortex due to voluntary and imagery movements and modeled the activations of different movement-related events with polynomial regression. This work opens the doorway to measure the voluntary and imagery movements from the prefrontal hemodynamics by fNIR modality. From the overall results of the proposed research work, we reveal that the upper limb movements (LH and RH) by voluntary and imagery movements are easily measurable from the prefrontal cortex due to their activation strength than the lower limb (iLF and iRF) activation. Although voluntary movements of lower limb (LF and RF) did not create activation significantly in the prefrontal cortex. This may be happened due to being the functional area of lower limb activities situated in the deep brain. The hemodynamic activations based on the concentration change in HbO₂ and dHb regarding the significant activities have been also modeled by the polynomial regression. These model equations will be helpful to assess the prefrontal hemodynamic activation pattern of the proposed movement-related events. In addition, this work proposes a classification technique utilizing the proposed

activation models to classify the fNIR data. We classified the 2, 4, and 6 class fNIR data including the voluntary and imagery tasks. The resulting classification accuracy of the proposed approach has been found convincing. The same signals were also classified by the conventional classifiers from the temporal features of the signals. From the comparisons of the classification accuracies by the conventional and the proposed approach, it has been found that the proposed method provides accuracies slightly lower than the ANN and SVM but it provides better result than that of the kNN and LDA. Another benefit of the application of the proposed method is its non-necessity of the training phase. The matrices of the polynomial coefficients (see (4.6) and (4.7)) regarding the propose activation models are used as the initial marker to compare a signal to find its class. So, it is easier to implement the proposed classification methods for the voluntary and imagery movement related task classification from the prefrontal hemodynamics. Since this work has found the very convincing classification accuracy from the prefrontal hemodynamics regarding voluntary and imagery movements, this result will be very helpful for implementing BCI for the paralyzed people as well as for those people has a major injury in their central lobe of the brain. Therefore, the proposed research work contributes significantly to model and classify the voluntary and imagery movements from the prefrontal hemodynamics.

As all the participants of this study were normal, the actual scenarios of the physically challenged or paralyzed persons were not taken into this research which can be considered as the limitation of this study. Nonetheless, this limitation may be a future direction of research to find the actual scenario of motor imagery (planning) activation in the prefrontal cortex regarding the physically challenged persons. In our future work, aforesaid undone work will be performed to present a comparative scenario of voluntary and imagery movement-related activations of the prefrontal cortex concerning both the normal and physically challenged persons.

CHAPTER 5

Predictive Modeling by CNN through fNIR and EEG Signals

5.1 Introduction

Functional brain imaging has been added a new dimension in biomedical engineering and explored the pathway to reach BCI. BCI contributes in various field of research in biomedical applications like prevention, detection, diagnosis, rehabilitation, and restoration [1]. In the field of BCI, EEG and MEG are two non-invasive modalities based on scalp electric potential. EEG has a very high temporal resolution (~1ms) with poor spatial resolution (EEG: 5 to 9 cm) [2]. Though MEG has both high temporal (~1ms) and spatial resolution (<1cm), it is not suitable for BCI because of its noise sensitivity and heavy weight [3]. Based on the hemodynamics, fMRI provides an excellent spatial resolution (3~6mm) but its temporal resolution is poor (1~3 sec). Nonetheless, due to its very high cost, motion sensitivity, and being bulky it is also not suitable for BCI [4]-[6]. To optimize the aforementioned limitations and requirements, it is a high demand for a new modality. fNIR is such a neuroimaging modality discovered in 1977 by Jöbsis [7]. The researchers in [8-10] reported that NIR range enables real-time non-invasive detection of hemoglobin oxygenation using fNIR. The fNIR modality provides a very good spatial resolution (~1-1.5cm), moderate temporal resolution (up to 100Hz), portability to use, low cost, the high value of the SNR, less motion artifact compared to fMRI, MEG, EEG, and PET, etc. [4]. Furthermore, fNIR is not as physically confining as fMRI and it allows movement during imaging. Recent publications [11, 12] demonstrated that the results of fNIR are comparable to fMRI and reliable for cortical activations measurement. Since, fNIR provides finer spatial resolution and EEG provides finer temporal resolution, combined information of fNIR and EEG is getting the most attention for the recent researches [13-18] in the field of neuroimaging and BCI.

Millions of people in the world are in different form of disability [19], whereas the brain of the most of these disabled persons work partially or completely. In this situation, a finer BCI system is a hope to provide to provide them easier life by operating different devices by brain command. There are various proposals for BCI

using single modality EEG or fNIR. One of the main limitations of the single modality based BCI is lower accuracy (less than 50%) for multiple motor imagery tasks classifications. Therefore, to implement suitable BCI, multimodal neuroimaging methods are proposed. Some recent research works [13, 14, 18] based on imagery movement-related tasks classification have been proposed by combining fNIR & EEG signals for BCI implementation. It has been revealed in [13-18] that the classification efficiency of combining fNIR & EEG is better than that of the individual modality. These multimodal proposals used conventional shallow machine learning algorithm to classify the multiple class problems. As the result, the achieved classification accuracies so far are still lower than the expectations. To achieve higher accuracy, several proposals [20-23] have been approached with convolutional neural network (CNN) which is a deep neural network to achieve the higher classification accuracy than that of the conventional shallow networks. From the aforementioned issues, two significant limitations of the existing works are found:

- Most of the existing BCI's are designed based on single modality which limits classification accuracies for multiple classes due to spatiotemporal resolution.
- No significant research work has been accomplished for deep neural network based BCI from the combination of fNIR and EEG signal.

To overcome these challenges, this proposed work scopes to design multimodal BCI and hence the objectives of this research work are to develop a CNN-based predictive model for multiclass BCI from fNIR and EEG signals.

The purpose of this work is to develop an effective BCI model to classify the brain signals (fNIR and EEG) regarding the voluntary and imagery movements. For achieving the high classification accuracy from the developed BCI system, CNN has been used to extract the features automatically from the multiple channel fNIR and EEG signals instead of the manual feature selection. In this work, eight different movement-related stimuli (four voluntary and four imagery movements of hands and feet) have been considered. The multiple channel fNIR and EEG signals are used to prepare functional neuroimages to train and test the performance of the proposed BCI system. In addition, the proposed procedure is applied to prepare neuroimages from the individual modality (fNIR and EEG) to train and test the performance of the CNN based BCI system. The results reveal that the combined-modality approach

of fNIR and EEG provides the improved classification accuracy than the individual one. The conventional feature extraction methods are also deployed in the previous chapter. We expect that the proposed CNN based predictive model will outperform the conventional methods in terms of the classification accuracy.

5.2 Materials and Methods

5.2.1 Data Acquisition Protocol

Eight different tasks were considered for neural stimulation. Every participant engaged in this research work performed four voluntary and four imagery tasks. Generally movements are mostly conducted by hands and feet. The participants were asked to perform movements by hands and feet by means of voluntary and imagery manner. The subjects were verbally informed and practiced the protocol of the data acquisition before actual data acquisition. The subjects lifted their left hand, right hand, left foot, and right foot, sequentially. For the proposed neural stimulation, the task was performed during 10 second with 20 second resting period. Therefore, the scheduling of the proposed data acquisition protocol can be presented by **Figure 5.1**. In one session this unit protocol was performed four times by a participant. After every session, each participant took rest at least five minutes. Eventually, every participant performed 40 trials for each movement related task. A graphical protocol aiding software was used for this research work that instructed graphically to perform the tasks according to the schedule designed about which we have already discussed in previous chapter. In this program, there are five different tasks those are movements of the hands, feet (left & right), and rest. Eventually, eight different tasks have been considered for analysis: voluntary left hand (LH), right hand (RH), left foot (LF), right foot (RF) and imagery left hand (iLH), right hand (iRH), left foot (iLF), and right foot (iRF).

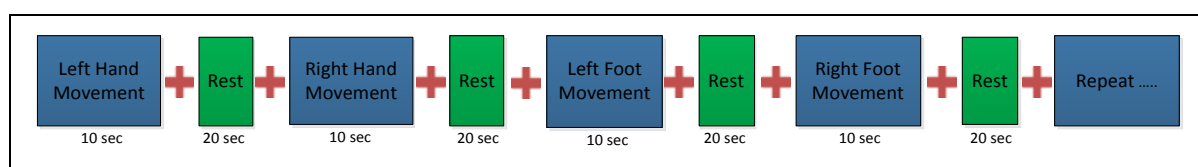


Figure 5.1: Time schedule of data acquisition protocol for each participant regarding both the voluntary and imagery movements. This is a unit task performing schedule that was repeated four times in each session to complete 40 individual trials of every task.

5.2.2 Data Acquisition

Fifteen right handed male subjects (age range=22 to 26) participated in this data combined fNIR-EEG data acquisition procedure. No participant had a history of the psychiatric, neurological, or visual disorder. Plus, no participant was reported to have any pain in their both hands and feet. The verbal consents of the participants were taken prior to the data acquisition as the rule of the university. All data acquisition procedures were completed in the Neuroimaging Laboratory of the Biomedical Engineering department of KUET obeying the declaration of Helsinki [24].

For this work, a 16 channel continuous-wave fNIR system (model: Biopac 1200 fNIR imager) and 9-channel EEG device (model B-Alert X-10) were used. The 9-channel electrode system of B-alert X-10 device has been illustrated in **Figure 5.2**. The data acquisition wireless device is also given in the figure. It covers the frontal, central, and parietal lobe with 9 channels so far. It is a wireless system to transmit the data. The data is logged by Acknowledge Software (version 4.4).

Utilizing both fNIR and EEG device, the prefrontal, frontal, and central part of the brain are covered. The hemodynamic signals from the prefrontal cortex were acquired by the fNIR device and the EEG signals of the frontal and central part of the brain were captured by the 9 channel EEG device. The optodes of fNIR devices and the electrode of B-Alert system were placed as the positions indicted by **Figure 5.3**. The COBI studio and Acknowledge software were used to log the combined fNIR-EEG signal. Although there is a time gap between the starting of the EEG and fNIR signal acquisition software, it has been corrected by reverse counting approach. In practice the illustration of concurrent fNIR and EEG data acquisition from a participant has been given in **Figure 5.4**. From the figure, the usage of the fNIR devices and EEG system are clearly observable.

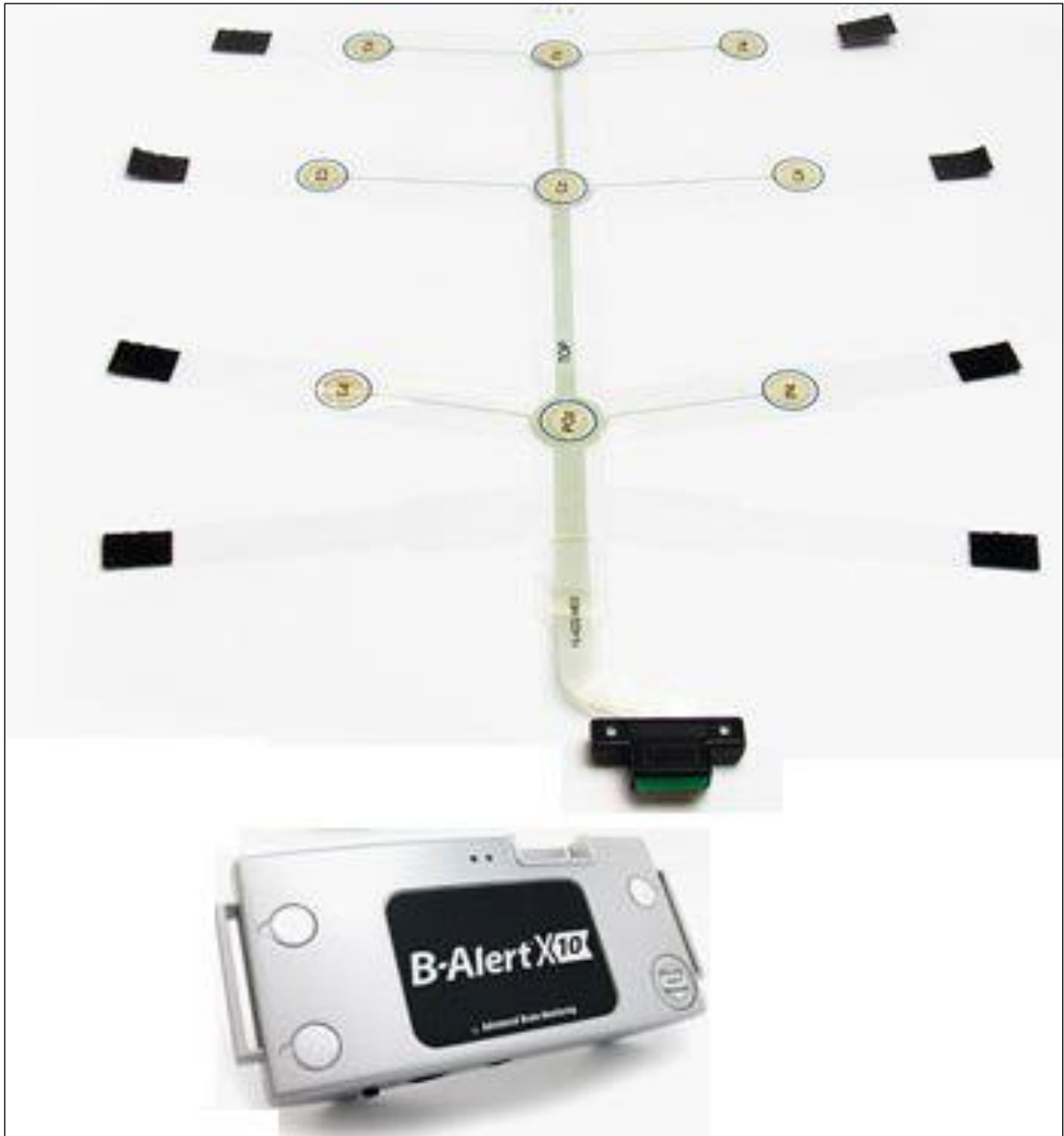
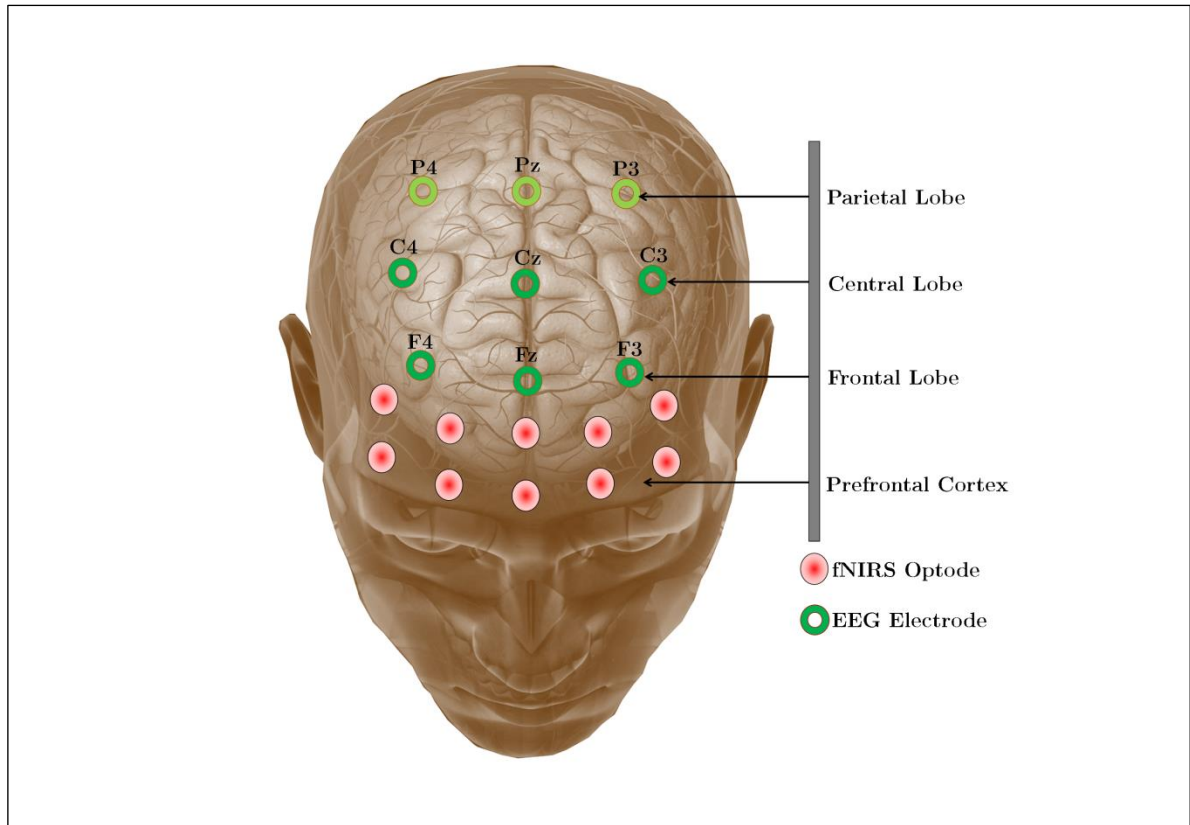


Figure 5.2: The electrodes and the data acquisition module of B-Alert X-10 wireless EEG system.



5.3 Figure: The combined fNIR-EEG sensor positions on the scalp and prefrontal cortex. The data of parietal lobe are acquired through the main data acquisition period but excluded for proposed offline processing.



Figure 5.4: Data acquisition of voluntary and imagery movements by concurrent fNIR and EEG modalities.

5.2.3 Methods

For multimodal signals fusion between fNIR and EEG, at first, all raw EEG signals are filtered by a 50Hz notch filter to remove power line noise. After that bandpass, elliptical filters are used to separate the strong band power from 1-60 Hz. The order of filter are taken as optimal selection considering passband range (1 to 60 Hz), stopband range (0 to 0.5 and 60.5 to ∞ Hz), the sampling frequency (256 Hz),

passband ripple (0.1), and stopband ripple (30) [25]. Since neural activities of imagery and voluntary movements are connected with the frontal and central part of the brain, only frontal three channels, and central three channels are taken for further processing. The most dominant features are included in the alpha, beta, and total band power of the EEG signal in case of imagery and voluntary movements [11, 26]). As a result, the relative powers of the alpha and beta band from the six channels are extracted by short-term Fourier transform (time period is 0.5 sec with 50% overlapping containing 128 samples). The average power of these prominent bands will be varied according to the tasks of voluntary and imagery movements those are fed into the CNN [27] classifier as 12 column feature vector combining with fNIR temporal samples of 16 channel. Finally, we get data matrix of 120×28 size. In our proposed method, neuroimages have been prepared by 16 column fNIR data (both HbO_2 and dHb) with 6 column EEG features.

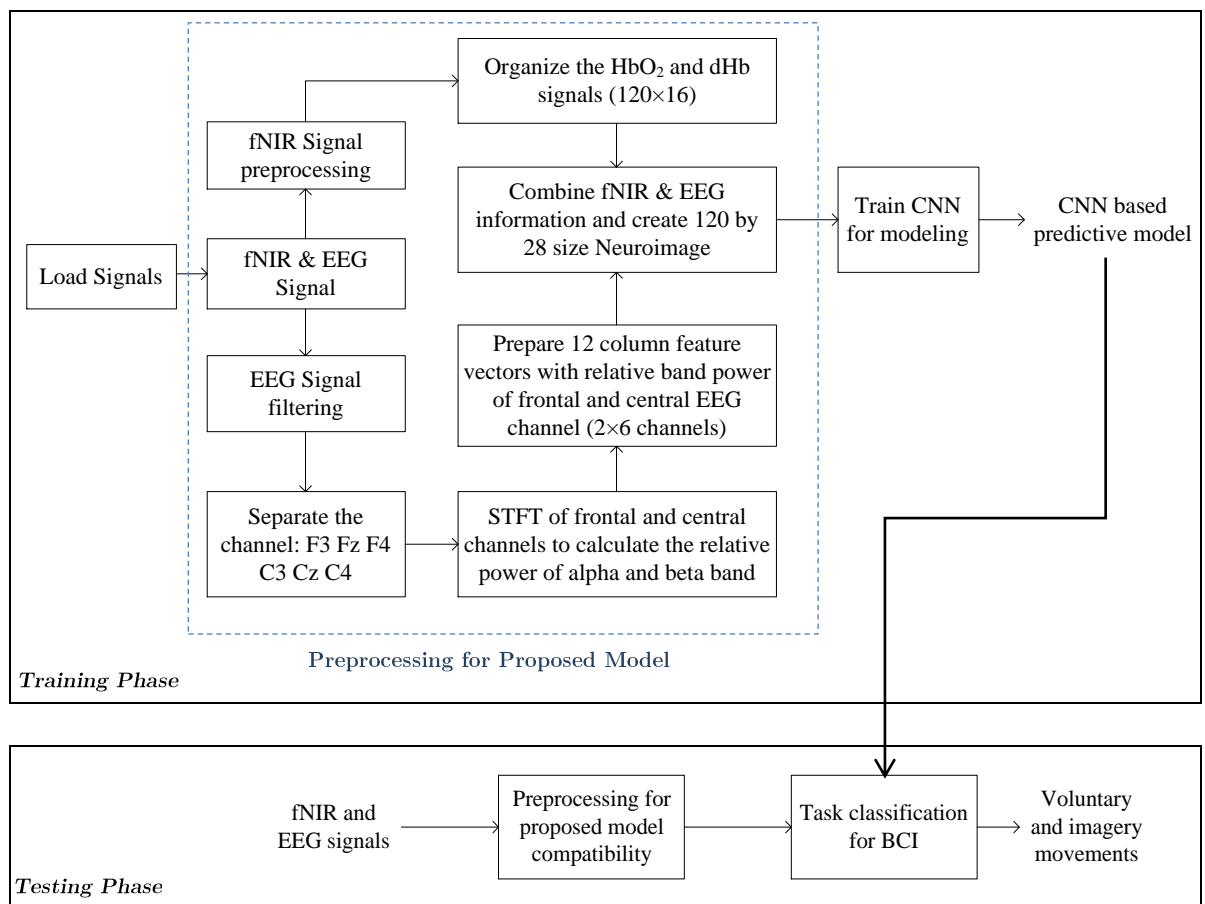


Figure 5.5: The training and testing phase of CNN based predictive model to classify the voluntary and imagery tasks for BCI.

These images of combined information of fNIR and EEG are fed to CNN to train the network that can be able to model itself as a movement related task classifier. This multimodal neuro-image based predictive model by CNN will be capable to provide highly efficient BCI. This complex methodology with prominent steps can be explained briefly by the following block diagram given in **Figure 5.5**.

5.3 Results and Discussions

Since the preprocessing results of the fNIR signals have been discussed in the previous chapters with clarified illustrations, in this chapter, some results of prominent preprocessing steps of EEG signal has been illustrated. The effect of notch filter on raw EEG signal has been presented in **Figure 5.6**. In addition, the elliptical filtering effects and eye blink removal steps are also given in this figure. Raw EEG signal is filtered by 50 Hz notch filter to remove the power line noises from the signal. After that, a third order elliptical filter has been used to filter up to 45 Hz EEG signal. This signal is still contaminated with the eye blinking effect. This effect has been removed using the Matlab based toolbox, EWICA. All the corresponding results of the preprocessing steps have been given in a chronological order in **Figure 5.6**. According to the assumption of the proposed work, with the variation of the task (either voluntary or imagery tasks) the band power of alpha and beta band will be changed. A grand variation has been estimated between left and right hand imagery movements using PSD and the outcomes of this assumption have been given in **Figure 5.7**. From the results, we can see that the variations are observable both in frontal and central lobe of the brain with a similar pattern.

It has already been claimed that we considered the central and frontal EEG channel. This is because the functional changes occur in the central lobe mostly, but the frontal lobes become also activated due to voluntary and imagery movement related tasks. For the justification, we have added the activation level of the different positions of the brain concerning frontal, central, and parietal lobe of the brain as topoplot. The topoplots are presented in **Table 5.1**. The topoplots are prepared from the average activations of five randomly chosen subjects. A Matlab based free toolbox [28] has been utilized to prepare the graphical topoplots, which is solely designed for the 9-channel EEG data of B-Alert wireless devices.

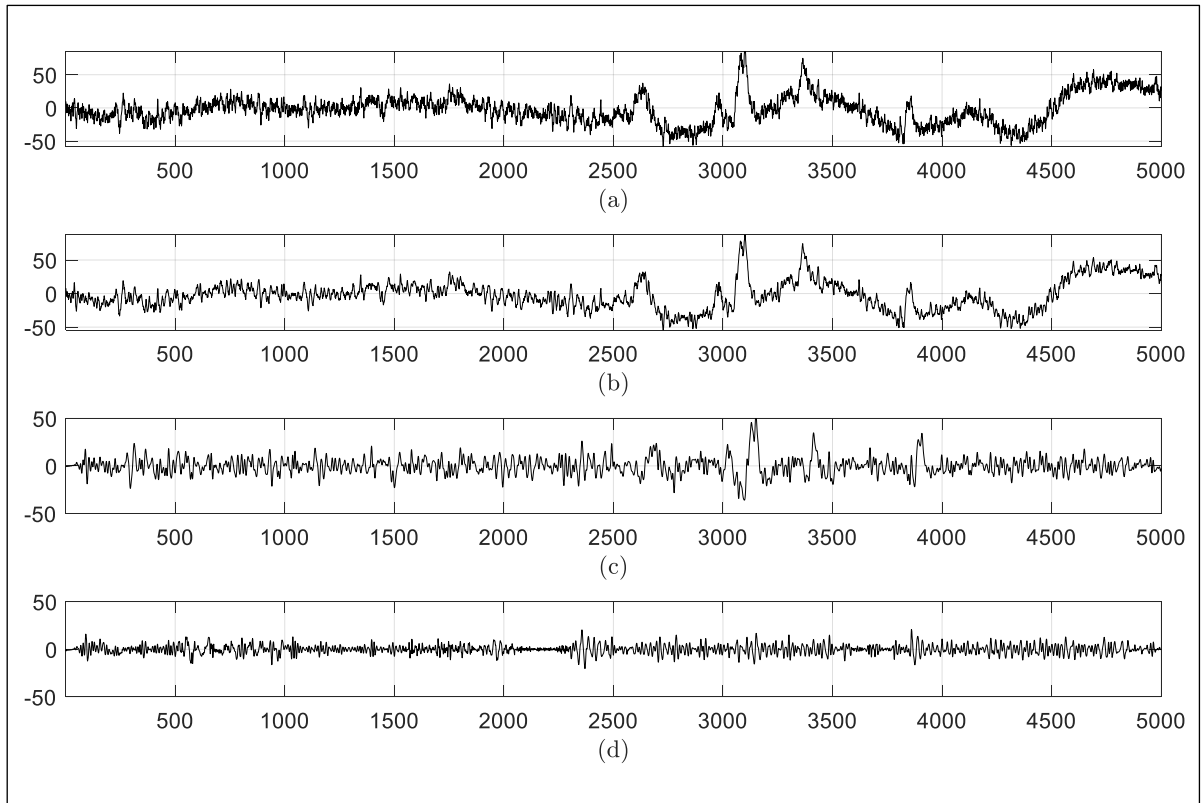


Figure 5.6: Step by step EEG signal pre-processing: (a) Raw EEG signal of a single channel, (b) EEG signal after removing 50 Hz power line noise, (c) Filtered EEG signal upto 45 Hz by third order elliptical filter, and (d) Eye-blink and EOG artifact free EEG signal which is filtered by the EWCA toolbox.

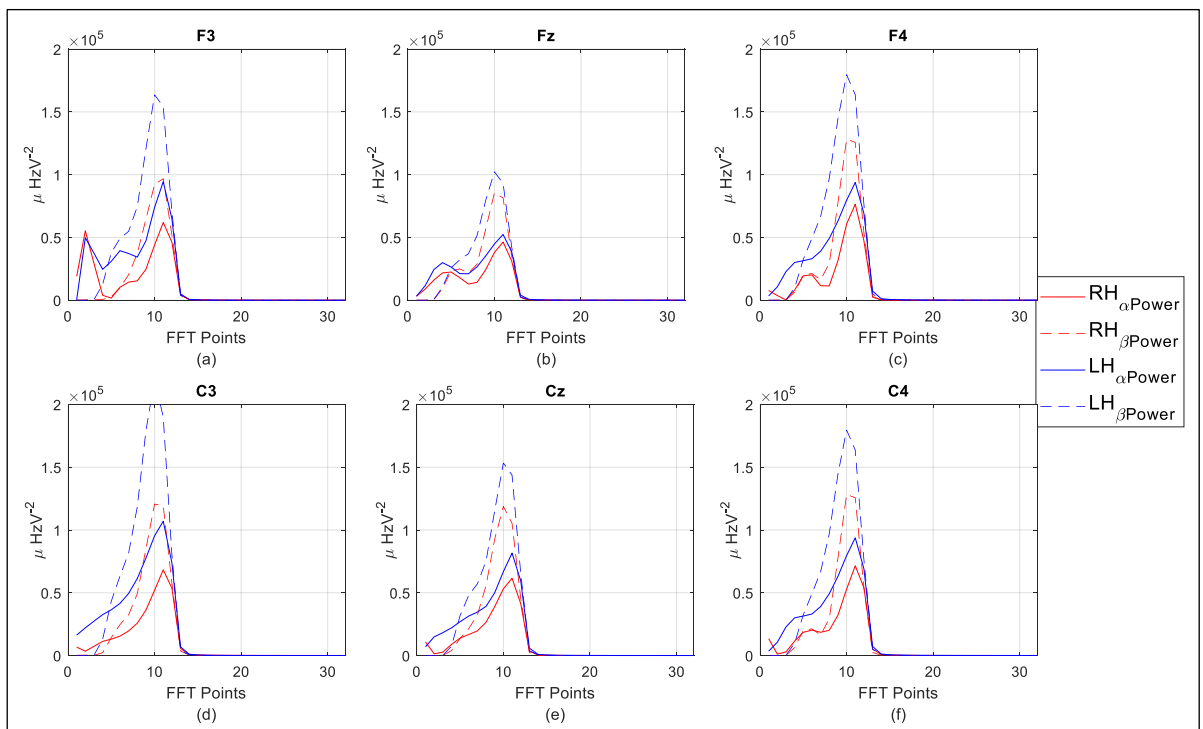
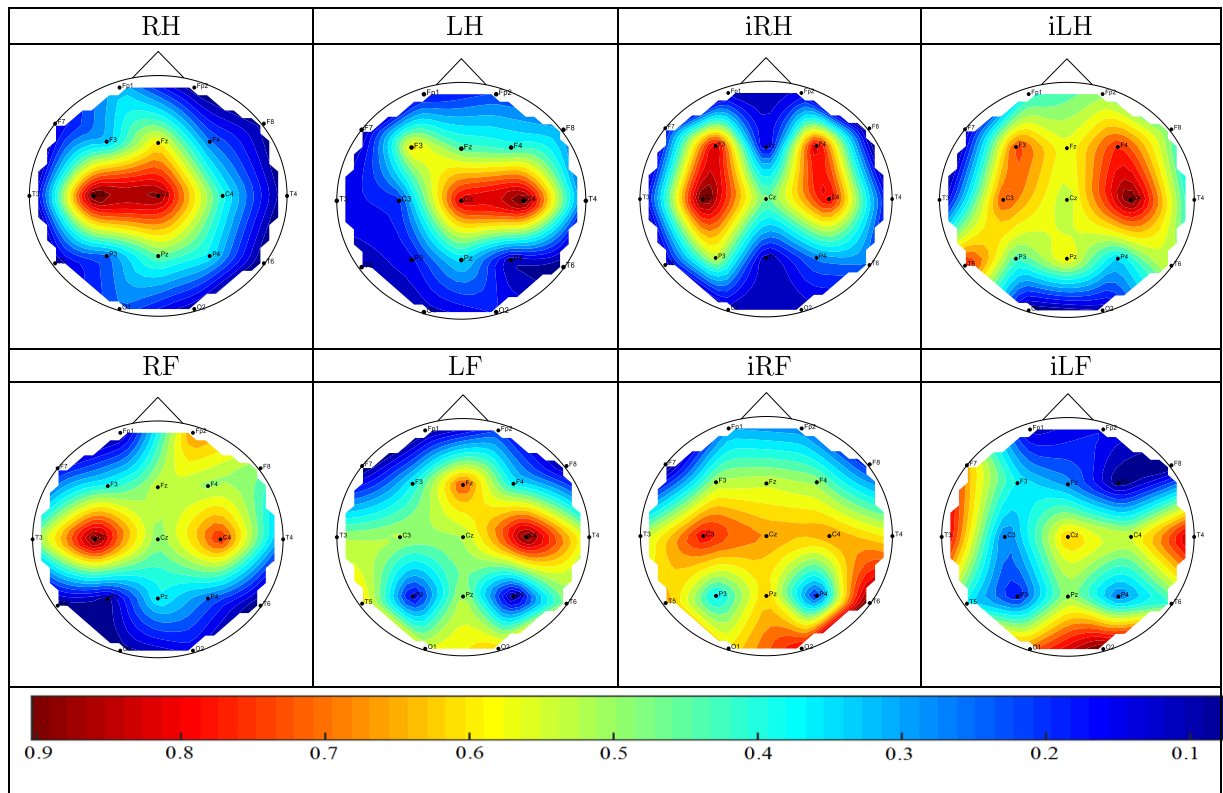


Figure 5.7: The power of alpha and beta band of left and right hand imagery movement.

Table 5.1: The average neural activations regarding different stimuli. The activation was calculated based on the relative power spectral density of the channels.



From the topoplots we get that the voluntary movements of hands and feet create significant activations in the central lobe. On the other hand, due to imagery movements, both the frontal and central lobes become activated. One thing is noticeable for the imagery feet movements that the impact of the activation is slightly lower than that of the imagery hand movements. In addition, the patterns are also irregular compared to the movements of the voluntary feet movements. In most of the cases, the parietal lobe was inactive and that is why the information of the parietal lobe is excluded in the functional neuro-image construction.

Consequently, according to the proposal the fNIR and EEG signals have been combined obeying the rule proposed in the previous chapter. It should be mentioned that with the combined fNIR-EEG based image, we also used only the fNIR data (HbO₂ and dHb) to produce the neuroimages for the training of the CNN. It is performed to show that the difference in the classification accuracy between the single fNIR modality and the combined modality approach. The neuroimages regarding the single and bimodal data of eight different class stimuli have been

presented by **Table 5.2** and **Table 5.3**, respectively. The images are prepared on the basis of their normalized value. Furthermore, these images are RGB color image those are prepared to feed the CNN. The image size is $(384 \times 384 \times 3)$.

Table 5.2: Neuroimages from the temporal HbO₂ and dHb fNIR data of 10 sec task plus 20 sec activation. Here, there are the images of eight types of tasks with 6 trials of each task.

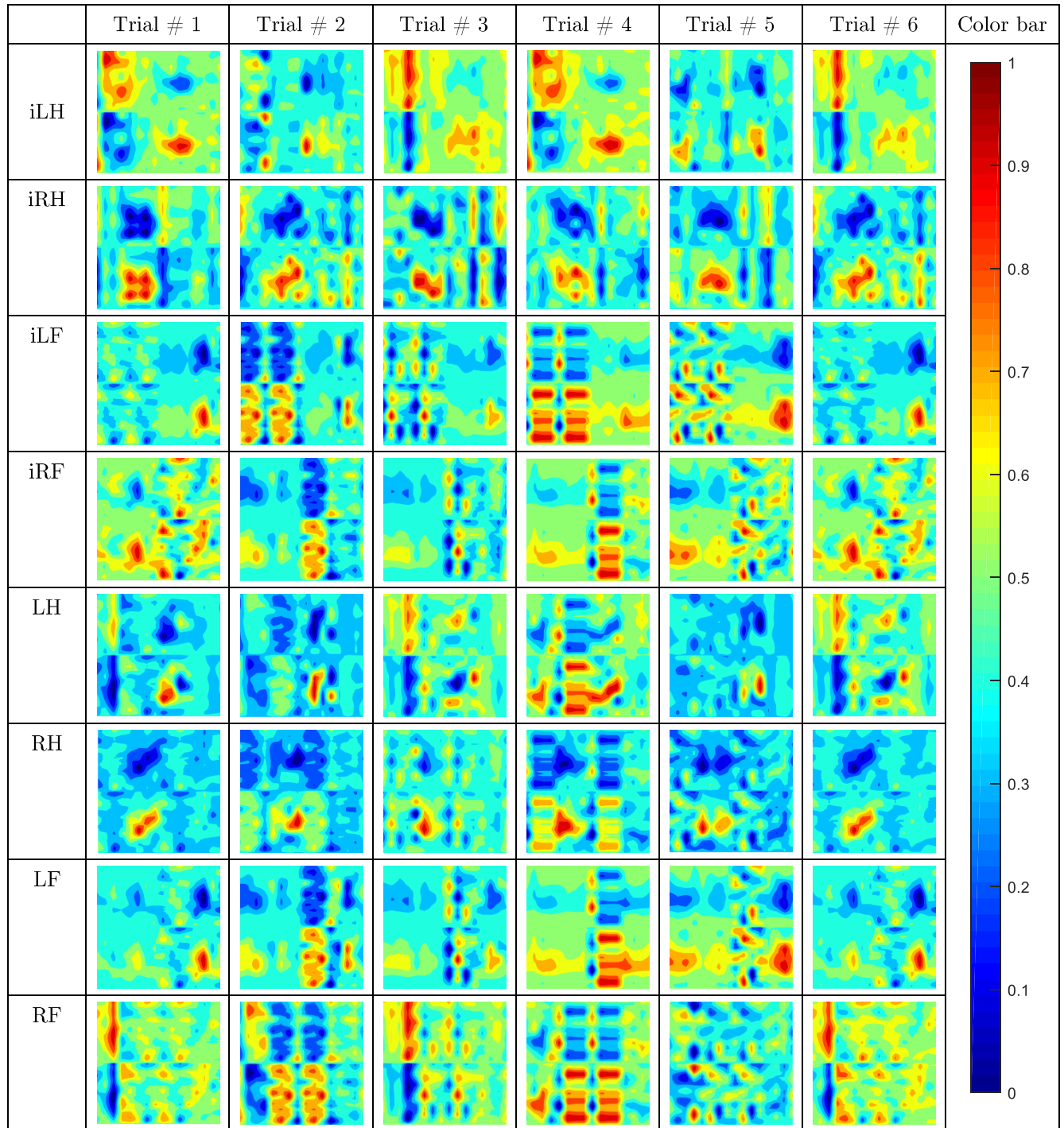
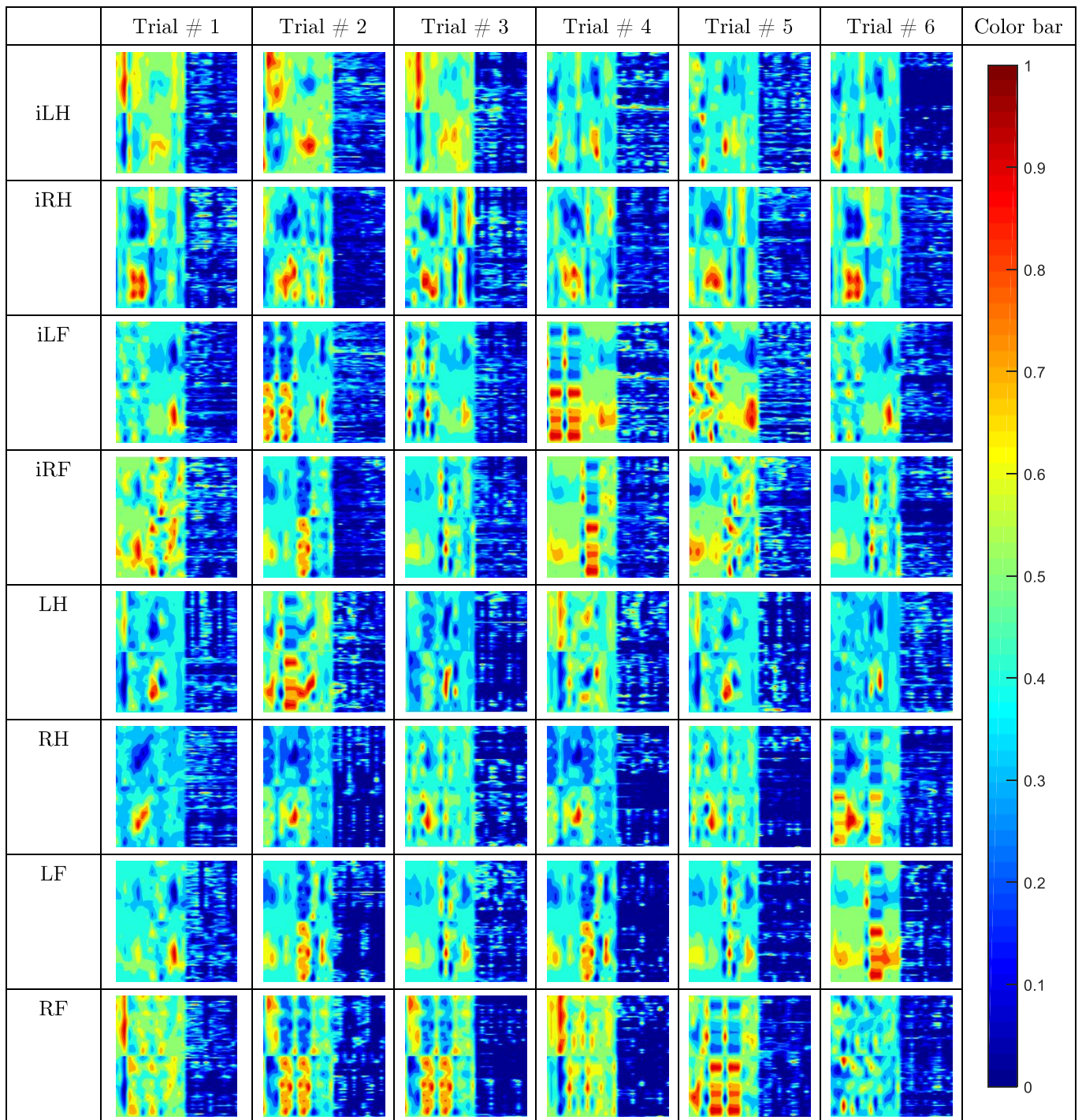


Table 5.3: Neuroimages from the combined fNIR and EEG data of 10 sec task plus 20 sec activation.



These images are sequentially fed to the CNN for automatic feature extraction and to train the predictive model for further classification. The typical CNN structure and the outcome features of the fed images with each convolution layer have been presented in **Figure 5.8** and **Figure 5.9**, respectively.

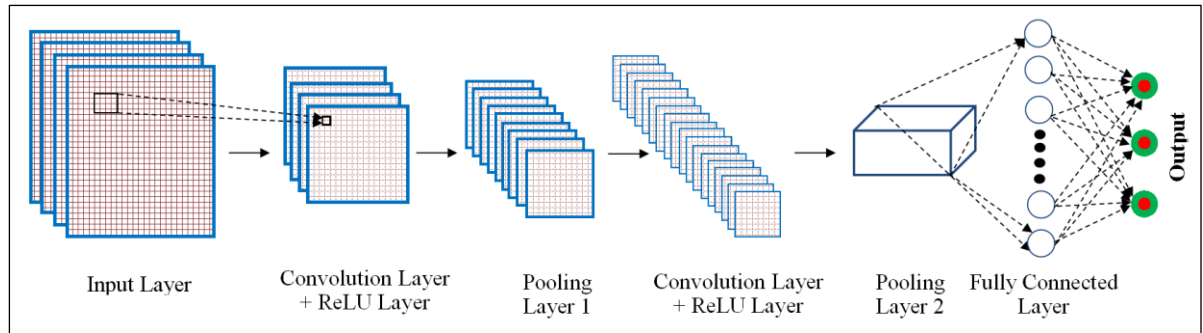


Figure 5.8: The general structure of a CNN based classifier.

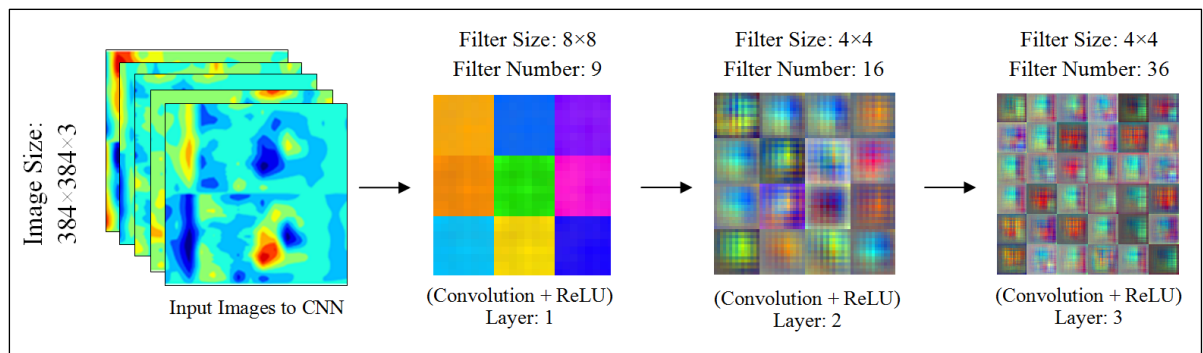


Figure 5.9: The features of the input images with the changes of layers of the CNN based classifiers.

The CNN structure of the proposed work has been given in Figure 5.10. This is a demo code of the CNN structure of the proposed work where the filter size and numbers were changed to get the optimum classification accuracy for all conditions. Here, the basic structure of the designed CNN network has been shown with its different parameter considerations. The architecture information regarding the proposed CNN model of this work are summarized in **Table 5.4**. With three convolutional layers (given in **Figure 5.9** with detail information), there are 15 layers in the proposed CNN model that includes three convolutional, two maxpooling, three batch normalization, and four/six/eight fully connected layers. In the case of four, six, and eight class problems, the fully connected layers are set to four, six, and eight, respectively. As explained earlier, the input image size is $384 \times 384 \times 3$, which indicates the image matrix size 384×384 with its 3-dimensional color information. The filter kernel was used as 8×8 , 4×4 , and 4×4 for the 1st, 2nd, and 3rd convolutional layers, respectively meanwhile the filter number was 9, 16, and 16, respectively. We have used stride [1 1] for the convolutional layers and [2 2] for maxpooling layers. The convolution layers and its kernel and filter numbers of this proposed CNN model are given in **Figure 5.9** along with the feature maps for the 4-class problem of a

typical subject. : The proposed CNN model was trained based on some initial considerations about different parameters, which are defined in **Table 5.5**. The loss function was calculated from the cross-entropy in the softmax layer. On the other hand, the training and testing data ration was considered 4:1. The classification accuracy was performed based on the 5-fold cross-validation technique. The 25% training data was used for validation. The training and testing of the proposed model were conducted as the subject-dependent approach. Eventually, the data of 15 participants were separately used for training and testing. The classification accuracy was conducted for 4, 6, and 8 class where the class level was set as 4 class: [LH, RH, iLH, and iRH], 6 class:[LH, RH, iLH, iRH, iLF, and iRF], and 8 class [LH, RH, LF, RF, iLH, iRH, iLF, and iRF].

Table 5.4: The details about the layers of the proposed CNN structure applied in this research.

Layers	Type	Description
0-1	Image Input Layer	384×384×3
1-2	Convolution Layer 1	Filter size=[8,8]; Number of Channels=3; Number of Filters=9; Padding Size=[3,4,3,4]; Stride=[1,1]
2-3	Batch Normalization Layer	
3-4	ReLU Layer	
4-5	Maxpooling Layer	Pool Size=[2,2]; Stride= [2,2]
5-6	Convolution Layer 2	Filter size=[4,4]; Number of Channels=9; Number of Filters=16; Padding Size=[1,2,1,2]; Stride=[1,1]
6-7	Batch Normalization Layer	
7-8	ReLU Layer	
8-9	Maxpooling Layer	Pool Size=[2,2]; Stride= [2,2]
9-10	Convolution Layer 3	Filter size=[4,4]; Number of Channels=16; Number of Filters=36; Padding Size=[1,2,1,2]; Stride=[1,1]
10-11	Batch Normalization Layer	
11-12	ReLU Layer	
12-13	Fully Connected Layer	Output Size=4/6/8
13-14	Softmax Layer	
14-15	Classification Output Layer	Output Size=4/6/8; Loss Function=Crossentropy

Table 5.5: Parameters considerations in the proposed CNN based model training.

Parameter Name	Consideration	Parameter Name	Consideration
Activation Function	Sigmoid	Maximum Epoch	20
Momentum	0.90	Mini Batch Size	128
Initial Learning Rate	0.01	Verbose Frequency	50
L_2 Regularization	1.00×10^{-4}	Validation Frequency	4
Gradient threshold method	L2 norm	Validation Patience	5

The trained model was constructed for 4-, 6-, and 8-class. The training and validation accuracy with respect to the iteration of 4-, 6-, and 8-class problems are given in **Figure 5.10**, **Figure 5.11**, and **Figure 5.12**, respectively. The loss reduction during training and validation of the proposed CNN models is also given in the figures. The training and validation accuracy of the proposed CNN model are found best in case of 4-class problem. On the other hand, the validation accuracy was slightly inferior in the case of 6 and 8 class.

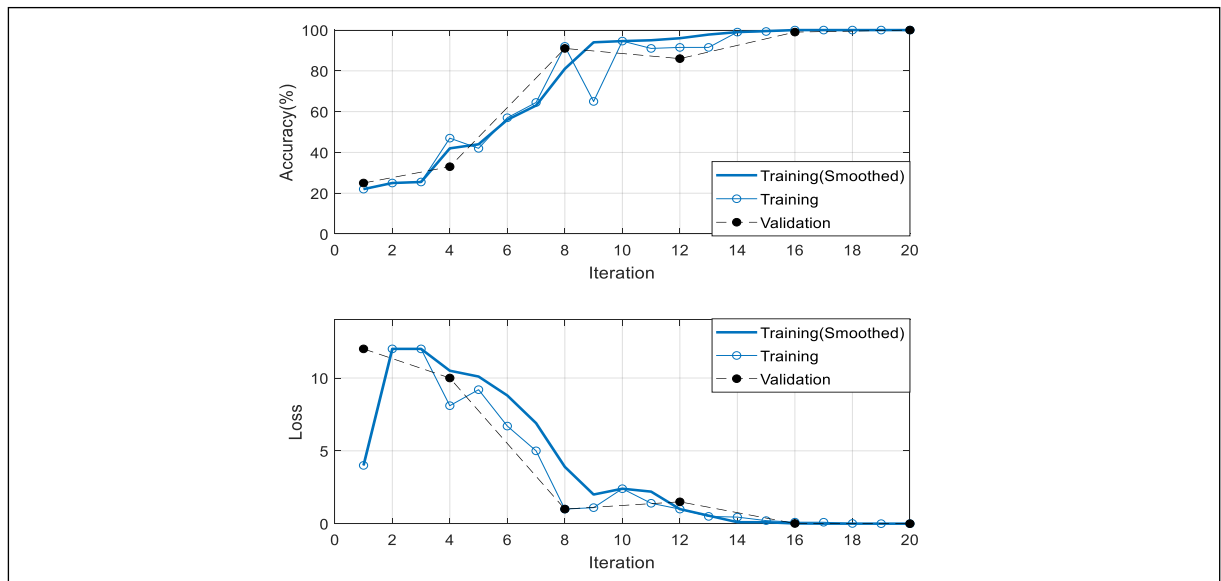


Figure 5.10: The training and validation accuracy with loss performances with respect to the epoch iterations for 4-class problem.

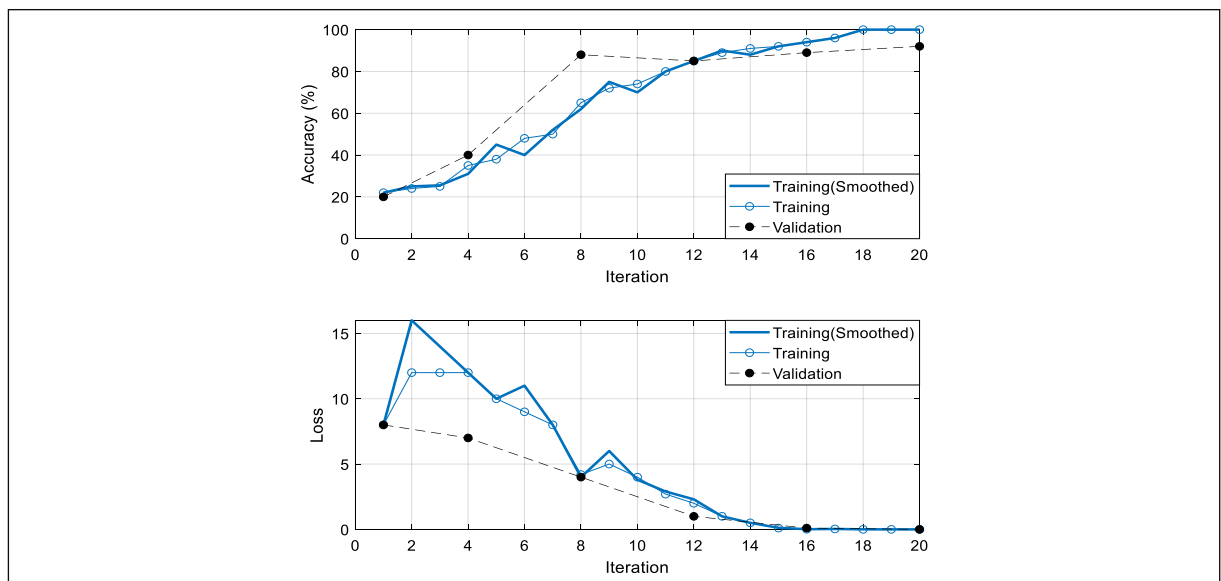


Figure 5.11: The training and validation accuracy with loss performances with respect to the epoch iterations for 6-class problem.

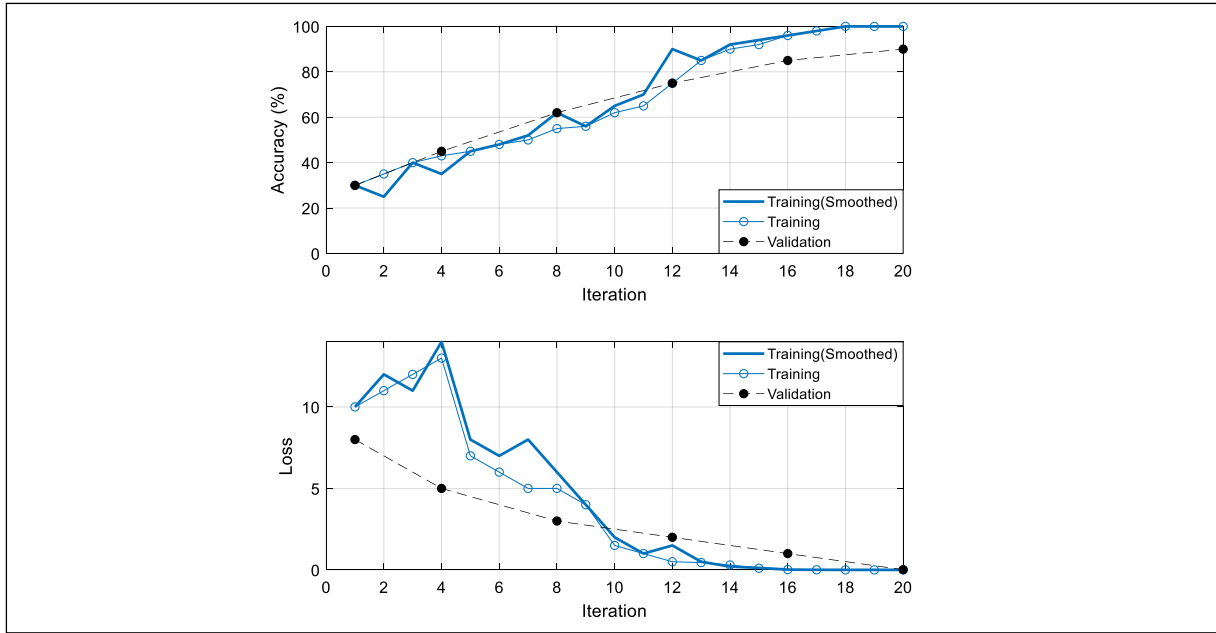


Figure 5.12: The training and validation accuracy with loss performances with respect to the epoch iterations for 8-class problem.

These results are found for subject 1 while the models were trained by combined fNIR and EEG data. We have applied two different approaches to find the classification accuracy: one is based on fNIR data only and the other is based on the combined information of fNIR and EEG data. The results of 15 participants are given in **Table 5.6** and **Table 5.7**, respectively. In addition, according to the proposition and scope of this work, the conventional classification methods such as LDA and SVM were also applied to check their performance. The extracted features of the fNIR data and the combined fNIR and EEG data were classified utilizing the SVM and LDA method and the regarding results are also given in **Table 5.6** and **Table 5.7**, respectively.

From the result, we get that the combined information provides us greater classification accuracy. For 4-, 6-, and 8-class problems, the classification accuracies are significantly improved by 9%, 11%, and 17% on average by the combined fNIR-EEG information in case of the CNN. On the other hand, the improvement in the classification accuracy occurred 10%, 8%, and 8% for SVM and 7%, 4%, and 5% for LDA. In the case of the conventional classifiers, the performances for the 6- and 8-class are not convincing at all and that is why, the choice of CNN is inevitable. The average classification performance of SVM, LDA, and the proposed CNN model for single and bimodal data are presented in **Figure 5.13** and **Figure 5.14**, respectively

to reflect the importance of utilizing the combined information of fNIR and EEG signal as well as choosing CNN as a classifier. The results claim that for 8-class problem classification, CNN exceptionally plays a significant role to achieve the expected BCI goal. In addition, the combination of the EEG information with the fNIR signal provides an excellent increment in the classification performances. The result proves that combined information of fNIR and EEG outperforms the information regarding the fNIR signal alone. In addition, the classification accuracy has been achieved $90 \pm 4.54\%$, $82 \pm 5.12\%$, and $72 \pm 4.34\%$ for 4-, 6-, and 8-class problems, respectively, which is too convincing for the BCI implementation.

Although there is numerous research work on motor imagery signal classification, their data acquisition protocol, devices, participants, and modalities are different from each other. Therefore, to compare them directly are difficult in the scientific aspect. Although some research works have existed that deploys 4-class motor imagery EEG or fNIR signal classification, there is only one work [29] that presents both 4-class and 8-class BCI for robot hand control. Since the main objective of all these research works is to implement BCI, a general comparison regarding their protocols, methods, and performances could be a nice presentation to observe the overall concept about the trends of the multiple-class BCI implementation through fNIR, EEG or combined fNIR & EEG. Such a comparison of 4-class and 8-class BCI of the proposed method with the others has been presented in **Table 5.8**. From the performance of the proposed method it is clear that in the process of improvement trending in the research of BCI, our proposed bimodal approach outperforms the existing previous works.

Table 5.6: The classification accuracy of the SVM, LDA, and the proposed model with the fNIR data only.

Participant #	4-class			6-class			8-class		
	<i>SVM</i>	<i>LDA</i>	<i>Proposed CNN</i>	<i>SVM</i>	<i>LDA</i>	<i>Proposed CNN</i>	<i>SVM</i>	<i>LDA</i>	<i>Proposed CNN</i>
1	60%	76%	82%	52%	61%	74%	48%	45%	55%
2	63%	66%	78%	53%	59%	71%	45%	48%	50%
3	68%	66%	80%	57%	53%	77%	52%	43%	50%
4	70%	74%	84%	60%	63%	77%	58%	54%	55%
5	65%	70%	85%	53%	54%	67%	37%	39%	65%
6	68%	69%	76%	61%	58%	71%	54%	47%	60%
7	64%	72%	81%	56%	67%	75%	41%	50%	60%
8	69%	67%	78%	64%	58%	61%	52%	56%	55%
9	66%	70%	89%	54%	53%	78%	43%	35%	50%
10	65%	68%	78%	59%	62%	65%	48%	48%	55%
11	72%	66%	78%	59%	60%	62%	48%	58%	45%
12	68%	64%	82%	56%	59%	71%	37%	48%	50%
13	73%	75%	84%	65%	66%	71%	56%	52%	60%
14	70%	74%	90%	62%	62%	74%	58%	51%	65%
15	74%	72%	75%	65%	64%	64%	43%	50%	50%
Average \pm (Standard Deviation)	68% \pm (3.88)	70% \pm (3.76)	81% \pm (4.45)	58% \pm (4.42)	60% \pm (4.33)	71% \pm (5.56)	48% \pm (6.98)	48% \pm (6.07)	55% \pm (5.97)

Table 5.7: The classification accuracy of the SVM, LDA, and the proposed model with the combined fNIR and EEG data.

Participant #	4-class			6-class			8-class		
	<i>SVM</i>	<i>LDA</i>	<i>Proposed CNN</i>	<i>SVM</i>	<i>LDA</i>	<i>Proposed CNN</i>	<i>SVM</i>	<i>LDA</i>	<i>Proposed CNN</i>
1	77%	80%	92%	70%	65%	90%	54%	50%	74%
2	82%	76%	88%	61%	68%	82%	52%	58%	72%
3	81%	80%	88%	69%	57%	84%	58%	60%	75%
4	86%	82%	90%	65%	64%	90%	61%	52%	76%
5	77%	78%	94%	73%	70%	88%	48%	54%	70%
6	75%	80%	92%	58%	57%	86%	60%	50%	80%
7	80%	77%	94%	62%	69%	82%	55%	48%	78%
8	72%	66%	86%	70%	61%	75%	61%	56%	69%
9	78%	74%	98%	65%	65%	85%	58%	55%	71%
10	71%	76%	84%	65%	53%	75%	55%	50%	70%
11	81%	79%	83%	66%	69%	78%	58%	58%	68%
12	77%	68%	91%	71%	68%	82%	48%	52%	65%
13	78%	80%	90%	65%	68%	80%	60%	54%	65%
14	76%	82%	96%	61%	58%	78%	62%	55%	72%
15	84%	78%	87%	64%	70%	75%	54%	50%	70%
Average \pm (Standard Deviation)	78% \pm (4.11)	77% \pm (4.66)	90% \pm (4.54)	66% \pm (4.23)	64% \pm (5.57)	82% \pm (5.12)	56% \pm (4.49)	53% \pm (3.56)	72% \pm (4.34)

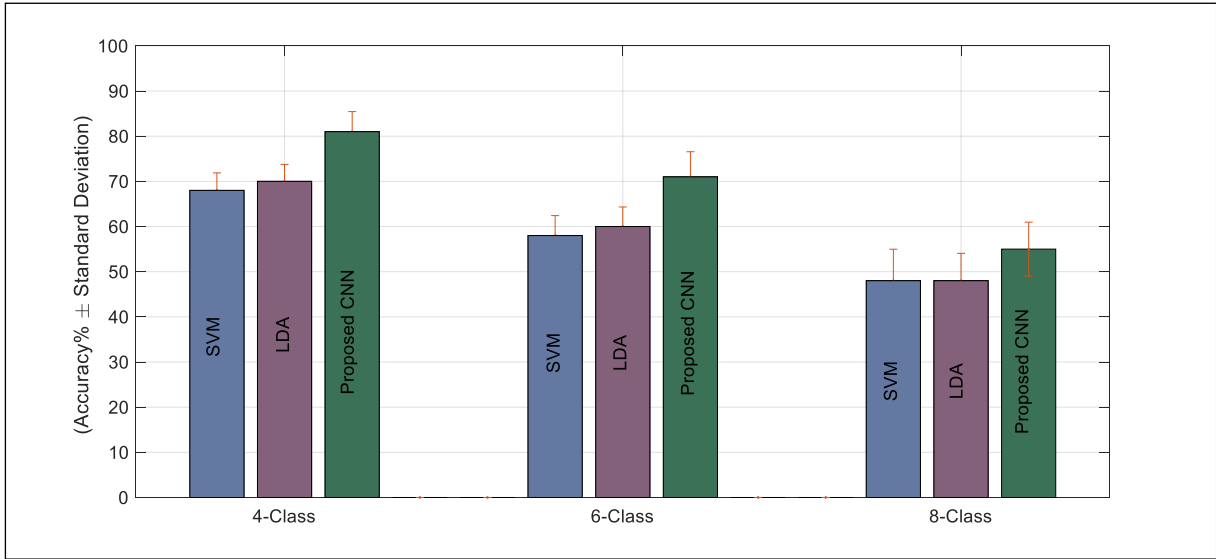


Figure 5.13: Overall performances (mean± standard deviation) of the classification accuracy through SVM, LDA, and the proposed CNN method while only the fNIR data were considered.

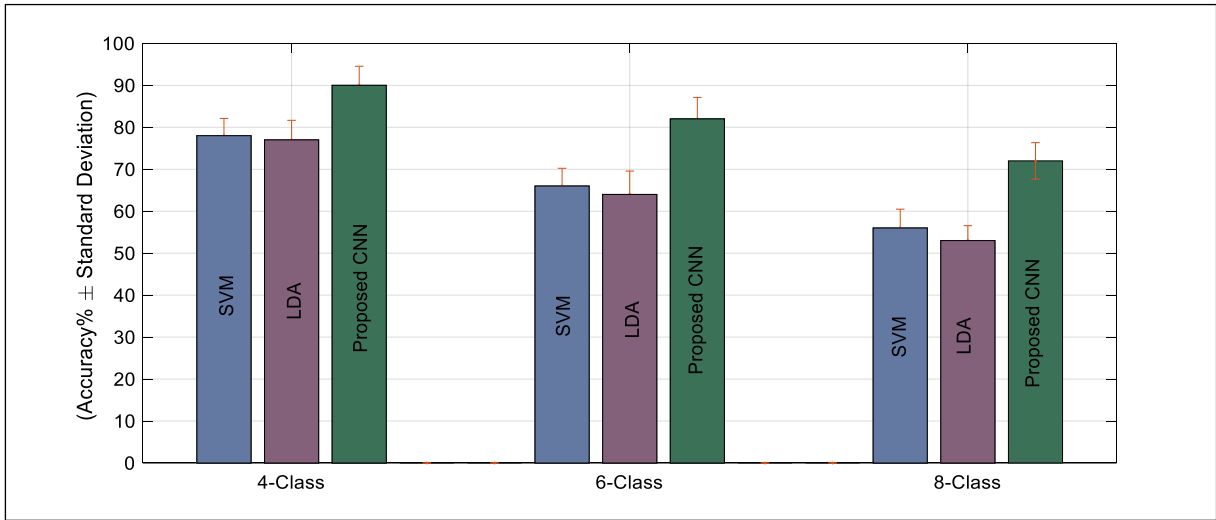


Figure 5.14: Overall performances (mean± standard deviation) of the classification accuracy through SVM, LDA, and the proposed CNN method while combined fNIR and EEG data were considered.

Table 5.8: Comparison of the proposals of the multiple class BCI system.

Research Work	Work Objectives	Methodology	Modality	Resulting Accuracy
4-class database classification				
C. L. Leon <i>et al.</i> 2017 [29]	Combined motor imagery classification	<i>Feature Extraction:</i> Modified CSP <i>Classifier:</i> Multistep SVM	EEG	71.67%
M. A. Rahman <i>et al.</i> 2019 [30]	Moto imagery classification	<i>Feature Extraction:</i> PCA & Wavelet <i>Classifier:</i> Two-step ANN	EEG	74.60%
S. Ge <i>et al.</i> 2014 [26]	Moto imagery classification	<i>Feature Extraction:</i> STFT & CSP <i>Classifier:</i> SVM	EEG	88.1%
A. M. Batula <i>et al.</i> 2014 [31]	Moto imagery classification	<i>Feature Extraction:</i> Mean Value <i>Classifier:</i> SVM	fNIR	54%
J. Shin <i>et al.</i> 2014 [32]	Moto imagery classification	<i>Feature Extraction:</i> Statistical Features <i>Classifier:</i> Naive Bayes classifier	fNIR	83.15%
Proposed Method	Moto imagery classification	Feature Extraction and Classification by CNN	fNIR+EEG	90%
8-class database classification				
C. L. Leon <i>et al.</i> 2017 [29]	Combined motor imagery classification	Feature Extraction: Modified CSP <i>Classifier:</i> Multistep SVM	EEG	51.67%
Proposed Method	Voluntary and imagery motor movement classification	Feature Extraction and Classification by CNN	fNIR+EEG	77%

CSP=Common Spatial Pattern, PCA= Principal Component Analysis, and STFT=Short Time Fourier Transform

These results are found for subject 1 while the models were trained by combined fNIR and EEG data. We have applied two different approaches to find the classification accuracy: one is based on the only fNIR data and the other is the combined information of fNIR and EEG data. The results of 15 participants according are given in **Table 5.6** and **Table 5.7**, respectively. From the result, we get that the combined information provides us greater classification accuracy. For 4, 6, and 8 class problem, the classification accuracies are significantly improved by 9%, 11%, and 17% on average by the combined fNIR-EEG information. The result proves that combined information of fNIR and EEG outperforms the information regarding the fNIR signal alone. In addition, the classification accuracy has been achieved $90 \pm 4.54\%$, $82 \pm 5.12\%$, and $72 \pm 4.34\%$ for 4, 6, and 8 class problem, respectively which is too convincing for the BCI implementation.

5.4 Conclusion

This chapter presents the first research work based on the combined fNIR and EEG signals that deals with up to 8 class problems classification by CNN. Besides, this is the first proposal to decode voluntary and imagery movements combining prefrontal hemodynamic signals (fNIR) along with the frontal and central neuroelectric signal (EEG). This proposal on the bimodal approach for CNN-based BCI implementation finds excellent results in classification accuracy of the voluntary and imagery movement related tasks. It has been also shown that the classification accuracies are increased in the combined fNIR-EEG signal rather than the single modality information (fNIR only). In addition, this proposed research work extends the pathway to implement up to 8 class problem utilizing fNIR and EEG data where most of the current literature discussed 2 or 4 class. This proposed method is robust and efficient to 8 class classification problem along with 4 and 6 class problems which makes hope in establishing an effective BCI for the motor impaired or paralyzed persons.

CHAPTER 6

Conclusions and Future Perspectives

6.1 Conclusions

This research work has been widely examined the voluntary and imagery movement through fNIR and EEG signals. These signals were used to model the activation pattern of the voluntary and imagery movements related prefrontal hemodynamics. In addition, with conventional approach fNIR signals of different movements are classified where it was found that the classification accuracies are not satisfactory to build an effective BCI system. As a result this work has been proposed to add the EEG signals with a novel approach and deployed deep neural network to construct a predictive model to classify the combined fNIR-EEG signal. The outcomes of the proposed method are very significant and convincing. The total outcomes of this research work can pointed with the following lines:

- The voluntary and imagery movements of hands and feet have been analyzed from the prefrontal hemodynamics with fNIR device. The hemodynamic properties regarding these voluntary and imagery movements in the prefrontal cortex have been widely examined in a novel approach.
- The activation pattern of the HbO₂ and dHb due to different voluntary and imagery movements are modeled using polynomial regression method from the prefrontal hemodynamics.
- A novel approach of fNIR and EEG signal combination has been proposed and examined by this work. The proposed method combine the fNIR and EEG signal and make a neuroimage considering its spatiotemporal information
- A deep neural network, CNN has been deployed to build a predictive model for classifying combining information of fNIR and EEG signals regarding the voluntary and imagery movements. This novel approach can predict the movement activity from the fNIR-EEG signal (converted as the proposed combining method) with very high classification accuracy.

- This work has shown that the combined fNIR-EEG signal provides the higher classification accuracies than that of the fNIR signal only.
- This research work classified the fNIR-EEG signals of eight classes so far with very high classification accuracy that recommend this outstanding outcomes of this proposed research method to deploy in practical BCI system design

6.2 Future Perspectives

There is a time-consuming issue to use the deep learning approach. In future, it can be a suitable research guideline for the future researchers to reduce the time consumption of the proposed CNN. In addition, some more classes can be added to implant the practical BCI system that can be very helpful for the disable persons. In addition, all this research work and the corresponding methodologies have been developed for an offline process. With the help of the current research outcomes, an online classification platform with deep neural network can be constructed to reach one step ahead of the practical BCI system.

References

Reference_Chapter_1

- [1] A. Rezeika, M. Benda, F. Gempler, A. Soboor, and I. Volosyak, “Brain-computer interface speller: A review,” *Brain Sciences*, vol. 8, no. 4, pp. 1-38, 2018.
- [2] F. Schettini, A. Riccio, L. Simione, G. Liberati, M. Caruso, V. Frasca, B. Calabrese, M. Mecella, A. Pizzimenti, M. Inghilleri, D. Mattia, and F. Cincotti, “Assistive device with conventional, alternative, and brain-computer interface inputs to enhance interaction with environment for the people with amyotrophic lateral sclerosis: a feasibility and usability study,” *Archives of Physical Medicine and Rehabilitation*, vol. 96, pp. 46-53, 2015.
- [3] S. N. Abdulkader, A. Atia, and M. S. M. Mostafa, “Brain computer interfacing: Applications and challenges,” *Egyptian Informatics Journal*, vol. 16, pp. 213-230, July 2015.
- [4] B. Burle, L. Spieser, C. Roger, L. Casini, T. Hasbroucq, and F. Vidal, “Spatial and temporal resolutions of EEG: Is it really black and white? A scalp current density view,” *International Journal of Psychophysiology*, vol. 97, no. 3, pp. 210-220, September 2015.
- [5] P. K. Mandal, A. Banerjee, M. Tripathi, and A. Sharma, “A comprehensive review of magnetoencephalography (MEG) studies for brain functionality in healthy, aging, and Alzheimer’s disease (AD),” *Frontiers in Computational Neuroscience*, vol. 12, no. 60, pp. 1-22, 2018.
- [6] Basic principles of magnetoencephalography, MIT Class notes, available in: <http://web.mit.edu/kitmitmeg/whatis.html>. last updated 10/24/06
- [7] H. Ayaz, B. Onaral, K. Izzetoglu, P. A. Shewokis, R. McKendrick, and R. Parasuraman, “Continuous monitoring of brain dynamics with functional near infrared spectroscopy as a tool for neuro ergonomic research: empirical examples and a technological development,” *Frontiers in Human Neuroscience*, vol. 7, no. 871, pp. 1-13. December 2013.
- [8] L. H. Ernst, M. M. Plichta, E. Lutz, A. K. Zesewitz, S. V. Tupak, T. Dresler, A. C. Ehlis, and A. J. Fallgatter, “Prefrontal activation patterns of automatic and regulated approach avoidance reactions : a functional near-infrared spectroscopy (fNIRS) study,” *Cortex*, vol. 49, no. 1, pp. 131–142, January 2013.
- [9] D. Ariely and G. S. Berns, “Neuromarketing: the hope and hype of neuroimaging in business,” *Nature Reviews Neuroscience*, vol. 11, pp. 284–292, April 2010.

- [10] F. F. Jöbsis, “Noninvasive infrared monitoring of cerebral and myocardial oxygen sufficiency and circulatory parameters,” *Science*, vol. 198, no. 4323, pp. 1264–1267, December 1977.
- [11] M. Ferrari and V. Quaresima, “A brief review on the history of human functional near-infrared spectroscopy (fNIRS) development and fields of application”, *NeuroImage*, vol. 63, no. 2, pp. 921-935, March 2012.
- [12] M. Ferrari, I. Giannini, A. Carpi, P. Fasella, C. Fieschi, and E. Zanette, “Non-invasive infrared monitoring of tissue oxygenation and circulatory parameters,” *XII World Congress of Angiology*, Athens, September 7–12, 1980.
- [13] Giannini, M. Ferrari, A. Carpi, and P. Fasella, “Rat brain monitoring by near-infrared spectroscopy: an assessment of possible clinical significance,” *Physiological Chemistry and Physics*, vol.14, no. 3, pp. 295–305, 1982.
- [14] M. Soltanlou, M. A. Sitnikova, H. C. Nuerk, and T. Dreseler, “Applications of functional near-infrared spectroscopy (fNIRS) in studying cognitive development: The case of mathematics and language,” *Frontiers in Psychology*, vo. 9, no. 277, pp. 1-15, 2018.
- [15] J. A. Noah, Y. Ono, Y. Nomot, S. Shimada, A. Tachibana, X. Zhang, S. Bronner, and J. Hirsch, “fMRI validation of fNIRS measurements during a naturalistic task,” *Journal of Visualized Experiments*, vol. 100, June 2015.
- [16] X. Cui, S. Bray, D. M. Bryant, G. H. Glover, and A. L. Reiss, “A quantitative comparison of NIRS and fMRI across multiple cognitive tasks,” *Neuroimage*, vol. 54, no.4, pp. 2808–2821, February, 2011.
- [17] T. Nguyen, S. Ahn, H. Jang, S. C. Jun, and J. G. Kim, “Utilization of a combined EEG/NIRS system to predict driver drowsiness,” *Scientific Reports*, vol. 7, no. 43933, pp. 1-10, 2017.
- [18] S. Ahn and S. C. Jun, “Multi-modal integration of EEG-fNIRS for brain computer interfaces-Current limitations and future directions,” *Frontiers in Human Neuroscience*, vol. 11, no. 503, pp. 1-6, 2017.
- [19] A. P. Buccino, H. O. Keles, and A. Omurtag, “Hybrid EEG-fNIRS asynchronous brain-computer interface for multiple motor tasks,” *PLOS One*, vol. 11, no. 1, pp. 1-16, 2016.
- [20] M. H. Lee, S. Fazli, J. Mehnert, and S. W. Lee, “Subject-dependent classification for robust idle state detection using multi-modal neuroimaging and data-fusion techniques in BCI,” *Pattern Recognition*, vol. 8, no. 8, pp. 2725-2737, 2015.

- [21] S. Fazli and S. W. Lee, “Brain-computer interfacing: A multi-modal perspective,” *Journal of Computing Science and Engineering*, vol. 7, no. 2, pp. 132-138, 2013.
- [22] S. Fazli, J. Mehnert, J. Steinbrink, G. Curio, A. Villringer, K. R. Müller, and B. Blankertz, “Enhanced performance by a hybrid NIRS–EEG brain computer interface,” *Neuroimage*, vol. 59, no.1, pp. 519-529, January 2012.
- [23] B. Z. Allison, C. Brunner, V. Kaiser, G. R. Muller-Putz, C. Neuper, and G. Pfurtscheller, “Toward a hybrid brain–computer interface based on imagined movement and visual attention,” *Journal of Neural Engineering*, vol. 7, no.2, April 2010.
- [24] G. Pfurtscheller, B. Z. Allison, C. Brunner, G. Bauernfeind, T. Solis-Escalante, R. Scherer, T. O. Zander, G. Mueller-Putz, C. Neuper and N. Birbaumer, “The hybrid BCI,” *Frontiers in Neuroscience*, vol. 4, no. 30, April 2010.
- [25] H. Aghajani, M. Garbey, and A. Omurtag, “Measuring mental workload with EEG+fNIRS,” *Frontiers in Human Neuroscience*, vol. 11, no. 359, pp. 1-21, 2017.
- [26] “World report on Disability”, by World Bank and WHO 2015. available in : http://www.who.int/disabilities/world_report/2011/report.pdf
- [27] K. S. Hong, M. J. Khan, and M. J. Hong, “Feature extraction and classification methods for hybrid fNIRS-EEG brain-computer interface,” *Frontiers in Human Neuroscience*, vol. 12, no. 246, pp. 1-25, 2018.
- [28] J. Yu, K. K. Ang, C. Guan, and C. Wang, “Supressing system interference in fNIRS monitoring cortical response to motor execution and imagery,” *Frontiers in Human Neuroscience*, vol. 12, no. 85, pp. 1-10, 2018.
- [29] A. Janani and M. Sasikala, “Evaluation of classification performance of functional near infrared spectroscopy signals during movement execution for developing a brain computer-interface application using optimal channels,” *Journal of Near Infrared Spectroscopy*, vol. 26, no. 4, pp. 1-13, 2018.
- [30] M. Batula, J. A. Mark, Y. E. Kim, and H. Ayaz, “Comparison of brain activation during motor imagery and motor movement using fNIRS,” *Computational Intelligence and Neuroscience*, vol. 2017, Article ID 5491296, pp.1-12, May 2017.
- [31] M. Batula, Y. E. Kim, and H. Ayaz, “Virtual and actual humanoid robot control with four-class motor-imagery-based optical brain-computer interface,” *Computational Intelligence and Neuroscience*, volume 2017, no. 1463512, pp. 1-13, July 2017.

- [32] M. S. Vry, D. Saur, M. Rijntjes, R. Umarova, P. Kellmeyer, and S. Schnell, “Ventral and dorsal fiber systems for imagined and executed movement,” *Experimental Brain Research*, vol. 219, pp. 203-216, 2012.
- [33] M. Semrud-Clikeman and T. Ellison, “Functional Neuroanatomy,” *Child Neuropsychology*, pp. 25-46, Springer Science+Business Media, LLC 2009.
- [34] K. Fiehler, M. Burke, A. Engel, S. Bien, and F. Rosler, “Kinesthetic working memory and action control within the dorsal stream,” *Cerebral Cortex*, vol. 8, pp. 243-253, 2007.
- [35] N. R. Carlos, *Physiology of Behaviour*, 5th edition, p. 91, Allyn and Bacon, 1994.
- [36] M. A. Rahman, M. M. Haque, A. Anjum, F. Khanam, M. N. Mollah, and M. Ahmad, “Classification of motor imagery events from prefrontal hemodynamics for BCI application,” *International Joint Conference on Computational Intelligence (IJCCI)*, 14-15 December, 2018, Daffodil International University, Dhaka, Bangladesh. pp. 1-06.
- [37] M. A. Rahman and M. Ahmad, “Evaluating the connectivity of motor area with prefrontal cortex by fnir spectroscopy,” *International Conference on Electrical, Computer and Communication Engineering (ECCE)*, February 16-18, 2017, Cox’s Bazar, Bangladesh.
- [38] M. A. Rahman and M. Ahmad, “Movement related events classification from functional near infrared spectroscopic signal,” *19th International Conference on Computer and Information Technology (ICCIT)*, December 18-20, 2016, North South University, Dhaka, Bangladesh.

Reference_Chapter_2

- [1] R. Abreu, A. Leal, and P. Figueiredo, “EEG-Informed fMRI: A review of data analysis methods,” *Frontiers in Human Neuroscience*, vol. 12, no. 29, pp. 1-23, 2018.
- [2] M. Amouroux, W. Uhring, T. Pebayle, P. Poulet, and L. Marlier, “A safe, low-cost and portable instrumentation for bedside time-resolved picosecond near infrared spectroscopy,” *Novel Optical Instrumentation for Biomedical Applications IV*, vol. 1, pp.7371-7377, July 2009.
- [3] P. K. Mandal, A. Banerjee, M. Tripathi, and A. Sharma, “A comprehensive review of magnetoencephalography (MEG) studies for brain functionality in healthy, aging, and Alzheimer’s disease (AD),” *Frontiers in Computational Neuroscience*, vol. 12, no. 60, pp. 1-22, 2018.

- [4] B. Burle, L. Spieser, C. Roger, L. Casini, T. Hasbroucq, and F. Vidal, "Spatial and temporal resolutions of EEG: Is it really black and white? A scalp current density view," *International Journal of Psychophysiology*, vol. 97, no. 3, pp. 210-220, September 2015.
- [5] T. G. Phan and A. Bullen, "Practical intravital two-photon microscopy for immunological research: faster, brighter, deeper," *Immunology and Cell Biology*, vol. 88, pp.438-444, January 2010.
- [6] F. F. Jöbsis, "Noninvasive infrared monitoring of cerebral and myocardial oxygen sufficiency and circulatory parameters," *Science*, vol. 198, no. 4323, pp. 1264–1267, December 1977.
- [7] M. Soltanlou, M. A. Sitnikova, H. C. Nuerk and T. Dresler, "Applications of Functional Near-Infrared Spectroscopy (fNIRS) in Studying Cognitive Development: The Case of Mathematics and Language," *Frontiers in Psychology*, vol. 9, no. 277, pp. 1-15, 2016.
- [8] M. A. Kamran, M. M. N. Mannan, and M. Y. Jeong, "Cortical signal analysis and advances in functional near-infrared spectroscopy signal: A review," *Frontiers in Human Neuroscience*, vol. 10, no. 61, pp. 1-12, 2016.
- [9] Y. Hoshi, "Towards the next generation of near-infrared spectroscopy," *Philosophical transactions of the royal society A*, vol. 369, pp. 4425-4439, November 2011.
- [10] J. S. Damoiseaux, S. A. R. B. Rombouts, F. Barkhof, P. Scheltens, C. J. Stam, S. M. Smith, and C. F. Beckmann, "Consistent resting-state networks across healthy subjects," *Proceedings of the national academy of sciences of the United States of America*, vol. 103, no. 37, pp. 13848–13853, February 2006.
- [11] M. A. Rahman and M. Ahmad, "Identifying Appropriate Feature to Distinguish between Resting and Active Condition from FNIRS," 3rd *International Conference on Signal Processing and Integrated Networks*, SPIN 2016, Amity University, Noida, New Delhi, India, February 2016.
- [12] D. A. Gusnard, E. Akbudak, G. L. Shulman, and M. E. Raichle, "Medial prefrontal cortex and self-referential mental activity: Relation to a default mode of brain function," *Proceedings of the national academy of sciences of the United States of America*, vol. 98, no. 7, pp. 4259-4264, March 2001.
- [13] H. Obrig and A. Villringer, "Beyond the visible-imaging the human brain with light," *Journal of Cerebral Blood Flow & Metabolism*, vol. 23, no. 1, pp. 1–18, January 2003.

- [14] A. Villringer and B. Chance, "Non-invasive optical spectroscopy and imaging of human brain function," *Trends in Neurosciences*, vol. 20, no. 10, pp. 435-442, October 1997.
- [15] D. J. Heeger and D. Ress, "What does fMRI tell us about neuronal activity?," *Nature Reviews Neuroscience*, vol. 3, pp. 142-151, February 2002.
- [16] M. Izzetoglu, S. C. Bunce, K. Izzetoglu, B. Onaral, and K. Pourrezaei, "Functional brain imaging using near-infrared technology," *IEEE Engineering in Medicine and Biology Magazine*, vol. 26, no. 4, July/August 2007.
- [17] A. Bozkurt, A. Rosen, H. Rosen, and B. Onaral, "A portable near infrared spectroscopy system for bedside monitoring of newborn brain," *Biomedical Engineering Online*, vol. 4, no. 29, pp. 1-11, 2005.
- [18] J. Mayhew, S. Askew, Y. Zheng, J. Porrill, G. W. M. Westby, P. Redgrave, D. M. Rector, and R. M. Harper, "Cerebral Vasomotion: A 0.1Hz oscillation in reflected light imaging of neural activity," *Neuroimage*, vol. 4, pp. 183-193, 1996.
- [19] C. E. Elwell, R. Springett, E. Hillman, and D. T. Delpy, "Oscillations in cerebral hemodynamics: Implications for functional activation studies," *Advances in Experimental Medicine and Biology*, vol. 471, pp. 57-65, 1999.
- [20] H. Obrig, M. Neufang, R. Wenzel, M. Kohl, J. Steinbrink, K. Einhaupl, and A. Villringer, "Spontaneous low frequency oscillations of cerebral hemodynamics and metabolism in human adults," *Neuroimage*, vol. 12, pp. 623-639, 2000.
- [21] N. Lundberg, H. Troupp, and H. Lorin, "Continuous recordings and control of ventricular fluid pressure in neurosurgical practice," *Journal of Neurosurgery & Experimental Neurology*, vol. 22, no. 6, pp. 581-590, 1962. DOI: 10.1097/00005072-196207000-00018
- [22] H. Ayaz, P. A. Shewokis, A. Curtin, M. Izzetoglu, K. Izzetoglu, and B. Onaral, "Using mazesuite and functional near infrared spectroscopy to study learning in spatial navigation," *Journal of Visualized Experiments*, vol. 56, pp. 1-11. October 2011.
- [23] A. Devaraj, "Signal processing for functional near-infrared neuroimaging," M.Sc. Thesis, Drexel University, Philadelphia, 2010.
- [24] M. Izzetoglu, S. C. Bunce, K. Izzetoglu, B. Onaral, and K. Pourrezaei, "Functional brain imaging using near-infrared technology," *IEEE Engineering in Medicine and Biology Magazine*, 26, pp. 38-46, 2007.

- [25] H. Ayaz, P. A. Shewokis, S. Bunce, K. Izzetoglu, B. Willems, and B. Onaral, "Optical brain monitoring for operator training and mental workload assessment," *NeuroImage*, vol. 59, pp. 36-47, 2012.
- [26] H. Ayaz, P. A. Shewokis, M. İzzetoğlu, M. P. Çakır, and B. Onaral, "Tangram solved? Prefrontal cortex activation analysis during geometric problem solving," *Annual International Conference of the IEEE Engineering in Medicine and Biology Society*, San Diego, CA, 2012, pp. 4724-4727.
- [27] H. Meiria, I. Selaa, P. Neshet, M. Izzetoglu, K. Izzetoglu, B. Onaral, and Z. Breznitz, "Frontal lobe role in simple arithmetic calculations: An fNIR study," *Neuroscience Letters*, vol. 510, pp. 43-47, 2012.
- [28] Y. Liu, H. Ayaz, A. Curtin, B. Onaral, and P. A. Shewokis, "Towards a hybrid P300-based BCI using simultaneous fNIR and EEG," *Lecture Notes in Computer Science*, vol. 8027. Springer, Berlin, Heidelberg Foundations of Augmented Cognition, pp.335-344, 2013.
- [29] A. M. Batula, H. Ayaz, and Y. E. Kim, "Evaluating a four-class motor-imagery-based optical brain-computer interface," *36th Annual International Conference of the IEEE Engineering in Medicine and Biology Society*, Chicago, IL, 2014, pp. 2000-2003.
- [30] M. A. Rahman, M. A. Rashid, and M. Ahmad, "Selecting the optimal conditions of savitzky-golay filter for fNIRS signal," *Biocybernetics and Biomedical Engineering*, vol. 39, no. 3, pp. 624-637, 2019.
- [31] K. Hong, M. J. Khan, and M. J. Hong, "Feature extraction and classification methods for hybrid fNIRS-EEG brain-computer interfaces," *Frontiers in Human Neuroscience*, vol. 12, no. 246, 2018.
- [32] K. Djansezian, "How does the brain produce movement?," Chapter 10, North Dakota University, Available in: https://www.ndsu.edu/faculty/pavek/Psych486_686/chapterpdfs1stedKolb/kolb_10.pdf
- [33] S. C. Wriessnegger, J. Kurzmam, and C. Neuper, "Spatio-temporal differences in brain oxygenation between movement execution and imagery: a multichannel near-infrared spectroscopy study," *International Journal of Psychophysiology*, vol. 67, no. 1, pp. 54-63, 2008.
- [34] K. Blinowska and P. Durka, "Electroencephalography (EEG)," *Wiley Encyclopedia of Biomedical Engineering*, Copyright & 2006 John Wiley & Sons, Inc.
- [35] P. Olejniczak, "Neurophysiologic Basis of EEG," *Journal of Clinical Neurophysiology*, vol. 23, no. 3, pp. 186-189, 2006.

- [36] R. W. Homan, J. Herman and P. Purdy, "Cerebral location of international 10-20 system electrode placement," *Electroencephalography and Clinical Neurophysiology*, vol. 66, pp. 376-382, 1987.
- [37] R. W. Homan, "The 10-20 electrode system and cerebral location", *American Journal of EEG Technology*, vol. 28, no. 4, pp. 269-279, 1988.
- [38] G. H. Klem, H. O. Lüder, H. H. Jasper, and C. Elger, "The ten±twenty electrode system of the international federation," Recommendations for the Practice of Clinical Neurophysiology: Guidelines of the International Federation of Clinical Physiology (EEG Suppl. 52).
- [39] S. Noachtar, C. Binnie, J. Ebersole, F. Mauguière, A. Sakamoto, and B. Westmoreland, "A glossary of terms most commonly used by clinical electroencephalographers and proposal for the report form for the EEG findings. The international federation of clinical neurophysiology," *Electroencephalography and clinical neurophysiology Supplement*, vol. 52, no. 1, pp. 21-41, 1999.
- [40] A. Moller, Auditory physiology, New York: Academic Press, 1983.
- [41] A. Vuckovic, V. Radivojevic, A. C. N. Chen and D. B. Popovic, "Automatic recognition of alertness and drowsiness from EEG by an artificial neural network," *Medical Engineering & Physics*, vol. 24, no. 5, pp. 349-60, July 2002.
- [42] L. M. Oberman, E. M. Hubbard, J. P. McCleery, E. L. Altschuler, V. S. Ramachandran, and J. A. Pineda, "EEG evidence for mirror neuron dysfunction in autism spectrum disorders," *Cognitive Brain Research*, vol. 24, no. 2, pp. 190–198, 2005.
- [43] Y. Kim, J. Ryu, K. K. Kim, C. C. Took, D. P. Mandic, and C. Park, "Motor imagery classification using mu and beta rhythms of EEG with strong uncorrelating transform based complex common spatial patterns," *Computational Intelligence and Neuroscience*, vol. 2016, Article ID 1489692, 2016.
- [44] B. Singh and H. Wagatsuma, "A removal of eye movement and blink artifacts from EEG data using morphological component analysis," *Computational and Mathematical Methods in Medicine*, vol. 2017, ArticleID 1861645, pp. 1-17, 2017.
- [45] Y. Li, Z. Ma, W. Lu and Y. Li, "Automatic removal of the eye blink artifact from EEG using an ICA-based template matching approach," *Physiological Measurement*, vol. 27, no. 4, pp. 425–436, 2006.

- [46] G. Pfurtscheller, C. Neuper, D. Flotzinger, and M. Pregenzer, “EEG-based discrimination between imagination of right and left hand movement,” *Electroencephalography and clinical Neurophysiology*, vol. 103, no. 6, pp. 642–651, 1997.
- [47] M. Pregenzer and G. Pfurtscheller, “Frequency component selection for an EEG-based brain to computer interface,” *IEEE Transactions on Rehabilitation Engineering*, vol. 7, no. 4, pp. 413–419, 1999.
- [48] C. Neuper, R. Scherer, M. Reiner, and G. Pfurtscheller, “Imagery of motor actions: Differential effects of kinesthetic and visual–motor mode of imagery in single-trial EEG,” *Cognitive Brain Research*, vol. 25, no. 3, pp. 668–677, 2005.

Reference Chapter 3

- [1] H. Ayaz, M. Izzetoglu, P. A. Shewokis, and B. Onaral, “Sliding-window motion artifact rejection for functional near-infrared spectroscopy,” *32nd Annual International Conference of the IEEE EMBS Buenos Aires, Argentina*, August 31-September 4, 2010.
- [2] Y. Liu, H. Ayaz, B. Onaral, and P. A. Shewokis, “Neural adaption to a working memory task: A concurrent EEG-fNIRS study,” *Foundations of Augmented Cognition 2015. Lecture Notes in Computer Science*, vol. 9183, pp. 268-280.
- [3] A. Devaraj, “Signal processing for functional near-infrared neuroimaging,” M.Sc. Thesis, Drexel University, Philadelphia, 2010.
- [4] J. G. Proakis and D. G. Manolakis, “Digital Signal Processing: Principles, Algorithms, and Applications,” Third Edition, Prentice-Hall of India Private Limited, New Delhi, 2002.
- [5] A. Janani and M. Sasikala, “Investigation of different approaches for noise reduction in functional near-infrared spectroscopy signals for brain-computer interface applications,” *Neural Computing and Applications*, vol. 28, no. 10, pp. 2889–2903, April 2017.
- [6] N. T. Hai, N. Q. Cuong, T. Q. D. Kho, and V. V. Toi, “Temporal hemodynamic classification of two hands tapping using functional near-infrared spectroscopy,” *Frontiers in Neuroscience*, vol. 7, no. 516, pp. 1-12, September 2013.
- [7] M. Strait and M. Scheutz, “What we can and cannot (yet) do with functional near infrared spectroscopy,” *Frontiers in Neuroscience*, vol. 8, no. 117, pp. 1-12, May 2014.

- [8] J. Shin and J. Jeong, "Multiclass classification of hemodynamic responses for performance improvement of functional near-infrared spectroscopy-based brain-computer interface," *Journal of Biomedical Optics*, vol. 19, no. 6, pp. 067009-1~067009-9, June 2014.
- [9] A. Savitzky and M. J. E. Golay, "Soothing and differentiation of data by simplifying least squares procedures," *Analytical Chemistry*, vol. 36, pp. 1627-1639, 1964.
- [10] R. W. Schafer, "What is a Savitzky-Golay filter? [Lecture Notes]," *IEEE Signal Processing Magazine*, vol. 28, no. 4, pp. 111-117, July 2011.
- [11] M. A. Rahman, M. A. Rashid, and M. Ahmad, "Selecting the optimal conditions of Savitzky-Golay filter for fNIRS signal," *Biocybernetics and Biomedical Engineering*, vol. 39, no. 3, pp. 624-637, 2019. DOI:10.1016/j.bbe.2019.06.004
- [12] B. Boashash, "Time-Frequency signal analysis and processing: A comprehensive reference," Second Edition, Eurasip and Academic Press Series in Signal and Image Processing, December 2015.
- [13] S. C. Wiriessnegger, J. Kurzman, and C. Neuper, "Spatio-temporal differences in brain oxygenation between movement execution and imagery: a multichannel near-infrared spectroscopy study," *International Journal of Psychophysiology*, vol. 67, no. 1, pp. 54-63, 2008.
- [14] A. M. Batula, J. A. Mark, Y. E. Kim, and H. Ayaz, "Comparison of brain activation during motor imagery and motor movement using fNIRS," *Computational Intelligence and Neuroscience*, vol. 2017, Article ID 5491296, pp.1-12, 2017.
- [15] S. J. Orfanidis, "Lecture Notes on Elliptic Filter Design," Department of Electrical & Computer Engineering, November 20, 2006.
- [16] M. S. Chavan, R. Agarwala, and M. D. Uplane, "Digital elliptic filter application for noise reduction in ECG signal," *WSEAS Transactions on Electronics*, vol. 3, no. 1, 2006.
- [17] M. D. Lutovac, D. V. Tasic, and B. L. Evans, *Filter Design for Signal Processing*, Prentice Hall, Upper Saddle River, NJ, 2001.
- [18] M. Vlcek and R. Unbehauen, "Degree, Ripple, and Transition Width of Elliptic Filters," *IEEE Transaction on Circuit and System*, CAS-36, 469 (1989).
- [19] S. J. Orfanidis, *Introduction to Signal Processing*, Prentice Hall, Upper Saddle River, NJ, 1996.

- [20] N. Mammone and F. C. Morabito, "Enhanced automatic wavelet independent component analysis for electroencephalographic artifact removal," *Entropy*, vol. 16, no. 12, pp. 6553-6572, 2014.
- [21] R. N. Khushaba, S. Kodagoda, S. Lal, and G. Dissanayake, "Driver drowsiness classification using fuzzy wavelet-packet-based feature-extraction algorithm," *IEEE Transactions on Biomedical Engineering*, vol. 58, no. 1, pp. 121-131, 2011.
- [22] M. A. Rahman, M. K. Hossain, F. Khanam, M. K. Alam, and M. Ahmad, "Four-class motor imagery EEG signal classification using PCA, wavelet, and two-stage neural network," *International Journal of Advanced Computer Science and Applications*, vol. 10, no. 5, May 2019. DOI: 10.14569/IJACSA.2019.0100562.
- [23] M. K. Wali, M. Murugappan, and B. Ahmmad, "Wavelet packet transform based driver distraction level classification using EEG," *Mathematical Problems in Engineering*, vol. 2013, Article ID 297587, 10 pages, 2013.
- [24] F. Khanam, M. A. Rahman, and M. Ahmad, "Evaluating Alpha Relative Power of EEG Signal during Psychophysiological Activities in Salat," *International Conference on Innovations in Science, Engineering and Technology (ICISSET)*, 27-28, 2018, Bangladesh, pp. 1-06.
- [25] E. C. Ifeakor and B. W. Jervis, *Digital Signal Processing: A Practical Approach*, Addison Wesley Publishers Ltd., 1993.
- [26] B. Zhijie, L. Qiuli, W. Lei, L. Chengbiao, Y. Shimin, and L. Xiaoli, "Relative power and coherence of EEG series are related to amnesic mild cognitive impairment in diabetes," *Frontiers in Aging Neuroscience*, vol. 6, no. 11, February 2014.
- [27] R. A. Khan, N. Naseer, N. K. Qureshi, F. M. Noori, H. Nazeer, and M. U. Khan, "fNIRS-based neurorobotic interface for gait rehabilitation," *Journal of Neuroengineering and Rehabilitation*, vol. 15, no.7, 2018.
- [28] A. Zafar and K. S. Hong, "Detection and classification of three class initial dips from prefrontal cortex," *Biomedical Optics Express*, vol. 8, pp. 367-383, 2017.
- [29] M. J. Khan and K. S. Hong, "Hybird EEG-fNIRS-based eight command decoding for BCI: application to quadcopter control," *Frontiers in Neurorobotics*, vol.11, no. 6, 2017.
- [30] R. Polikar, "Ensemble based systems in decision making," *IEEE Circuits and Systems Magazine*, vol. 6, no. 3, pp. 21-45, 2006.

- [31] K. Hong, M. J. Khan and M. J. Hong, “Feature extraction and classification methods for hybrid fNIRS-EEG brain-computer interfaces,” *Frontiers in Human Neuroscience*, vol. 12, no. 246, 2018.
- [32] N. Naseer, N. K. Qureshi, F. M. Noori, and K. S. Hong, “Analysis of different classification techniques for two-class functional near-infrared spectroscopy-based brain-computer interface,” *Computational Intelligence and Neuroscience*, vol. 2016, no. 5480760, pp. 1-11, 2016.
- [33] X. Li, C. Jiang, J. Tang, Y. Chen, D. Yang, and Z. Chen, “A Fisher’s criterion-based linear discriminant analysis for predicting the critical values of coal and gas outbursts using the initial gas flow in a borehole,” *Mathematical Problems in Engineering*, vol. 2017, no. 7189803, pp. 1-11, 2017.
- [34] L. Luan, Y. Wang, X. Li, W. Hu, K. Li, J. Li, K. Yang, R. Shu, L. Zhaoa, and C. Laoa, “Application of multiple classifier fusion in the discriminant analysis of near infrared spectroscopy for agricultural products,” *Journal of Near Infrared Spectroscopy*, vol. 24, pp. 363–372, 2016.
- [35] Y. Zhang, Q. Deng, W. Liang, and X. Zou, “An efficient feature selection strategy based on multiple support vector machine technology with gene expression data,” *BioMed Research International*, vol. 2018, no. 7538204, pp. 1-11, 2018.
- [36] J. Shin and J. Jeong, “Multiclass classification of hemodynamic responses for performance improvement of functional near infrared spectroscopy-based brain-computer interface,” *Journal of Biomedical Optics*, vol. 19, no. 6, no. 067009, 2014.
- [37] N. Naseer, M. J. Hong, and K.-S. Hong, “Online binary decision decoding using functional near-infrared spectroscopy for the development of brain-computer interface,” *Experimental Brain Research*, vol. 232, no. 2, pp. 555–564, 2014.
- [38] S. Huang, N. Cai, P. P. Pacheco, S. Narandes, Y. Wang, and W. Xu, “Applications of support vector machine (SVM) learning in cancer genomics,” *Cancer Genomics & Proteomics*, vol. 15, pp. 41-51, 2018.
- [39] X. Wu, V. Kumar, J. R. Quinlan, J. Ghosh, Q. Yang, et. al., “Top 10 algorithms in data mining,” *Knowledge Information System*, vol. 14, pp.1–37, 2008.
- [40] M. A. Rahman, M. M. Haque, A. Anjum, M. N. Mollah, and M. Ahmad, “Classification of motor imagery events from prefrontal hemodynamics for BCI application,” *Springer Book Series: Algorithms for Intelligent System*, 2018.

- [41] Phil Kim, MATLAB Deep Learning With Machine Learning, Neural Networks and Artificial Intelligence, Apress, 2017. ISBN-13 (electronic): 978-1-4842-2845-6, DOI 10.1007/978-1-4842-2845-6.
- [42] M. Matsugu, K. Mori, Y. Mitari, and Y. Kaneda, "Subject independent facial expression recognition with robust face detection using a convolutional neural network," *Neural Networks*, 2003.
- [43] A. Krizhevsky, I. Sutskever, and G. E. Hinton, "Imagenet classification with deep convolutional neural networks," *Advances in Neural Information Processing Systems*, 2012, pp. 1097-1105.
- [44] Vendran Vuukotic, Josip Krapac, and Sinisa Segvic, "Convolutional Neural Network for Croatian Traffic Signs Recognition," Available at <https://github.com/v-v/CNN/>
- [45] S. Iofie and C. Szegedy, "Batch normalization: Accelerating deep network training by reducing internal covariate shift," *International Conference on Machine Learning*, 2015, pp. 448-456.
- [46] V. Nair and G. E. Hinton, "Rectified linear units improve restricted Boltzmann machines," *27th International Conference on Machine Learning (ICML-10)*, 2010, pp. 807-814.
- [47] Y. A. LeCun, L. Bottou, G. B. Orr, and K.-R. Muller, "Efficient backprop," in *Neural Networks: Tricks of the trade*, Springer, 2012, pp. 9-48.
- [48] Y. A. LeCun, L. Bottou, Y. Bengio, and P. Haffner, "Gradient-based learning applied to document recognition," *Proceedings of the IEEE*, 1998.
- [49] Y. LeCun and Y. Bengio, "Convolutional networks for images, speech, and time series," *The handbook of brain theory and neural networks*, 1995.
- [50] D. Scherer, A. Muller, and S. Behnke, "Evaluation of pooling operations in convolutional architectures for object recognition," in *International Conference on Artificial Neural Networks (ICANN) 2010*, Springer, 2010.
- [51] A. Deshpande, "A Beginner's Guide to Understanding Convolutional Neural Networks," Available in: <https://adeshpande3.github.io/A-Beginner%27s-Guide-To-Understanding-Convolutional-Neural-Networks/>

Reference Chapter 4

- [1] M. A. Rahman, "Matlab Based Graphical Protocol," MATLAB Central File Exchange. Retrieved October 20, 2018. Available in: <https://www.mathworks.com/matlabcentral/fileexchange/69162-matlab-based-graphical-protocol>.

- [2] R. C. Oldfield, "The assessment and analysis of handedness: The Edinburgh inventory," *Neuropsychologia*, vol. 9, pp. 97-113, 1971.
- [3] World medical association declaration of helsinki-ethical principles for medical research involving human subjects, Adopted by 64th WMA General Assembly, Fortaleza, Brazil, Special Communication: Clinical Review & Education, 2013.
- [4] H. Ayaz, "Functional near infrared spectroscopy based brain computer interface," *PhD Thesis*, Drexel University, Philadelphia, 2010.
- [5] Y. Liu, H. Ayaz, B. Onaral, and P. A. Shewokis, "Neural adaption to a working memory task: A concurrent EEG-fNIRS study," *Foundations of Augmented Cognition 2015. Lecture Notes in Computer Science*, vol. 9183, pp. 268-280.
- [6] B. Boashash, "Time-Frequency Signal Analysis and Processing: A Comprehensive Reference," Second Edition, Eurasip and Academic Press Series in Signal and Image Processing, 2015.
- [7] G. M. Sullivan and R. Feinn, "Using effect size—or why the P value is not enough," *Journal of Graduate Medical Education*, vol. 4, no. 3, pp. 279–282, 2012.
- [8] M. A. Rahman and M. Ahmad, "A straightforward signal processing scheme to improve effect size of fNIR signals," 5th *International Conference on Informatics, Electronics & Vision, ICIEV 2016*, Dhaka University, Dhaka, Bangladesh, May 2016.
- [9] N. T. Hai, N. Q. Cuong, T. Q. Dang Khoa, and V. V. Toi, "Temporal hemodynamic classification of two hands tapping using functional near-infrared spectroscopy," *Frontiers in Human NeuroScience*, vol. 7, no. 516, pp. 1-12, September 2013.
- [10] H. Ayaz, M. Izzetoglu, S. M. Platek, S. Bunce, K. Izzetoglu, K. Pourrezaei, and B. Onaral, "Registering fNIR data to brain surface image using MRI templates," 28th *Annual International Conference of the IEEE EMBS*, 2006, pp. 2671-2674.

Reference_Chapter_5

- [1] S. N. Abdulkader, A. Atia, and M. S. M. Mostafa, "Brain computer interfacing: Applications and challenges," *Egyptian Informatics Journal*, vol. 16, pp. 213-230, July 2015.
- [2] B. Burle, L. Spieser, C. Roger, L. Casini, T. Hasbroucq, and F. Vidal, "Spatial and temporal resolutions of EEG: Is it really black and white? A scalp current

- density view,” *International Journal of Psychophysiology*, vol. 97, no. 3, pp. 210-220, September 2015.
- [3] Basic principles of magnetoencephalography, MIT Class notes, available in: <http://web.mit.edu/kitmitmeg/whatis.html>. last updated 10/24/06
- [4] D. Ariely and G. S. Berns, “Neuromarketing: the hope and hype of neuroimaging in business,” *Nature Reviews Neuroscience*, vol. 11, pp. 284–292, April 2010.
- [5] H. Ayaz, B. Onaral, K. Izzetoglu, P. A. Shewokis, R. McKendrick, and R. Parasuraman, “Continuous monitoring of brain dynamics with functional near infrared spectroscopy as a tool for neuro ergonomic research: empirical examples and a technological development,” *Frontiers in Human Neuroscience*, vol. 7, no. 871, pp. 1-13. December 2013.
- [6] L. H. Ernst, M. M. Plichta, E. Lutz, A. K. Zesewitz, S. V. Tupak, T. Dresler, A. C. Ehlis, and A. J. Fallgatter, “Prefrontal activation patterns of automatic and regulated approach avoidance reactions: a functional near-infrared spectroscopy (fNIRS) study,” *Cortex*, vol. 49, no. 1, pp. 131–142, January 2013.
- [7] F. F. Jöbsis, “Noninvasive infrared monitoring of cerebral and myocardial oxygen sufficiency and circulatory parameters,” *Science*, vol. 198, no. 4323, pp. 1264–1267, December 1977.
- [8] M. Ferrari and V. Quaresima, “A brief review on the history of human functional near-infrared spectroscopy (fNIRS) development and fields of application”, *NeuroImage*, vol. 63, no. 2, pp. 921-935, March 2012.
- [9] M. Ferrari, I. Giannini, A. Carpi, P. Fasella, C. Fieschi, and E. Zanette, “Non-invasive infrared monitoring of tissue oxygenation and circulatory parameters,” XII World Congress of Angiology 1980, Athens, September 7–12.
- [10] I. Giannini, M. Ferrari, A. Carpi, and P. Fasella, “Rat brain monitoring by near-infrared spectroscopy: an assessment of possible clinical significance,” *Physiological Chemistry and Physics*, vol. 14, no. 3, pp. 295–305, 1982.
- [11] X. Cui, S. Bray, D. M. Bryant, G. H. Glover, and A. L. Reiss, “A quantitative comparison of NIRS and fMRI across multiple cognitive tasks,” *Neuroimage*, vol. 54, no. 4, pp. 2808–2821, February 2011.
- [12] J. A. Noah, Y. Ono, Y. Nomot, S. Shimada, A. Tachibana, X. Zhang, S. Bronner, and J. Hirsch, “fMRI validation of fNIRS measurements during a naturalistic task,” *Journal of Visualized Experiments*, vol. 100, June 2015.
- [13] B. Z. Allison, C. Brunner, V. Kaiser, G. R. Muller-Putz, C. Neuper, and G. Pfurtscheller, “Toward a hybrid brain-computer interface based on imagined movement and visual attention,” *Journal of Neural Engineering*, vol. 7, no. 2, April 2010.
- [14] G. Pfurtscheller, B. Z. Allison, C. Brunner, G. Bauernfeind, T. Solis-Escalante, R. Scherer, T. O. Zander, G. Mueller-Putz, C. Neuper and N.

- Birbaumer, “The hybrid BCI,” *Frontiers in Neuroscience*, vol. 4, no. 30, April 2010.
- [15] S. Fazli, J. Mehnert, J. Steinbrink, G. Curio, A. Villringer, K. R. Müller, and B. Blankertz, “Enhanced performance by a hybrid NIRS–EEG brain-computer interface,” *Neuroimage*, vol. 59, No.1, pp. 519-529, January 2012.
- [16] M. H. Lee, S. Fazli, J. Mehnert, and S. W. Lee, “Improving the performance of brain-computer interface using multi-modal neuroimaging,” 2nd *IAPR Asian Conference on Pattern Recognition*, Naha, 2013, pp. 511-515.
- [17] M. H. Lee, S. Fazli, J. Mehnert, and S. W. Lee, “Subject-dependent classification for robust idle state detection using multi-modal neuroimaging and data-fusion techniques in BCI,” *Pattern Recognition*, vol. 48, no. 8, pp. 2725-2737, August 2015.
- [18] P. Buccino, H. O. Keles, and A. Omurtag, “Hybrid EEG-fNIRS asynchronous brain-computer interface for multiple motor tasks,” *PLOS One*, vol.11, no.1, January 2016.
- [19] “World report on Disability”, by World Bank and WHO 2015. available in: http://www.who.int/disabilities/world_report/2011/report.pdf.
- [20] T. Trakoolwilaiwan, B. Behboodi, J. Lee, K. Kim, and J. W. Choi, “Convolutional neural network for high-accuracy functional near-infrared spectroscopy in a brain–computer interface: three-class classification of rest, right-, and left-hand motor execution,” *NeuroPhotonics*, vol. 15, no. 1, 2018.
- [21] A. Emamia, N. Kuniib, T. Matsuoc, T. Shinozakid, K. Kawaie, and H. Takahashia, “Seizure detection by convolutional neural network-based analysis of scalp electroencephalography plot images,” *NeuroImage: Clinical*, vol. 22, 2019.
- [22] S. Opałka, B. Stasiak, D. Szajerman, and A. Wojciechowski, “Multi-channel convolutional neural networks architecture feeding for effective EEG mental tasks classification,” *Sensors*, vol. 18, pp. 1-21, 2018.
- [23] T. Cheng, C. Rui, W. Bin, N. Yan, H. Ting, G. Hao, and X. Jie, “Epileptic Seizure Detection Based on EEG Signals and CNN,” *Frontiers in Neuroinformatics*, vol. 12, pp. 1-95, 2018..
- [24] World medical association declaration of helsinki-ethical principles for medical research involving human subjects, Adopted by 64th WMA General Assembly, Fortaleza, Brazil, Special Communication: Clinical Review & Education, 2013.
- [25] P. K. Mishra, B. Jagadish, M. P. R. S. Kiran, P. Rajalakshmi and D. S. Reddy, “A novel classification for EEG based four class motor imagery using kullback-leibler regularized riemannian manifold,” *IEEE 20th International Conference on e-Health Networking, Applications and Services (Healthcom)*, Ostrava, 2018, pp. 1-5.

- [26] S. Ge, R. Wang, and D. Yu, "Classification of four-class motor imagery employing single-channel electroencephalography," *PLOS One*, vol. 9, no. 6, pp. 1-7, 2014.
- [27] M. A. Rahman, Matlab Based Graphical Protocol. MATLAB Central File Exchange. Retrieved October 20, 2018. Available in: <https://www.mathworks.com/matlabcentral/fileexchange/69162-matlab-based-graphical-protocol>.
- [28] S. C. Wiriessnegger, J. Kurzmann, and C. Neuper, "Spatio-temporal differences in brain oxygenation between movement execution and imagery: a multichannel near-infrared spectroscopy study," *International Journal of Psychophysiology*, vol. 67, no. 1, pp. 54-63, 2008.
- [29] C. L. León, "Multilabel classification of EEG-based combined motor imageries implemented for the 3D control of a robotic arm," Ph.D. Thesis, Université de Lorraine, 2017.
- [30] M. A. Rahman, M. K. Hossain, F. Khanam, M. K. Alam, and M. Ahmad, "Four-class motor imagery EEG signal classification using PCA, Wavelet, and Two-stage neural network," *International Journal of Advanced Computer Science and Applications*, vol. 10, no. 5, May 2019. DOI: 10.14569/IJACSA.2019.0100562.
- [31] A. M. Batula, H. Ayaz, and Y. E. Kim, "Evaluating a four-class motor-imagery-based optical brain-computer interface," *36th Annual International Conference of the IEEE Engineering in Medicine and Biology Society*, Chicago, IL, 2014, pp. 2000-2003. DOI: 10.1109/EMBC.2014.6944007
- [32] J. Shin and J. Jeong, "Multiclass classification of hemodynamic responses for performance improvement of functional near-infrared spectroscopy-based brain-computer interface," *Journal of Biomedical Optics*, vol. 19, no. 6, pp. 067009-1 to 067009-9, June 2014. DOI: 10.1117/1.JBO.19.6.067009

List of Publications

International Journal

- [1] **Md. Asadur Rahman**, Mohd Abdur Rashid, and Mohiuddin Ahmad, “Selecting the optimal conditions of Savitzky–Golay filter for fNIRS signal,” *Biocybernetics and Biomedical Engineering*, vol. 39, no. 3, pp. 624-637, 2019. DOI:10.1016/j.bbe.2019.06.004
- [2] **Md. Asadur Rahman**, Md. Shorif Uddin, and Mohiuddin Ahmad, “Modeling and Classification of Voluntary and Imagery Movement through fNIR & EEG Signals for Brain-Computer Interface,” *Health Information Science and Systems*, vol. 7, no. 22, December 2019. DOI: [10.1007/s13755-019-0081-5](https://doi.org/10.1007/s13755-019-0081-5)
- [3] **Md. Asadur Rahman**, Md. Kazem Hossain, Farzana Khanam, Mohammad Khurshed Alam, and Mohiuddin Ahmad, “Four-Class Motor Imagery EEG Signal Classification Using PCA, Wavelet, and Two-Stage Neural Network,” *International Journal of Advanced Computer Science and Applications*, vol. 10, no. 5, May 2019. DOI: 10.14569/IJACSA.2019.0100562
- [4] **Md. Asadur Rahman** and Mohiuddin Ahmad, “Modeling and Classification of Voluntary and Imagery Movements from the Prefrontal fNIRS Signals” (Under Review in *URASHIP Journal of Signal Processing*).

International Conferences

- [1] **Md. Asadur Rahman**, Mohiuddin Ahmad, and Farzana Khanam, “Detection of Effective Temporal Window for Classification of Motor Imagery Events from Prefrontal Hemodynamics,” *International Conference on Electrical, Computer and Communication Engineering (ECCE)*, Cox'sBazar, Bangladesh, 2019, pp. 1-6. DOI: 10.1109/ECACE.2019.8679317
- [2] **Md. Asadur Rahman**, Md. Mahmudul Haque Milu, Anika Anjum, Farzana Khanam, Md. Nurunnabi Mollah, and Mohiuddin Ahmad, “Classification of Motor Imagery Events from Prefrontal Hemodynamics for BCI Application,” *International Joint Conference on Computational Intelligence (IJCCI)*, 14-15

December, 2018, Daffodil International University, Dhaka, Bangladesh. pp. 1-06. DOI: 10.1007/978-981-13-7564-4_2

- [3] **Md. Asadur Rahman**, and Mohiuddin Ahmad, “Lie Detection from Single Feature of Functional Near Infrared Spectroscopic (fNIRS) Signals,” 2nd *International Conference on Electrical & Electronic Engineering (ICEEE 2017)*, 27-29 December, Rajshahi University of Engineering & Technology (RUET), Rajshahi, Bangladesh. DOI: 10.1109/CEEE.2017.8412900
- [4] **Md. Asadur Rahman** and Mohiuddin Ahmad, “Evaluating the Connectivity of Motor Area with Prefrontal Cortex by fNIR Spectroscopy,” *International Conference on Electrical, Computer, and Communication Engineering*, 2017, Cox’s Bazar, Bangladesh, February 16-18. DOI: 10.1109/ECACE.2017.7912921
- [5] **Md. Asadur Rahman** and Mohiuddin Ahmad, “Movement Related Events Classification from Functional Near Infrared Spectroscopic Signal,” *Int. Conf. on Computer and Information Technology (ICCIT)*, Dhaka, Bangladesh, 18-20 December, 2016, Dhaka, Bangladesh. DOI: 10.1109/ICCITECHN.2016.7860196
- [6] **Md. Asadur Rahman** and Mohiuddin Ahmad, “Lie Detection from fNIR Signal and NeuroImage,” *Int. Conf. on Medical Engineering, Health Informatics and Technology (MediTec)*, 17-18 December, 2016, Dhaka, Bangladesh. DOI: 10.1109/MEDITEC.2016.7835382
- [7] **Md. Asadur Rahman** and Mohiuddin Ahmad, “A Straight Forward Signal Processing Scheme to Improve Effect Size of fNIR Signals,” *5th International Conference on Informatics, Electronics & Vision (ICIEV 2016)*, Dhaka University, Dhaka, Bangladesh, May 2016. DOI: 10.1109/ICIEV.2016.7760042
- [8] **Md. Asadur Rahman** and Mohiuddin Ahmad, “Identifying Appropriate Feature to Distinguish between Resting and Active Condition from FNIRS,” *3rd International Conference on Signal Processing and Integrated Networks, (SPIN 2016)*, Amity University, Noida, New Delhi, India, February 2016. DOI: 10.1109/SPIN.2016.7566781

National Conferences

- [1] **Md. Asadur Rahman** and Mohiuddin Ahmad, “Hope and Hype of Functional Neuro Imaging by fNIR in Bangladesh,” *Annual Conf. of Bangladesh Society of Radiation Oncologist & Bangladesh Medical Physics Society*, September 2016, Dhaka, Bangladesh.
- [2] **Md. Asadur Rahman** and Mohiuddin Ahmad, “Towards a Portable Near-Infrared Spectroscopy System for Bedside Monitoring of a Patient Brain,” *4th Annual Conference of Bangladesh Medical Physics Society (ACBMPS)*, July 2015, Dhaka Medial College, Dhaka.

Appendix

A. SMAR Algorithm

Sometimes the acquired fNIR signals can be infected by head movement and some special noises are introduced in raw fNIR signals. Due to the motion of participant during optical brain imaging through fNIR causes coupling or the changes of pressure in the light sources and detectors. This reason and its corresponding effect can be captured within the raw fNIR signals as noise. This noise is found as spikes or burst noise with much higher or lower amplitudes than regular cortical activity. Additionally, the temporal sequences of these abrupt variations by reason of motion artifact in the raw fNIR signal are much faster than the typical raw signals. Sliding-window motion artifact rejection or SMAR algorithm can scan the fNIR signal to identify the segments with such characteristics. This algorithm measures light intensity at two different wavelengths (730nm and 850nm) and also a dark current condition to estimate the existence of any possible ambient light leakage.

Suppose that at the light intensity of wavelength, λ the raw fNIR signal is $x_\lambda(n)$ and the dark current has been measure $x_d(n)$ at that time. According to accomplish the SMAR algorithm following steps should be completed:

i) At first calculate a local coefficient of variation (*CV*) of the dark current for each n ,

$$CV_d(n) = \frac{\sqrt{\left(\frac{1}{N} \sum_{j=n-N/2}^{n+N/2} \left(x_d(j) - \left(\frac{1}{N+1} \sum_{i=n-N/2}^{n+N/2} x_d(i)\right) \right)^2\right)}{\left(\frac{1}{N+1} \sum_{i=n-N/2}^{n+N/2} x_d(i)\right)} \quad (\text{A.1})$$

where, $N+1$ indicates the sample size of the window.

ii) By the similar procedure, calculate $CV_{\lambda_1}(n)$ and $CV_{\lambda_2}(n)$ for the wavelength λ_1 and λ_2 , respectively.

iii) In this step, a threshold is needed to fix on the value of x_d and x_{λ_1} and x_{λ_2} after calculating CV_d , CV_{λ_1} and CV_{λ_2} , respectively. Therefore, to get the cleaned signals, \hat{x}_d , \hat{x}_{λ_1} and \hat{x}_{λ_2} following estimations are considered.

$$\hat{x}_d(n) = \begin{cases} x_d(n), & CV_d(n) < \tau_d^{upper} \\ NaN, & else \end{cases} \quad (\text{A.2})$$

where NaN indicates “Not a Number” that represents threshold or excluded value. Here, the upper threshold value for the concerned dark current is taken τ_d^{upper} . On the other hand, for the specific wavelength light intensity, window mean X_λ^n is calculated by (A.2) centering n ,

$$X_\lambda^n = \left(\frac{1}{N+1} \right) \sum_{i=n-N/2}^{n+N/2} x_\lambda(i) \quad (\text{A.3})$$

Therefore, the value of \hat{x}_{λ_1} and \hat{x}_{λ_2} can be calculated obeying the rule given in (A.4)

$$\hat{x}_\lambda(n) = \begin{cases} NaN, & X_\lambda^n > s \ \& \ \tau_\lambda^{lower} > CV_\lambda(n) \\ NaN, & CV_\lambda < \tau_\lambda^{upper} \\ x_\lambda(n), & else \end{cases} \quad (\text{A.4})$$

where, NaN is the excluded value and the upper and lower thresholds are τ_λ^{upper} and τ_λ^{lower} for the wavelength, λ_1 and λ_2 , respectively. In addition, s is the measure of saturation which is actually instrument depended. Since MBLL for concentration estimating equation requires the raw values of the both wavelengths, if one segment can be excluded for x_{λ_1} , x_{λ_2} or x_d it will eliminate the other wavelength raw values at the same time. The suggested threshold values and window size for the fNIR devices used in this research work are given in **Table A.1** those are considered to test the acquisition correctness of the fNIR signals.

Table A.1: The necessary parameters of SMAR algorithm and their recommended values

Parameters	N	s (mv)	τ_{λ}^{lower}	τ_{λ}^{upper}	τ_d^{upper}
Recommended Values	10	4000	0.003	0.025	0.015

B. Principal Component Analysis (PCA)

Suppose, a matrix A is consists of the n dimensional data. Now, a matrix U can be calculated which represents the eigenvectors sorted as the eigenvalues of the covariance matrix of A . In that case, we can get the PCA transformation of the data A in the form of Y as,

$$Y = U^T \Lambda \quad (\text{B.1})$$

The eigenvectors are also termed as the principal components. If only first r rows of Y are selected to project the data, the data becomes of r dimensional from d dimensions. This transformation is performed by singular value decomposition (SVD). The procedure to perform PCA by SVD can be described by matrix decomposition. Suppose, the matrix, Λ can be decomposed using SVD as,

$$\Lambda = \Omega \Gamma \Psi^T \quad (\text{B.2})$$

Here, Ω is $n \times m$ matrix with orthonormal columns ($\Omega^T \Omega = I$), Ψ is a $m \times m$ orthonormal matrix ($\Psi^T \Psi = I$), and Γ is a $m \times m$ diagonal matrix with positive or zero element which is also known as singular value. Besides, we can calculate the covariance matrix, C of Λ as,

$$C = \frac{1}{N} \Lambda \Lambda^T = \frac{1}{N} \Omega \Gamma^2 \Omega^T \quad (\text{B.3})$$

As the singular values are sorted in descending order and if $n < m$, the first n columns in Ω corresponds to the sorted eigenvalues of matrix C and if $m \geq n$, the first m corresponds to the sorted non-zero eigenvalues of C . Therefore, eventually the transformed data can be written as,

$$Y = U^T \Lambda = U^T U \Gamma \Psi^T \quad (\text{B.4})$$

C. Analysis of Variance (ANOVA)

Analysis of variance or ANOVA test is essential to testify the statistical strength of the hypothesis made on the data. When a number of subjects participated in a same working protocol, then the results from the all subjects are not same at all. From

multiple channels data, only the consistent results are taken into account to take decision. This consistency measurement is done statistically. One of the major and well established procedures is ANOVA. A two way ANOVA of samples with 0 mean and standard deviation σ , is described by the following equation:

$$\pi_{jk} = \mu + \alpha_j + \beta_k + \zeta_{jk} \quad (C.1)$$

Here, μ is grand mean of population, α_j is sample effect, β_k is column effect, and ζ_{jk} is the chance of error. Suppose, the number of samples per row is b and number of samples per column is a then on the basis of samples of two way ANOVA test, the expectation of variations are,

$$\text{Error variation, } E(V_E) = (a - 1)(b - 1)\sigma^2 \quad (C.2)$$

$$\text{Variation between rows, } E(V_R) = (a - 1)\sigma^2 + b\sum_j \alpha_j^2 \quad (C.3)$$

$$\text{Variation between columns, } E(V_C) = (b - 1)\sigma^2 + a\sum_k \beta_k^2 \quad (C.4)$$

$$\text{Total variation, } E(V) = (ab - 1)\sigma^2 + a\sum_k \beta_k^2 + b\sum_j \alpha_j^2 \quad (C.5)$$

Regardless of hypothesis, a best unbiased estimation of variance σ^2 is provided by,

$$S_E^2 = \frac{V_E}{(a - 1)(a - b)} \text{ which is actually } E(S_E^2) = \sigma^2. \text{ In case of hypothesis, } H_0^{(1)} \text{ or } H_0^{(2)}$$

are true, then (C.6) - (C.8) will be unbiased estimates of σ^2 .

$$S_R^2 = \frac{V_R}{(a - 1)} \quad (C.6)$$

$$S_C^2 = \frac{V_C}{(b - 1)} \quad (C.7)$$

$$S^2 = \frac{V_C}{(ab - 1)} \quad (C.8)$$

However the two hypotheses are not true, we get from (C.6) and (C.7),

$$E(S_R^2) = \sigma^2 + \frac{b}{a - 1} \sum_j \alpha_j^2 \quad (C.9)$$

$$E(S_C^2) = \sigma^2 + \frac{a}{b - 1} \sum_k \alpha_k^2 \quad (C.10)$$

According to the results of ANOVA are tested by the fisher values to testify the hypothetical strength of the data. This result will help us to find the most effective channel to classify the activities and model the BCI.

D. Code of Graphical Protocol Aiding Application Software

```

%%%%%%%%%%%%%%%%%%%%%%%%%%%%%%%%%%%%%%%%%%%%%%%%%%%%%%%%%%%%
% This is a MATLAB based graphical protocol of four different
% event-oriented data acquisition aiding software
% This is coded by Md. Asadur Rahman, PhD Candidate,
% Dept. of BME, Khulna University of Engineering & Technology
% and a property of ABC_KUET
% (Advanced Bio-Engineering Club of KUET)
%%%%%%%%%%%%%%%%%%%%%%%%%%%%%%%%%%%%%%%%%%%%%%%%%%%%%%%%%%%%

```

```

clc
clear all
close all

```

```

for j=1:1:5 %% Please put the number how many trials you want to take in a session

```

```

%%%%%%%%%%%%%%%%%%%%%%%%%%%%%%%%%%%%%%%%%%%%%%%%%%%%%%%%%%%%
% Rest
%%%%%%%%%%%%%%%%%%%%%%%%%%%%%%%%%%%%%%%%%%%%%%%%%%%%%%%%%%%%

```

```

subplot 335
title('Rest')
% the flashing block on frequency
t = timer;
set(t, 'executionMode', 'fixedRate');
freq = 1;
period = 1/freq;
set(t, 'Period', 1/freq);
set(t, 'TimerFcn', 'show');
flash = true;

```

```

RectPos = [0,0,1,1];

```

```

%% Set the visible property to off.
show = rectangle('Position',RectPos,'FaceColor','r','Visible','off');
hide = rectangle('Position',RectPos,'FaceColor','r','Visible','off');

```

```

% set the background to green
set(gcf, 'Color', [0 1 1]);

```

```

for i=0:1:20;

```

```

%% Play with the "Visible" property to show/hide the rectangles.
set(show,'Visible','on')

```

```

pause(0.1)

```

```

set(show,'Visible','off')
set(hide,'Visible','on');
drawnow

```

```

pause(0.1)
set(hide,'Visible','off');

```

```

set(gca,'xcolor',get(gcf,'color'));
set(gca,'ycolor',get(gcf,'color'));
%set(gca,'ytick',[]);
%set(gca,'xtick',[]);
i=i+1;

```

```

end

```

```

%%%%%%%%%%%%%%%%%%%%%%%%%%%%%%%%%%%%%%%%%%%%%%%%%%%%%%%%%%%%
% Left Hand Movement
%%%%%%%%%%%%%%%%%%%%%%%%%%%%%%%%%%%%%%%%%%%%%%%%%%%%%%%%%%%%

```

```

subplot 331
title('Left Hand')
% the flashing block on frequency
t = timer;
set(t, 'executionMode', 'fixedRate');
freq = 5;

```

```

period = 1/freq;
set(t, 'Period', 1/freq);
set(t, 'TimerFcn', 'show');
flash = true;

RectPos = [0,0,1,1];

%// Set the visible property to off.
show = rectangle('Position',RectPos,'FaceColor','g','Visible','off');
hide = rectangle('Position',RectPos,'FaceColor','r','Visible','off');

% set the background to black
set(gcf, 'Color', [0 1 1] );

for i=1:1:20;

%// Play with the "Visible" property to show/hide the rectangles.
set(show,'Visible','on')

pause(0.1)

set(show,'Visible','off')
set(hide,'Visible','on');
drawnow

F(i)=getframe(gcf);
pause(0.1)
set(hide,'Visible','off');

set(gca,'xcolor',get(gcf,'color'));
set(gca,'ycolor',get(gcf,'color'));
set(gca,'ytick',[]);
set(gca,'xtick',[]);
i=i+1;
end

%%%%%%%%%%%%%%%%%%%%%%%%%%%%%%%%%%%%%%%%%%%%%%%%%%%%%%%%%%%%%%%%%%%%%%%%%%%%%%
%%%%%%%%%%%%%%%%%%%%%%%%%%%%%%%%%%%%%%%%%%%%%%%%%%%%%%%%%%%%%%%%%%%%%%%%%%%%%% Rest %%%%%%%%%%%%%%%%%%%%%%%%%%%%%%%%%%%%%%%%%%%%%%%%%%%%%%%%%%%%%%%%%%%%%%%%%%%%%%%
%%%%%%%%%%%%%%%%%%%%%%%%%%%%%%%%%%%%%%%%%%%%%%%%%%%%%%%%%%%%%%%%%%%%%%%%%%%%%%

subplot 335
title('Rest')
% the flashing block on frequency
t = timer;
set(t, 'executionMode', 'fixedRate');
freq = 1;
period = 1/freq;
set(t, 'Period', 1/freq);
set(t, 'TimerFcn', 'show');
flash = true;

RectPos = [0,0,1,1];

%// Set the visible property to off.
show = rectangle('Position',RectPos,'FaceColor','r','Visible','off');
hide = rectangle('Position',RectPos,'FaceColor','r','Visible','off');

% set the background to black
set(gcf, 'Color', [0 1 1] );

for i=0:1:20;

%// Play with the "Visible" property to show/hide the rectangles.
set(show,'Visible','on')

pause(0.1)

set(show,'Visible','off')
set(hide,'Visible','on');
drawnow

pause(0.1)
set(hide,'Visible','off');

```

```

set(gca,'xcolor',get(gcf,'color'));
set(gca,'ycolor',get(gcf,'color'));
set(gca,'ytick',[]);
set(gca,'xtick',[]);
i=i+1;
end

```

%%
%% Right Hand %%%
%%

```

subplot 333
title('Right Hand')
% the flashing block on frequency
t = timer;
set(t, 'executionMode', 'fixedRate');
freq = 5;
period = 1/freq;
set(t, 'Period', 1/freq);
set(t, 'TimerFcn', 'show');
flash = true;

```

```
RectPos = [0,0,1,1];
```

```

%// Set the visible property to off.
show = rectangle('Position',RectPos,'FaceColor','g','Visible','off');
hide = rectangle('Position',RectPos,'FaceColor','r','Visible','off');

```

```

% set the background to black
set (gcf, 'Color', [0 1 1] );

```

```
for i=0:1:20;
```

```

%// Play with the "Visible" property to show/hide the rectangles.
set(show,'Visible','on')

```

```
pause(0.1)
```

```

set(show,'Visible','off')
set(hide,'Visible','on');
drawnow

```

```

pause(0.1)
set(hide,'Visible','off');

```

```

set(gca,'xcolor',get(gcf,'color'));
set(gca,'ycolor',get(gcf,'color'));
set(gca,'ytick',[]);
set(gca,'xtick',[]);
i=i+1;
end

```

```
end
```

%%
%% Rest %%%
%%

```

subplot 335
title('Rest')
% the flashing block on frequency
t = timer;
set(t, 'executionMode', 'fixedRate');
freq = 1;
period = 1/freq;
set(t, 'Period', 1/freq);
set(t, 'TimerFcn', 'show');
flash = true;

```

```
RectPos = [0,0,1,1];
```

```

%// Set the visible property to off.
show = rectangle('Position',RectPos,'FaceColor','r','Visible','off');
hide = rectangle('Position',RectPos,'FaceColor','r','Visible','off');

```



```

% set the background to black
set (gcf, 'Color', [0 1 1] );

for i=0:1:20;

%// Play with the "Visible" property to show/hide the rectangles.
    set(show,'Visible','on')

    pause(0.1)

    set(show,'Visible','off')
    set(hide,'Visible','on');
    drawnow

    pause(0.1)
    set(hide,'Visible','off');

    set(gca,'xcolor',get(gcf,'color'));
    set(gca,'ycolor',get(gcf,'color'));
    set(gca,'ytick',[]);
    set(gca,'xtick',[]);
    i=i+1;
end

%%%%%%%%%%%%%%%%%%%%%%%%%%%%%%%%%%%%%%%%%%%%%%%%%%%%%%%%%%%%%%%%%%%%%%%%%%%%%%
%%%%%%%%%%%%%%%%%%%%%%%%%%%%%%%%%%%%%%%%%%%%%%%%%%%%%%%%%%%%%%%%%%%%%%%%%%%%%% Left Foot Movement %%%%%%%%%%%%%%%%%%%%%%%%%%%%%%%%%%%%%%%%%%%%%%%%%%%%%%%%%%%%%%%%%%%%%%%%%%%%%%%
%%%%%%%%%%%%%%%%%%%%%%%%%%%%%%%%%%%%%%%%%%%%%%%%%%%%%%%%%%%%%%%%%%%%%%%%%%%%%%

subplot 337
title('Left Foot')
% the flashing block on frequency
t = timer;
set(t, 'executionMode', 'fixedRate');
freq = 5;
period = 1/freq;
set(t, 'Period', 1/freq);
set(t, 'TimerFcn', 'show');
flash = true;

RectPos = [0,0,1,1];

%// Set the visible property to off.
show = rectangle('Position',RectPos,'FaceColor','g','Visible','off');
hide = rectangle('Position',RectPos,'FaceColor','r','Visible','off');

% set the background to black
set (gcf, 'Color', [0 1 1] );

for i=0:1:20;

%// Play with the "Visible" property to show/hide the rectangles.
    set(show,'Visible','on')

    pause(0.1)

    set(show,'Visible','off')
    set(hide,'Visible','on');
    drawnow

    pause(0.1)
    set(hide,'Visible','off');

    set(gca,'xcolor',get(gcf,'color'));
    set(gca,'ycolor',get(gcf,'color'));
    set(gca,'ytick',[]);
    set(gca,'xtick',[]);
    i=i+1;
end

%%%%%%%%%%%%%%%%%%%%%%%%%%%%%%%%%%%%%%%%%%%%%%%%%%%%%%%%%%%%%%%%%%%%%%%%%%%%%%
%%%%%%%%%%%%%%%%%%%%%%%%%%%%%%%%%%%%%%%%%%%%%%%%%%%%%%%%%%%%%%%%%%%%%%%%%%%%%% Rest %%%%%%%%%%%%%%%%%%%%%%%%%%%%%%%%%%%%%%%%%%%%%%%%%%%%%%%%%%%%%%%%%%%%%%%%%%%%%%%
%%%%%%%%%%%%%%%%%%%%%%%%%%%%%%%%%%%%%%%%%%%%%%%%%%%%%%%%%%%%%%%%%%%%%%%%%%%%%%

```



```
set(show,'Visible','off')
set(hide,'Visible','on');
drawnow

pause(0.1)
set(hide,'Visible','off');

set(gca,'xcolor',get(gcf,'color'));
set(gca,'ycolor',get(gcf,'color'));
set(gca,'ytick',[]);
set(gca,'xtick',[]);
i=i+1;
end

j=j+1;
end
```